D I P L O M A R B E I T

First-Principles Screening of Fluoride-Based Compounds for Gate Dielectric Applications

ausgeführt zum Zwecke der Erlangung des akademischen Grades
eines Diplom-Ingenieurs (Dipl.-Ing.)

unter der Betreuung von

Univ.Prof. Dipl.-Ing. Dr.techn. Tibor Grasser

unter der Assistenz von

Univ.Ass. Dipl.-Ing. Dr.techn. Dominic Waldhör
Dipl.-Ing. Dr.techn. Christoph Wilhelmer

eingereicht an der Technischen Universität Wien
Fakultät für Elektrotechnik und Informationstechnik
von

Jonas Bodingbauer, BSc BSc
Matrikelnummer: 11802486

Wien, im Juni 2025 _____

ABSTRACT

Modern metal-oxide-semiconductor (MOS) device technologies are aiming for insulating layers with an equivalent oxide thickness (EOT) of less than 1 nm. Up to now, these small EOTs are achieved by using high-k materials like HfO_2 as gate dielectrics. However, finding alternative insulators with a high dielectric constant, a large band gap, and a good interface quality with potential channel materials remains a challenge. Exploring new material systems experimentally is time-consuming and costly. Theoretical methods, on the other hand, enable fast screening of several materials, predicting their properties while also improving the understanding of microscopic processes.

Recent studies suggest that fluorides are a promising material class for electronic applications due to their inherently high band gaps and relatively high dielectric constants. In this work, density functional theory (DFT) calculations using a hybrid functional were employed to predict and compare the band gaps and dielectric constants of various fluorides. After this initial screening step, the most promising candidates lanthanum trifluoride (LaF_3) and bismuth trifluoride (BiF_3) were analyzed, as well as two reference materials, zirconium tetrafluoride (ZrF_4) and the already well-studied calcium difluoride (CaF_2), for benchmarking purposes.

In particular, the fluorine vacancy defect was examined in these materials, as this defect is suspected to negatively impact the reliability of electronic devices by charge trapping or diffusion through the gate dielectric. The formation energies of the possible charge states of these defects were calculated, and their stability was analyzed within the formation energy formalism. Additionally, their vacancy diffusion mechanism was analyzed by calculating the migration barriers with the nudged elastic band method and compared to experimental data.

The calculations reveal that LaF_3 is the most promising material, considering its high theoretical band gap of 9.9 eV and relative permittivity of 14.2. BiF_3, on the other hand, has a band gap of 6.61 eV and a high relative total permittivity of 46.6. Both materials have small F vacancy diffusion barriers (0.20 eV for LaF_3 and 100 meV for BiF_3) according to the calculations, which might lead to reliability issues when used in ultra-scaled devices. Additionally, for BiF_3, these defects are stable in various charge states depending on the Fermi level, which might cause further reliability issues. ZrF_4, with a large band gap of 7.6 eV and $\varepsilon_r = 10.8$, presumably has a comparatively high diffusion activation energy over 1 eV due to a metastable configuration with high energy along the diffusion path.

KURZFASSUNG

Moderne Metall-Oxid-Halbleiter (MOS)-Bauelementtechnologien streben Isolationsschichten mit einer effektiven Oxiddicke (EOT) von weniger als 1 nm an. Bislang werden diese kleinen EOTs durch den Einsatz von high-k-Materialien wie HfO_2 als Gate-Dielektrikum erreicht. Die Suche nach alternativen Isolatoren mit hoher Dielektrizitätskonstante, großer Bandlücke und guter Grenzflächenqualität zu potenziellen Kanalmaterialien bleibt jedoch eine Herausforderung. Die experimentelle Erkundung neuer Materialsysteme ist zeitaufwendig und kostspielig. Theoretische Methoden hingegen ermöglichen ein schnelles *Screening* mehrerer Materialien, indem sie deren Eigenschaften vorhersagen und gleichzeitig das Verständnis mikroskopischer Prozesse verbessern.

Aktuelle Studien deuten darauf hin, dass Fluoride aufgrund ihrer von Natur aus hohen Bandlücken und vergleichsweise hohen Dielektrizitätskonstanten eine vielversprechende Materialklasse für elektronische Anwendungen darstellen. In dieser Arbeit wurden Dichtefunktionaltheorie (DFT)-Berechnungen mit einem hybriden Funktional durchgeführt, um die Bandlücken und Dielektrizitätskonstanten verschiedener Fluoride vorherzusagen und zu vergleichen. Nach diesem initialen *Screening* wurden die vielversprechendsten Kandidaten Lanthantrifluorid (LaF_3) und Bismuttrifluorid (BiF_3) sowie zwei Referenzmaterialien Zirconiumtetrafluorid (ZrF_4) und das bereits gut untersuchte Calciumdifluorid (CaF_2) zu Vergleichszwecken genauer analysiert.

Insbesondere wurde die Fluorvakanz in diesen Materialien untersucht, da dieser Defekt vermutlich die Zuverlässigkeit elektronischer Bauelemente durch *Charge Trapping* oder Diffusion durch das Gatedielektrikum negativ beeinflusst. Die Bildungsenergien der möglichen Ladungszustände dieser Defekte wurden berechnet und ihre Stabilität mit dem Formationsenergie-Formalismus analysiert. Zusätzlich wurden verschiedene Diffusionsmechanismen der Vakanzen durch Berechnung der Migrationsbarrieren mit der *Nudged Elastic Band* Methode untersucht und mit experimentellen Daten verglichen.

Die Berechnungen zeigen, dass LaF_3 das vielversprechendste Material ist, basierend auf seiner hohen theoretischen Bandlücke von 9.9 eV und einer relativen Permittivität von 14.2. BiF_3 hingegen besitzt eine Bandlücke von 6.61 eV und eine hohe relative Gesamtpermittivität von 46.6. Beide Materialien haben laut den Berechnungen kleine Fluorvakanzdiffusionsbarrieren (0.20 eV für LaF_3 und 100 meV für BiF_3), was möglicherweise zu Zuverlässigkeitsproblemen bei der Verwendung in ultraskaligen Bauelementen führt. Zusätzlich sind diese Defekte in BiF_3 je nach Ferminiveau in verschiedenen Ladungszuständen stabil, was zu weit-

eren Zuverlässigkeitsproblemen führen könnte. ZrF_4, mit einer großen Bandlücke von 7.6 eV und $\varepsilon_r = 10.8$, weist vermutlich aufgrund einer metastabilen Konfiguration mit hoher Energie entlang des Diffusionspfades eine vergleichsweise hohe Aktivierungsenergie von über 1 eV auf.

ACKNOWLEDGEMENTS

First, I would like to thank my supervisor, Tibor Grasser, who encouraged me to take on this project and made it possible for me to explore this fascinating topic. His teaching during my studies greatly deepened my interest in understanding the underlying physics of semiconductor devices and laid the foundation for this work.

I want to thank Dominic Waldhör and Christoph Wilhelmer for their great guidance and advice. They supported me along the way and helped me to understand new concepts quickly. Without their help, I would probably still be tuning parameters of the many employed methods. I am also grateful for their insightful comments on this manuscript, which significantly contributed to its clarity and cohesion.

Zoltán Hajnal took the time to explain many basic concepts and helped me with my first steps conducting DFT simulations. His welcoming attitude during many fruitful discussions was essential for my entry into this, at first, overwhelming field.

I also want to thank my colleagues - Angus, Anna, Gerald, Martin, Robert *et al.* - in the office, who always had an open ear when I needed to vent some frustration when computations did not converge, and who also helped me with some problems I encountered.

Calculations were performed using supercomputer resources provided by the Vienna Scientific Cluster (VSC). I want to thank the VSC support team for the resources provided. Without them, this work would not have been possible.

A big thank you is also due to my family, who supported me through all my studies, even though I took on two degrees at once. Without them, this would not have been possible at all, and I am extremely grateful for everything they have done, and are doing for me.

Furthermore, I want to thank my friends who went on many coffee breaks with me and helped me take my mind off work when I needed it.

Last but not least, thank you, Lena, for all your support and understanding during all of my studies. Time and time again, you helped keep me sane and highlighted the important things in life.

Hiermit erkläre ich, dass die vorliegende Arbeit gemäß den Code of Conduct - Regeln zur Sicherung guter wissenschaftlicher Praxis (in der aktuellen Fassung des jeweiligen Mitteilungsblattes der TU Wien), insbesondere ohne unzulässige Hilfe Dritter und ohne Benutzung anderer als der angegebenen Hilfsmittel, angefertigt wurde. Die aus anderen Quellen direkt oder indirekt übernommenen Daten und Konzepte sind unter Angabe der Quelle gekennzeichnet. Die Arbeit wurde bisher weder im In- noch im Ausland in gleicher oder in ähnlicher Form in anderen Prüfungsverfahren vorgelegt.

Wien, am 21. Mai 2025

Jonas Bodingbauer

CONTENTS

LIST OF FIGURES

LIST OF TABLES

LIST OF ABBREVIATIONS

ADMM	Auxiliary density matrix method
API	Application programming interface
BEC	Born effective charge
BFGS	Broyden-Fletcher-Goldfarb-Shanno
BTI	Bias temperature instability
CI-NEB	Climbing image nudged elastic band
DFT	Density functional theory
DOS	Density of states
EOT	Equivalent oxide thickness
FET	Field effect transistor
GAA	Gate-all-around
GAPW	Gaussian augmented plane waves
GGA	Generalized gradient approximation
GPW	Gaussian plane waves
HFX	Hartree-Fock exchange
HOMO	Highest occupied molecular orbital
LBFGS	Limited-memory Broyden-Fletcher-Goldfarb-Shanno
LDA	Local density approximation
LO	Longitudinal optical
LUMO	Lowest unoccupied molecular orbital
MOS	Metal-oxide-semiconductor
NEB	Nudged elastic band
OT	Orbital transform
PBE	Perdew-Burke-Ernzerhof
PDOS	Projected density of states
PES	Potential energy surface
PP	Pseudopotential
PW91	Perdew-Wang 1991
RTN	Random telegraph noise
TCAD	Technology computer aided design
TO	Transversal optical

CHAPTER 1
INTRODUCTION

Today's nanoelectronics technologies are largely based on metal-oxide-semiconductor (MOS) devices, which have been scaled to the low nanometer regime. Such devices require a stack of compatible materials, all of which are crucial for its performance. In this chapter, the principles of MOS devices are introduced, along with the most relevant properties of the insulating layer - the focus of this thesis.

1.1 Metal-Oxide-Semiconductor Devices

Silicon remains the primary semiconductor material in device fabrication. A key reason for silicon's continued dominance as the channel material is its ability to thermally grow high-quality interfaces with its native insulating silicon dioxide (SiO_2) layer [1].

The continued miniaturization of devices has introduced several challenges, including short channel effects [2] and increased leakage currents due to thinning of the insulating layer. Thinner layers allow more current to tunnel through. To mitigate this, nitrogen was initially added to the oxide, forming SiO_xN_y layers, which helped reduce leakage [3]. As scaling progressed, the industry adopted high-k dielectrics such as HfO_2 and ZrO_2 [4]. These materials enable thicker insulating layers while preserving gate control over the channel due to their higher dielectric constants.

Geometric innovations beyond planar devices have also been introduced. FinFETs use a 3D structure to increase the controlled channel area. Figure 1.1 schematically compares planar and FinFET geometries. The latest advancements in surface-area-enhancing structures are gate-all-around (GAA) and nanosheet transistors [5], in which the gate surrounds the channel entirely. This provides better control, though it increases manufacturing complexity.

Although modern devices are still primarily silicon-based, materials like SiGe, SiC, and GaN are also used commercially for high-speed and power electronics [5]. For photonic and optoelectronic applications, III-V materials such as GaAs and GaP are preferred due to their direct bandgaps [5]. For continued scaling, two-dimensional materials like MoS_2 are being actively researched as promising candidates, though they currently face integration and reliability challenges [6].

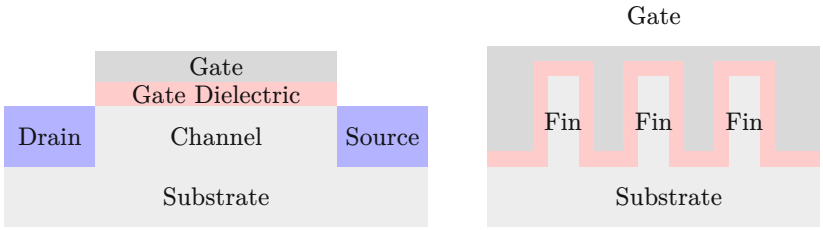

(a) Planar FET (b) FinFET

Figure 1.1: Schematic representation of a cross-section through a planar (left) and FinFET (right) device. The current flows in the axis perpendicular to the page for the FinFET.

1.2 Insulators

All the presented transistor devices rely on high-quality insulating layers, whose properties must be examined in detail to support the development of future technologies. The insulator's purpose in a device is to electrically separate the gate from the channel, preventing current flow through it. The electric field from the gate must still control the channel, which is aided by a high permittivity of the insulator. The properties of insulators are discussed in the following sections.

The electronic band structure of a material determines its electrical properties. Particularly the electronic band gap, which corresponds to the energy required to excite an electron from the valence band to the conduction band. This band gap can be used to distinguish between insulators, semiconductors, and metals. A material with a band gap larger than 4 eV is typically considered an insulator [7], while those with smaller band gaps are called semiconductors, and materials without a band gap are classified as metals. Based on their bonding mechanisms, insulators can be categorized into three types [8]:

- **Covalent insulators** share electrons between the valence orbitals of nuclei, typically forming localized bond states. The formation of these bonds depends primarily on the valence shell structure of the involved nuclei - especially on the number of valence electrons. A well-known example is SiO_2.
- **Ionic insulators** consist of metallic and nonmetallic elements, where electrons are transferred from the metallic to the nonmetallic atom. These crystals have highly localized electronic states, similar to molecular crystals, but their nuclei are charged ions. These ions dominate many material

properties, setting ionic crystals apart from molecular ones despite their shared localization characteristics.

- **Molecular insulators** are formed by molecules held together through weaker interactions such as van der Waals forces, dipole-dipole interactions, or hydrogen bonds. The strong bonds exist within the molecules, while the weaker forces bind the molecules together. Such materials are for example used in flexible optoelectronic devices [9].

However, this classification is not clear-cut, and crystals may exhibit characteristics of multiple types. For example, Si is a purely covalent crystal, while the polar semiconductor GaAs is primarily covalent with some ionic character, and CaSe is ionic with slight covalent character [8].

All the materials studied in this thesis are ionic crystals, meaning their properties are largely governed by charged ions. Fluorine, being the most electronegative element in the periodic table, forms ionic bonds with other elements, resulting in crystals with an almost purely ionic character.

1.3 Permittivity

For building electronic devices such as MOS field effect transistors (FETs), the permittivity of the insulator is one of the most important properties. In a simple, isotropic, linear material, it is the proportionality constant between the electric field $\mathbf{E}$ and the electric displacement field $\mathbf{D}$:

$$\mathbf{D} = \varepsilon \mathbf{E} = \varepsilon_0 \varepsilon_r \mathbf{E} \tag{1.1}$$

The permittivity ε is expressed as the product of the vacuum permittivity ε_0 and the relative permittivity ε_r. In more complex anisotropic materials, it becomes a second-rank tensor.

The saturation region of the IV characteristic of a MOS device can be modeled by [8]

$$I_{\mathrm{DSsat}} \approx \frac{W}{2LM} \mu_e C_{\mathrm{ox}} (V_{\mathrm{GS}} - V_{\mathrm{th}})^2 \tag{1.2}$$

where M is an ideality factor close to 1, W is the channel width, L is the channel length, μ_e is the electron mobility, C_{ox} is the capacitance of the MOS capacitor, V_{GS} is the gate-source voltage, and V_{th} is the threshold voltage. The capacitance depends on both the thickness and permittivity of the insulator, and can be compared across materials using the equivalent oxide thickness (EOT). The EOT is the “electrostatically corrected” thickness of the material - defined as

the thickness that a SiO_2 layer would need to have to yield the same capacitance.

$$\mathrm{EOT} = t_{\mathrm{mat}} \frac{\varepsilon_{\mathrm{SiO_2}}}{\varepsilon_{\mathrm{mat}}} \tag{1.3}$$

A high-permittivity material lowers this value when the physical thickness is kept constant [4]. For this reason, high-k materials are used in modern devices to reduce the effective oxide thickness while keeping the physical layer thicker, thereby limiting leakage currents.

1.4 Gate Leakage Currents

Leakage currents are undesired currents in a MOS device that flow through the insulating layer. These are typically caused by tunneling and can arise from various tunneling mechanisms. Additional currents may result from defects in the insulator, which not only affect tunneling behavior but can also lead to ionic conduction by enabling the diffusion of charged species through the material. In general, leakage currents increase as insulator thickness decreases, posing a major challenge for continued device scaling [10].

1.4.1 Tunneling Processes

Several tunneling mechanisms can occur in insulating layers, as schematically shown in Fig. 1.2. In a defect-free insulator, the barrier height is determined by the band gap and the relative alignment of the band edges with those of the semiconductor. An external electric field modifies this barrier, creating a trapezoidal potential.

Tunneling in a Defect-Free Insulator

In a (near) defect-free insulator, direct tunneling and Fowler-Nordheim tunneling are dominant mechanisms [11]. Direct tunneling involves a carrier tunneling through a trapezoidal barrier, whereas Fowler-Nordheim tunneling involves tunneling through a triangular barrier. These processes are illustrated in Fig. 1.3. In direct tunneling, the carrier moves directly between the channel and the gate. In contrast, Fowler-Nordheim tunneling involves the carrier tunneling to the conduction band of the insulator, after which it is transported by the electric field to the semiconductor.

Both tunneling processes can be modeled using the Tsu-Esaki model, which is based on the WKB approximation of the Schrödinger equation [11]. The WKB approximation is a semi-classical method in quantum mechanics that enables

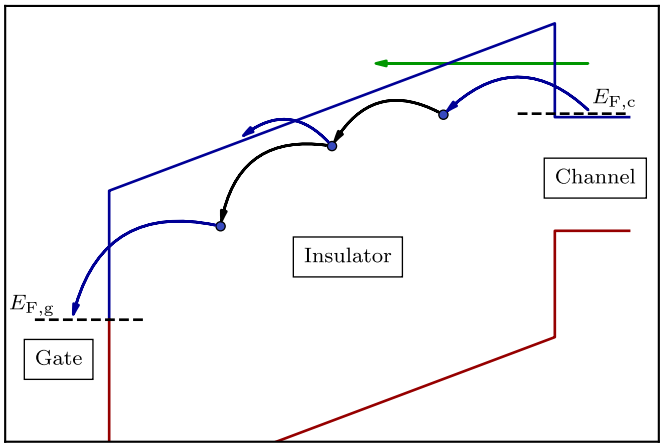

Figure 1.2: Schematic representation of tunneling leakage currents in a MOS device. The green arrow depicts Fowler-Nordheim tunneling, the black arrows show trap-to-trap tunneling, and the blue arrows indicate tunneling from a trap to the conduction band. (Adapted from [11])

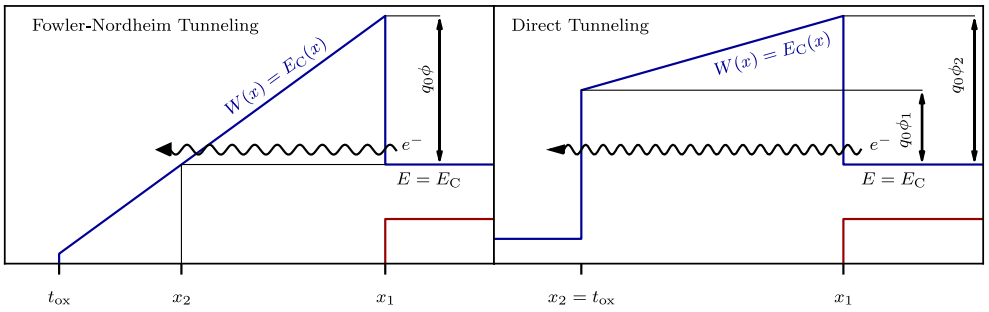

Figure 1.3: Fowler-Nordheim and direct tunneling processes over a barrier [11].

calculation of the wavefunction decay within a potential barrier. In both cases, the charge carrier travels directly through or over the barrier. Unlike in trap-assisted tunneling, discussed in the next section.

Trap-Assisted Tunneling

Defects in an insulator can enable trap-assisted tunneling. Traps correspond to electronic states within the band gap of an insulator that can capture and release electrons. These are typically caused by impurities and structural imperfections [12].

The efficiency of trap-assisted tunneling depends on the energy level of the trap relative to the insulators band edges and the trap's spatial position within the insulator. Higher defect concentrations and lower relaxation energies of the

defects enhance the hopping mechanism, allowing for significant gate-leakage currents. This process is strongly temperature dependent due to the need for electron-phonon coupling to facilitate charge trapping at defects [11].

Trap-assisted tunneling includes both single-step and multistep tunneling processes, as schematically shown in Fig. 1.2. Charge trapping at these states also contributes to other detrimental effects in MOS devices, such as random telegraph noise (RTN) [13] and bias temperature instability [14].

The characteristics of trap-assisted tunneling, in particular its temperature and bias dependence, can be used to experimentally determine defect parameters, such as trap energy levels and relaxation energies. These measurements can then be compared with theoretical predictions from DFT calculations to identify specific defect types relevant to tunneling. For example, such analyses have shown that polaronic defect states are likely responsible for trap-assisted tunneling in amorphous oxides [15].

In summary, both the barrier height, determined by the band gap, and the defect properties and their distribution within the insulator are critical factors influencing leakage currents in MOS devices.

1.4.2 Diffusion of Defects

Defects can not only conduct current via charge trapping and emission, as discussed previously, but may also diffuse through the material. If these defects are charged, they can cause ionic conduction within the insulator. This can be beneficial, as it may enhance the low-frequency permittivity of the material, as shown in [16]. For high-frequency applications, however, the defects do not have sufficient time to move and therefore do not contribute to the permittivity.

On the downside, the diffusion of charged defects alters the electronic properties of the insulator, which can negatively impact device performance and reliability, leading to significant instabilities. In early silicon devices, for instance, sodium ions diffusing through the SiO_2 layer were found to cause major issues [17].

To investigate this phenomenon and the properties of the diffusing defects, density functional theory (DFT) can be used to calculate the diffusion barriers of defects within the insulator.

1.5 Fluorides

Fluorides, the salts of hydrofluoric acid, have recently gained attention as insulators for next-generation devices using 2D materials, due to their high band gaps and permittivity [16, 18–22]. They are ionic crystals, with fluorine as the anion

and a metal as the cation. The high band gap is beneficial for implementing thin insulating layers, as the tunneling barrier height is increased, which suppresses the (direct) tunneling rate. Additionally, a high permittivity allows for thicker layers while maintaining the same EOT, further reducing leakage currents.

The first investigations of MOS devices with fluoride layers were conducted in 1984, where a thin film of calcium fluoride was grown on a (111) silicon substrate. The films, with thicknesses of several hundred nanometers, showed no strain, indicating that epitaxial growth of this material system is possible [23, 24]. This was enabled by the small lattice mismatch between the Si (111) surface and CaF_2, which is only 0.6 % [25].

More recently, CaF_2 has been successfully demonstrated in a MOS device with a 2D material, specifically MoS_2, as the semiconductor. Working devices with an epitaxially grown 2 nm thick CaF_2 layer have been shown. In this application, the material exhibits a band gap of 12.1 eV and a permittivity of 8.4, resulting in an EOT of approximately 0.9 nm, achieving sub-nm EOT [19].

However, not only CaF_2 is of interest for future applications. Other fluorides, mainly based on lanthanides and group II and III elements, such as LaF_3 and CeF_3, have also been studied experimentally by Meng *et al.* [16]. These materials were deposited as thin films by thermal evaporation, and their surface quality, capacitance as a function of frequency, and leakage currents were subsequently characterized. Some examined fluorides exhibited superionic conductivity, resulting in much higher static capacitance values at low frequencies compared to high frequencies [16]. The successful thin-film deposition of these materials is a key prerequisite for their use in devices.

Dielectrics compatible with 2D materials are of particular interest for potential future ultra-scaled devices. To identify suitable candidates, computer-based material simulations are valuable tools to reduce experimental effort. High-throughput *ab initio* calculations by Lee *et al.* [18] compared different material classes, including carbides, nitrides, phosphides, sulfides, chlorides, and fluorides. Using a generalized gradient approximation (GGA)+U functional, they found that fluorides tend to have the highest band gaps while maintaining decent permittivity [18], making them promising materials for next-generation electronics.

The distribution of studied fluorides from the high-throughput study is shown in Fig. 1.4. Fluorides have the highest band gaps compared to other material classes. Outliers with relatively high permittivity and band gap, such as LaF_3 and BiF_3, were identified in the data for fluorides.

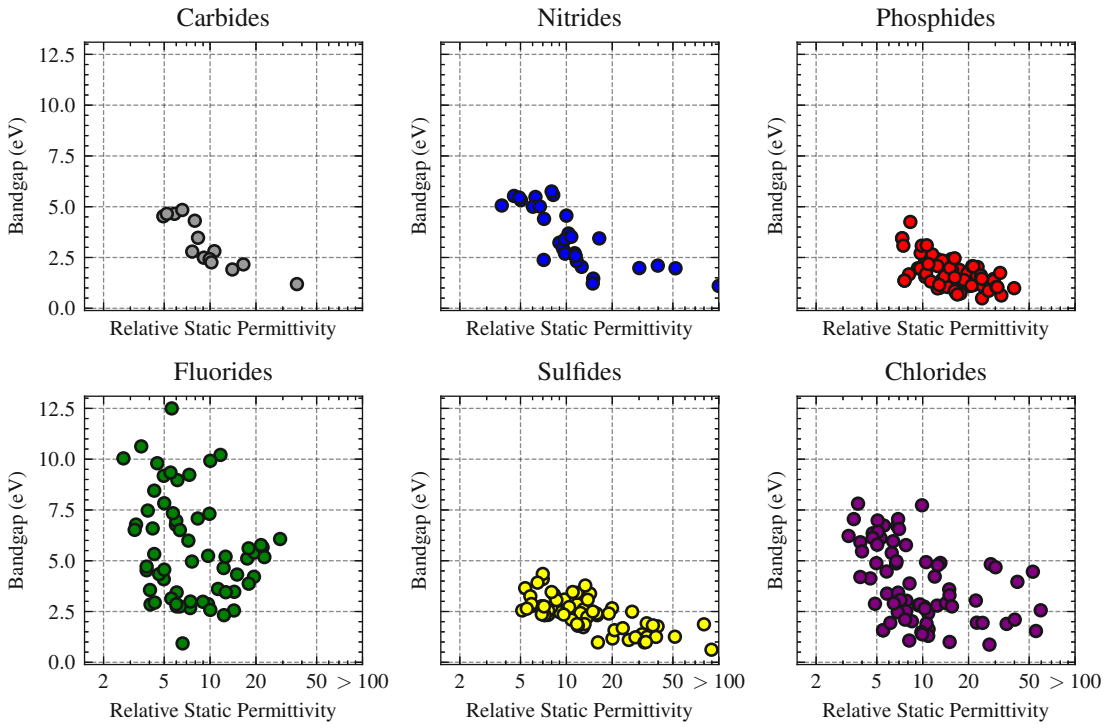

Figure 1.4: Scatterplot of band gap vs. permittivity of different insulator DFT simulations from high-throughput screening of non-oxide dielectrics. Fluorides tend to have the highest band gaps while maintaining decent permittivity. Data from [18].

1.6 Structure of the Thesis

This thesis aims to study fluorides in more detail by first calculating the band gap and permittivity of selected materials using a different, typically more accurate, hybrid functional instead of the previously employed GGA+U approach [18]. This is followed by an investigation of vacancy defects in selected materials. The results serve to verify previous computations and provide more detailed insights into important defects in these materials, offering valuable information for future technology computer aided design (TCAD) simulations. The thesis is structured as follows:

Chapter 2 provides an overview of the employed *ab initio* calculation methods, in particular DFT. The multi-particle Schrödinger equation is introduced, and both the Hartree-Fock method and DFT are discussed. Key computational techniques and approximations for DFT simulations, such as pseudopotentials, are introduced.

The basics of crystal structures and insulators are introduced in Chapter 3. Furthermore, the properties of interest within this thesis, *i.e.* band gap and permittivity, and how to compute them using DFT, are discussed.

An initial screening of materials based on permittivity and band gap is conducted in Chapter 4. The simulation setup used for these calculations is explained, and convergence criteria are discussed. The results of this initial screening of band gap and permittivity are presented yielding LaF_3, BiF_3 as promising candidates with ZrF_4 and CaF_2 as a point of reference.

Chapter 5 analyzes vacancy defects in CaF_2, LaF_3, BiF_3, and ZrF_4. Formation energies for vacancies in different charge states and the associated defect levels are calculated and discussed. In addition, migration paths of these vacancies within the crystal are examined, and the corresponding energy barriers are computed.

The thesis concludes in Chapter 6 with a summary of the findings and an outlook on future work.

CHAPTER 2

AB-INITIO SIMULATION OF MATERIALS

Simulating materials on a computer can be done at various levels of abstraction. "Ab initio", meaning "from the beginning" or "from first principles", refers to simulations based on the laws of quantum mechanics. These methods aim to describe a material as accurately as possible, relying solely on fundamental constants without the need for experimental values.

2.1 Solving the Schrödinger Equation

Quantum mechanics is the theory that describes the behavior of elementary particles such as electrons, protons, and neutrons. The central equation in non-relativistic quantum physics is the Schrödinger equation:

$$i\hbar\frac{\mathrm{d}}{\mathrm{d}t}\Psi = \hat{H}\Psi \tag{2.1}$$

Here, $\hat{H}$ is the Hamiltonian operator, Ψ the wave function, and $\hbar$ the reduced Planck constant. The time-independent Schrödinger equation can be derived by separating the time-dependent wave function into time-independent and time-dependent components, leading to

$$\hat{H}\Psi = E\Psi \tag{2.2}$$

where E is the energy of the system. The time-independent wave function of a single particle in spatial representation is a function in 3D space, $\Psi(\mathbf{r})$. For two particles, the wave function depends on both position vectors, $\Psi(\mathbf{r}_1, \mathbf{r}_2)$. Other representations, such as in momentum space, are not considered in this introductory explanation.

Naïve approach: Suppose one wants to solve the time-independent Schrödinger equation for a many-body system on a computer. A straightforward approach is to define a volume discretized by a grid of points. For simplicity, consider an equidistant grid with N points in each spatial dimension. Each particle adds three dimensions to the problem, so for M particles, the total number of grid points becomes N^{3M}.

Even for modest values, such as $N = 10$ and $M = 6$, which could represent a calculation of electrons in the potential of a carbon atom, this leads to 10^{18} sample points. If only one byte is stored per point, over 1 exabyte of memory would be required. While memory-saving techniques could reduce this somewhat, such a computation might just be feasible on the largest supercomputers in the near future. For example, FRONTIER, the second-ranked machine in the TOP500 list as of November 2024, has 9 petabytes of RAM [26]. However, due to the exponential scaling, even slightly larger systems quickly become intractable-without yet considering the computation time and associated costs.

Approximate solutions: In this thesis, simulations involving hundreds of atoms and thousands of electrons are carried out using approximate solutions to the many-body Schrödinger equation. The two methods which are used in this thesis, Hartree-Fock and DFT, are discussed in the remainder of this chapter.

2.2 Hamiltonian for Interaction of Electrons and Nuclei

In the previous section, the Schrödinger equation was introduced in a general form. The Hamiltonian can describe any quantum system. The (intractable) multi-particle Hamiltonian, used to describe materials, consists of the kinetic and interaction energies between particles and is given in Equation 2.3.

$$\begin{aligned}\hat{H} = &- \overbrace{\frac{\hbar^2}{2m_\mathrm{e}} \sum_i \nabla_i^2}^{\text{electron kin. energy}} - \overbrace{\frac{\hbar^2}{2} \sum_I \frac{1}{M_I} \nabla_I^2}^{\text{nucleus kin. energy}} + \overbrace{\frac{1}{2} \sum_{i \neq j} \frac{e^2}{|\mathbf{r}_i - \mathbf{r}_j|}}^{\text{electron-electron interaction}} \\ &+ \underbrace{\frac{1}{2} \sum_{I \neq J} \frac{Z_I Z_J e^2}{|\mathbf{R}_i - \mathbf{R}_j|}}_{\text{nucleus-nucleus interaction}} - \underbrace{\sum_{i,I} \frac{Z_I e^2}{|\mathbf{r}_i - \mathbf{R}_I|}}_{\text{electron-nucleus interaction}}\end{aligned} \tag{2.3}$$

The small indices i and j are enumerating the electrons and the capital indices I and J are enumerating the nuclei. Furthermore, Z_i and M_i denote the atomic number and atomic mass respectively [27].

2.3 Born-Oppenheimer Approximation

The Born-Oppenheimer approximation assumes that the wave functions of nuclei and electrons can be treated separately, with the total wave function being a

product of the nuclear and electronic wave functions. This is justified by the much larger mass of the nucleus (for hydrogen: $m_p = 1.672 \cdot 10^{-27}$ kg) compared to the electron mass $m_{\text{el}} = 9.109 \cdot 10^{-31}$ kg. The mass difference of over a factor of 10^3 means that nuclei respond to environmental changes much more slowly than electrons. Since both particles experience Coulomb forces of similar magnitude, the heavier nucleus undergoes significantly slower acceleration [28].

The approximation thus assumes that nuclei are stationary while solving the Schrödinger equation for the electrons. From a mathematical perspective, referring to Equation 2.3, this is equivalent to taking the limit $M_I \to \infty$, which effectively removes the nuclear kinetic energy term from the Hamiltonian [27].

$$\hat{H} = -\frac{\hbar^2}{2m_e} \sum_i \nabla_i^2 + \frac{1}{2} \sum_{i \neq j} \frac{e^2}{|\mathbf{r}_i - \mathbf{r}_j|} - \sum_{i,I} \frac{Z_I e^2}{|\mathbf{r}_i - \mathbf{R}_I|} + E_{\text{nucleus-nucleus}} \tag{2.4}$$

The electrons move in a potential created by the fixed positions of the nuclei. The Coulomb interaction between the nuclei contributes only a constant energy shift and does not affect the electronic behavior directly. The resulting electronic Hamiltonian depends solely on the electronic wave function, which largely determines the fundamental properties of a material.

Since the potential energy landscape experienced by the electrons is defined by the atomic positions, the concept of the potential energy surface (PES) can be introduced. It describes the total energy of the system as a function of the atomic coordinates. This approximation is essential for many of the optimization methods used in this thesis.

2.4 Variational Principle

The variational principle is a concise yet fundamental concept that underpins most quantum mechanical ground state calculations. Given a Hamiltonian $\hat{H}$ and a properly normalized trial wave function Ψ_{trial}, such that $\langle \Psi_{\text{trial}} | \Psi_{\text{trial}} \rangle = 1$, the following inequality holds:

$$\langle \Psi_{\text{trial}} | \hat{H} | \Psi_{\text{trial}} \rangle \geq E_0 \tag{2.5}$$

where E_0 is the ground state energy of the true wave function Ψ [29].

In simple terms, the expected energy of any normalized trial wave function is always greater than or equal to the true ground state energy of the system. This allows one to use a set of trial functions and minimize the energy by adjusting their parameters. Such an approach enables efficient optimization algorithms. The computed energy serves as an upper bound for the true ground state energy,

and with a well-chosen trial function, it provides a good approximation of the system's ground state.

2.5 Bloch Theorem

This thesis focuses on crystalline materials, where the potential exhibits the same periodicity as the underlying lattice. An important result that facilitates working with wave functions in such periodic potentials is Bloch's theorem [8, 30].

Theorem. *Let U be the periodic potential in which the particles move, and let $\mathbf{R}$ denote the lattice vectors. The eigenstates $\psi_{n\mathbf{k}}$ of the one-electron Hamiltonian $\hat{H} = -\frac{\hbar^2\nabla^2}{2m} + U(\mathbf{r})$, where $U(\mathbf{r}+\mathbf{R}) = U(\mathbf{r})$ for all $\mathbf{R}$, can be expressed as a product of a plane wave and a function with the periodicity of the Bravais lattice:*

$$\psi_{n\mathbf{k}}(\mathbf{r}) = e^{i\mathbf{k}\cdot\mathbf{r}} u_{n\mathbf{k}}(\mathbf{r}) \tag{2.6}$$

The functions $u_{n\mathbf{k}}(\mathbf{r})$, known as Bloch functions, modulate the plane wave and have the same periodicity as the crystal lattice, that is:

$$u_{n\mathbf{k}}(\mathbf{r}+\mathbf{R}) = u_{n\mathbf{k}}(\mathbf{r}) \tag{2.7}$$

This result implies that, when moving from one primitive cell to another by a lattice vector $\mathbf{R}$, the wave function transforms as

$$\psi(\mathbf{r}+\mathbf{R}) = e^{i\mathbf{k}\cdot\mathbf{R}}\psi(\mathbf{r}) \tag{2.8}$$

Thus, at any periodic point in the crystal, the wave function acquires a phase factor of $\mathbf{k}\cdot\mathbf{R}$. The vector $\mathbf{k}$ lies in reciprocal space and represents the crystal momentum of the electron. Crystal momentum is not identical to the momentum of a free particle, as reciprocal lattice vectors can be added to it obtaining equivalent vectors.

2.6 Hartree-Fock Method

As previously discussed, solving the many-body Schrödinger equation directly is infeasible for all but the simplest systems. However, a mean-field approach can simplify the problem by treating each electron independently, with each electron experiencing an average interaction due to the presence of all others.

Equation 2.4, which results from the Born-Oppenheimer approximation, is now decomposed into separate equations for each electron. This approach neglects electron-electron correlation effects, making the problem more tractable.

In this approximation, the total wave function is expressed as a product of single-particle wave functions ψ_i for each electron i:

$$\Psi = \psi_1(\mathbf{r}_1) \cdot \psi_2(\mathbf{r}_2) \cdot ... \cdot \psi_N(\mathbf{r}_N) \tag{2.9}$$

The kinetic energy term and the electron-nucleus interaction for each electron remain unchanged, as they are independent of the other electrons. The electron-electron interaction term, however, is approximated by the average interaction with the surrounding electron density ρ, which represents the collective influence of all other electrons [31]. Thus, the second term in Equation 2.4 is replaced by

$$\sum_{i \neq j} \frac{e^2}{|\mathbf{r}_i - \mathbf{r}_j|} \rightarrow -e \int \frac{\rho(\mathbf{r})}{|\mathbf{r}_i - \mathbf{r}|} \, \mathrm{d}^3 r \tag{2.10}$$

where the total electron density $\rho(\mathbf{r})$ is defined as

$$\rho(\mathbf{r}) = -e \sum_i |\psi_i(\mathbf{r})|^2 \tag{2.11}$$

which represents the probability density of finding an electron at a given position, multiplied by the electron charge.

These approximations lead to the Hartree equations 2.12, a set of equations describing the behavior of the single electrons:

$$\hat{H}_{\text{Hartree}} \psi_i = \left(-\frac{\hbar^2}{2m_e} \nabla^2 + \int \sum_j |\psi_j(\mathbf{r}')|^2 \frac{e^2}{|\mathbf{r} - \mathbf{r}'|} \, \mathrm{d}^3 r' - \sum_I \frac{Z_I e^2}{|\mathbf{r}_i - \mathbf{R}_I|} \right) \psi_i = E_i \psi_i \tag{2.12}$$

Fermions require antisymmetric wave functions, a condition not accounted for in Equation 2.12. To include this requirement, one must first recognize that the Hartree equations can also be derived using the variational principle, assuming the wave function is a product of single-particle wave functions [32, 33]. However, such a product wave function is not antisymmetric. A general antisymmetric wave function can be constructed using a Slater determinant. In this context, the quantity minimized is the expectation value of the Hamiltonian, which corresponds to the total energy of the system. Evaluating this expectation value for a trial wave function built from a Slater determinant (with orthonormal

single-particle wave functions) yields [8]

$$\begin{aligned} E[\Psi] = \sum_i \int \psi_i^*(\mathbf{r}) \left(-\frac{\hbar^2}{2m_e}\nabla^2 - \sum_I \frac{Z_I e^2}{|\mathbf{r}_i - \mathbf{R}_I|} \right) \psi_i(\mathbf{r})\, \mathrm{d}^3 r \\ + \frac{1}{2} \sum_{i,j} \int\int \psi_i^*(\mathbf{r}) \psi_j^*(\mathbf{r}') \frac{e^2}{|\mathbf{r} - \mathbf{r}'|} \psi_i(\mathbf{r}) \psi_j(\mathbf{r}')\, \mathrm{d}^3 r\, \mathrm{d}^3 r' \\ - \frac{1}{2} \sum_{i,j} \delta_{\sigma_i,\sigma_j} \int\int \psi_i^*(\mathbf{r}) \psi_j^*(\mathbf{r}') \frac{e^2}{|\mathbf{r} - \mathbf{r}'|} \psi_i(\mathbf{r}') \psi_j(\mathbf{r})\, \mathrm{d}^3 r\, \mathrm{d}^3 r' \end{aligned} \tag{2.13}$$

Notice that the second term in the energy expression corresponds to the electron-electron interaction, as in the Hartree equations 2.12. The factor of $1/2$ accounts for the double counting of pairwise interactions.

Applying the variational principle to minimize the total energy, as expressed in Equation 2.13, leads to the Hartree-Fock equations [34, 35]

$$\hat{H}_{\text{Hartree}} \psi_i(\mathbf{r}) - \sum_j \delta_{\sigma_i,\sigma_j} \int \frac{e^2}{|\mathbf{r} - \mathbf{r}'|} \psi_j^*(\mathbf{r}') \psi_j(\mathbf{r}) \psi_i(\mathbf{r}')\, d\mathbf{r}' = E_i \psi_i(\mathbf{r}) \tag{2.14}$$

where, σ_i denotes the spin of the electron. The additional term is known as the *exchange term*, which arises from the requirement of antisymmetry in the total wave function. It takes the form of an integral operator, making the equation complex to solve [8]. Nevertheless, hybrid potentials based on the Hartree-Fock method are commonly used in DFT calculations and will be discussed in a later chapter.

2.7 Density Functional Theory

Density functional theory (DFT) is another approximation widely used in current material science due to its accurate prediction of many material parameters. It is based on the Hohenberg-Kohn theorems, which state that a systems properties are completely determined by the ground-state electron density $\rho_0(\mathbf{r})$ [36]. $\rho_0(\mathbf{r})$ is a function in three dimensions regardless of the number of particles in the system which avoids the exponential scaling problem discussed earlier. DFT is not necessarily the most accurate method that can be used, but it can be efficiently computed and gives decent results for many materials.

2.7.1 Hohenberg-Kohn Theorems

The Hohenberg-Kohn theorems provide the theoretical foundation of density functional[1] theory.

Theorem. *For any system of interacting particles in an external potential $V_{ext}(\mathbf{r})$, the potential, and thus the Hamiltonian, is uniquely determined up to a constant by the ground-state particle density ρ_0 [27].*

Proof Sketch. Towards contradiction: Assume that two different external potentials V_{ext}^1 and V_{ext}^2, differing by more than a constant, yield the same ground state density $\rho_0(\mathbf{r})$. These lead to different Hamiltonians $\hat{H}^1$ and $\hat{H}^2$ with corresponding ground state wave functions Ψ^1 and Ψ^2, both associated with $\rho_0(\mathbf{r})$.

Assuming non-degeneracy of the ground state and using the variational principle:

$$\langle\Psi^1|\hat{H}^1|\Psi^1\rangle < \langle\Psi^2|\hat{H}^1|\Psi^2\rangle = \langle\Psi^2|\hat{H}^2|\Psi^2\rangle + \langle\Psi^2|\hat{H}^1 - \hat{H}^2|\Psi^2\rangle$$

Similarly:

$$\langle\Psi^2|\hat{H}^2|\Psi^2\rangle < \langle\Psi^1|\hat{H}^2|\Psi^1\rangle = \langle\Psi^1|\hat{H}^1|\Psi^1\rangle + \langle\Psi^1|\hat{H}^2 - \hat{H}^1|\Psi^1\rangle$$

Combining both:

$$E_0^1 < E_0^2 + \langle\Psi^2|\hat{H}^1 - \hat{H}^2|\Psi^2\rangle \quad \text{and} \quad E_0^2 < E_0^1 + \langle\Psi^1|\hat{H}^2 - \hat{H}^1|\Psi^1\rangle$$

Adding these inequalities gives:

$$E_0^1 + E_0^2 < E_0^1 + E_0^2$$

which is a contradiction. □

An important corollary of this theorem is that all observables of the system, including the ground state energy, are functionals of the density $\rho(\mathbf{r})$ [27]. Using this result, the second Hohenberg-Kohn theorem can be stated:

Theorem. *A universal energy functional $E[\rho]$ exists in terms of the density $\rho(\mathbf{r})$, valid for any external potential $V_{ext}(\mathbf{r})$. For a given $V_{ext}(\mathbf{r})$, the exact ground state energy is the global minimum of this functional, and the density $\rho(\mathbf{r})$ that minimizes it is the exact ground state density $\rho_0(\mathbf{r})$ [27].*

[1] A functional is a function that takes a function as an argument and returns a scalar.

Proof Sketch. Let E_0 be the ground state energy corresponding to the wave function Ψ_0 and density $\rho_0(\mathbf{r})$, and let $E[\rho]$ be the energy functional of the density:

$$E_0 = E[\rho_0] = \langle \Psi_0 | \hat{H} | \Psi_0 \rangle$$

Now, consider any other density $\rho'(\mathbf{r})$ with corresponding wave function Ψ'. By the variational principle:

$$E[\rho_0] = \langle \Psi_0 | \hat{H} | \Psi_0 \rangle < \langle \Psi' | \hat{H} | \Psi' \rangle = E[\rho']$$

Therefore, minimizing the functional $E[\rho]$ with respect to $\rho(\mathbf{r})$ yields the ground state energy and the exact ground state density. □

2.7.2 Kohn-Sham Equations

The Hohenberg-Kohn theorems establish the existence of a functional $E[\rho]$ for the ground state energy, but they do not provide its explicit form. To construct such a density, Kohn and Sham proposed an approximation by introducing an auxiliary system of non-interacting electrons that reproduces the same ground-state density as the real interacting system. The electron density of this system is given by:

$$\rho(\mathbf{r}) = \sum_{\sigma} \sum_{i=1}^{N_\sigma} |\psi_i^\sigma(\mathbf{r})|^2$$

where σ denotes the spin state and $\psi_i^\sigma(\mathbf{r})$ is the wave function of the corresponding electron. The Kohn-Sham total energy functional is written as:

$$E[\rho] = T_s[\rho] + E_{\text{Hartree}}[\rho] + E_{\text{xc}}[\rho] + E_{\text{ext}}[\rho] + E_{\text{nucleus-nucleus}} \tag{2.15}$$

Here, $T_s[\rho]$ is the kinetic energy of the non-interacting reference system, given by:

$$T_s[\rho] = -\frac{\hbar^2}{2m_e} \sum_{\sigma} \sum_{i}^{N_\sigma} \langle \psi_i^\sigma | \nabla^2 | \psi_i^\sigma \rangle \tag{2.16}$$

Although $T_s[\rho]$ depends on the wave functions rather than directly on the density, the first Hohenberg-Kohn theorem ensures that the ground-state density $\rho(\mathbf{r})$ uniquely determines the external potential $V_{\text{ext}}(\mathbf{r})$, and therefore also the wave functions. Thus, T_s is still considered a functional of ρ. The external and Hartree energy contributions can be written directly in terms of the density:

$$E_{\text{ext}}[\rho] = \int \rho(\mathbf{r}) V_{\text{ext}}(\mathbf{r}) \, \mathrm{d}^3 r \tag{2.17}$$

$$E_{\text{Hartree}}[\rho] = \frac{1}{2} \int \frac{\rho(\mathbf{r})\rho(\mathbf{r}')}{|\mathbf{r} - \mathbf{r}'|} \, \mathrm{d}^3 r \, \mathrm{d}^3 r' \tag{2.18}$$

$E_{\text{Hartree}}[\rho]$ represents the classical electrostatic interaction energy of the charge distribution $\rho(\mathbf{r})$. The remaining term, $E_{\text{xc}}[\rho]$, is the exchange-correlation energy. It captures the many-body quantum effects beyond the non-interacting kinetic energy and the classical Coulomb interaction:

$$E_{\text{xc}}[\rho] = \langle \hat{T} \rangle - T_s[\rho] + \langle \hat{U}_{\text{el-el int}} \rangle - E_{\text{Hartree}}[\rho] \tag{2.19}$$

Here, $\langle \hat{T} \rangle$ and $\langle \hat{U}_{\text{el-el int}} \rangle$ are the expectation values of the kinetic energy and the electron-electron interaction energy of the true many-body system. This is the main source of approximation in DFT, in addition to the Born-Oppenheimer approximation. The exchange-correlation energy must be approximated as a functional of the density, which is discussed in more detail in Sec. 2.7.4. To find the ground-state density, the total energy functional is minimized using variational calculus [27].

The density is expressed in terms of the wave functions and inserted into the functionals $E_{\text{ext}}[\rho]$, $E_{\text{Hartree}}[\rho]$ and $E_{\text{xc}}[\rho]$. The resulting functional is minimized with respect to these orthogonal wave functions keeping in mind the chain rule and using Lagrange multipliers. This yields the Kohn-Sham equations [27]

$$\left(-\frac{\hbar^2}{2m_e} \nabla^2 + V_{\text{KS}}^{\sigma}(\mathbf{r}) \right) \psi_i^{\sigma}(\mathbf{r}) = \varepsilon_i^{\sigma} \psi_i^{\sigma}(\mathbf{r}) \tag{2.20}$$

with the Kohn-Sham potential defined as:

$$V_{\text{KS}}^{\sigma}(\mathbf{r}) = V_{\text{ext}}(\mathbf{r}) + \frac{\delta E_{\text{Hartree}}}{\delta \rho(\mathbf{r}, \sigma)} + \frac{\delta E_{\text{xc}}}{\delta \rho(\mathbf{r}, \sigma)} \tag{2.21}$$

Here, $\frac{\delta}{\delta \rho}$ denotes the functional derivative with respect to the electron density.

2.7.3 Solving the Kohn-Sham Equations

A solution to the Kohn-Sham equations, given the potential $V_{\text{KS}}^{\sigma}(\mathbf{r})$, consists of a set of wave functions $\psi_i(\mathbf{r})$ and their corresponding eigenenergies ε_i. These wave functions determine the electron density $\rho(\mathbf{r})$, which in turn defines the potential $V_{\text{KS}}^{\sigma}(\mathbf{r})$, creating a circular dependency. To resolve this, the system is solved self-consistently. One begins with an initial guess for the spin-dependent density ρ^{σ}, computes the corresponding potential, and solves the Kohn-Sham equations. The resulting wave functions yield a new density, which is then used to update the potential [27]. This process is repeated iteratively until convergence is reached, as illustrated in Fig. 2.1.

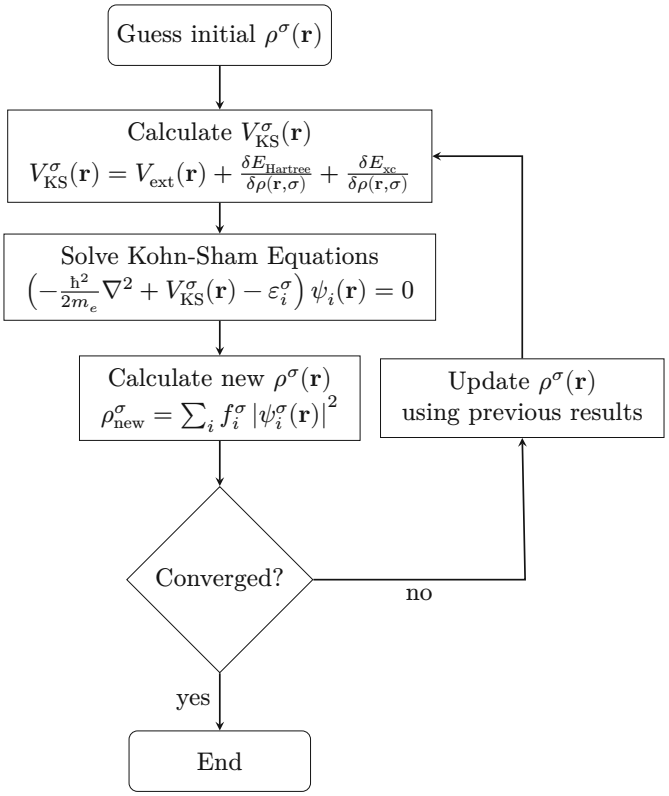

Figure 2.1: Iteration process for solving the Kohn-Sham equations. The convergence of the process can for example be determined by comparing the old and new density. If the difference is smaller than a certain threshold, the process is considered converged. Adapted from [27]

There are several methods to update the density ρ after each iteration. The simplest approach is to take a linear combination of the previous and current densities. More advanced techniques, such as Broyden mixing or Kerker mixing, are often employed to accelerate convergence [27]. Alternatively, methods like the orbital transformation approach directly exploit the orthonormality constraints of the wave functions [37, 38].

2.7.4 Exchange-Correlation Functionals

Up to this point, the exchange-correlation functional $E_{\mathrm{xc}}[\rho]$ has only been defined in general terms, without specifying its explicit form. This is because the exact form of the functional is currently unknown. Nevertheless, several approximations are commonly used in practice and yield good results for a wide

range of materials. The choice of approximation strongly affects the accuracy and reliability of simulation results.

For convenience and consistency with the literature, atomic units will be used for the remainder of this chapter. This means that the elementary charge e, the reduced Planck constant $\hbar$, the electron mass m_e, and the Bohr radius a_0 are all set to 1.

Local Density Approximation

Kohn and Sham introduced the local density approximation (LDA) as the first practical approximation to the exchange-correlation functional [39]. It is based on the homogeneous electron gas, for which the exchange-correlation contributions are well known. The key assumption is that, locally, the electron gas in a material behaves like a homogeneous electron gas. This approximation is valid primarily for systems with slowly varying electron densities. In the LDA, the exchange-correlation energy depends only on the local value of the density and is written as an integral over space:

$$E_{\mathrm{xc}}^{\mathrm{LDA}}[\rho] = \int \rho(\mathbf{r})\varepsilon_{\mathrm{xc}}(\rho(\mathbf{r}))\ \mathrm{d}^3r = \int \rho(\mathbf{r})\left(\varepsilon_{\mathrm{x}}(\rho(\mathbf{r})) + \varepsilon_{\mathrm{c}}(\rho(\mathbf{r}))\right)\ \mathrm{d}^3r \tag{2.22}$$

For the homogeneous electron gas, the exchange energy can be derived from the Thomas-Fermi model. It is given by [40]:

$$\varepsilon_{\mathrm{x}}(\rho) = -\frac{3}{4}\left(\frac{3}{\pi}\right)^{1/3}\rho^{1/3} \tag{2.23}$$

While no analytic expression exists for the correlation energy, accurate results have been obtained from Monte Carlo simulations [41].

An extension of this model accounts for the electron spin. By using separate densities $\rho^{\uparrow}$ and $\rho^{\downarrow}$ for spin-up and spin-down electrons, the exchange-correlation energy is evaluated independently for each spin channel. This leads to the local spin density approximation (LSDA) [27].

Generalized Gradient Approximation

As the name suggests, the GGA includes not only the local electron density but also its gradient. One limitation of the LDA is its assumption of slowly varying densities, which is addressed by incorporating the density gradients in the GGA. The general form of the exchange-correlation functional in the GGA is [27]

$$E_{\mathrm{xc}}^{\mathrm{GGA}}[\rho] = \int \rho(\mathbf{r})\varepsilon_{\mathrm{xc}}(\rho^{\uparrow}(\mathbf{r}), \rho^{\downarrow}(\mathbf{r}), \nabla\rho^{\uparrow}(\mathbf{r}), \nabla\rho^{\downarrow}(\mathbf{r}))\ \mathrm{d}^3r \tag{2.24}$$

Here, $\nabla\rho(\mathbf{r})$ appears as a new argument, and the spin dependence is explicitly included, which is not the case in the plain LDA.

A widely used GGA functional in solid-state physics is the Perdew-Burke-Ernzerhof (PBE) functional. It has been shown to improve upon LDA for a broad range of materials [42, 43]. For example, it corrects the over-binding tendency of LDA, which often results in underestimated lattice constants. However, GGA is slightly more computationally expensive. Other GGA functionals, such as Perdew-Wang 1991 (PW91) [44] or PBEsol [45], which is optimized for solids, are also in use. The wide range of available functionals reflects the fact that there is no single best choice for all applications. The selection of an appropriate functional depends on the specific material system and the properties of interest.

Hybrid Functionals

A well-known limitation of the LDA and GGA functionals is their tendency to underestimate the band gap of materials [46]. Since this thesis focuses on accurately predicting band gaps in insulators, hybrid functionals are of particular interest [47]. These functionals improve upon LDA and GGA by incorporating a fraction of Hartree-Fock exchange, which typically overestimates the band gap. The Hartree-Fock method, discussed in Sec. 2.6, forms the basis for hybrid functionals. Specifically, the exchange energy term from Equation 2.14 is used to enhance the exchange-correlation functional in DFT [27]:

$$E_{\mathrm{x}}^{\mathrm{HF}} = -\frac{1}{2}\sum_i\sum_j \delta_{\sigma_i,\sigma_j}\int\int \psi_i^*(\mathbf{r})\psi_j^*(\mathbf{r}')g(|\mathbf{r}-\mathbf{r}'|)\psi_i(\mathbf{r}')\psi_j(\mathbf{r})\ \mathrm{d}^3r\ \mathrm{d}^3r' \quad (2.25)$$

where $g(r)$ is the Coulomb operator:

$$g(r) = \frac{1}{r} \quad (2.26)$$

This Hartree-Fock exchange is mixed with a GGA or LDA exchange-correlation functional to form the hybrid functional:

$$E_{\mathrm{xc}}^{\mathrm{Hybrid}} = \alpha E_{\mathrm{x}}^{\mathrm{HF}}[\rho] + (1-\alpha)E_{\mathrm{x}}^{\mathrm{GGA}}[\rho] + E_{\mathrm{c}}^{\mathrm{GGA}}[\rho] \quad (2.27)$$

A widely used example is the PBE0 functional [48], which combines the PBE GGA functional with Hartree-Fock exchange using a mixing parameter $\alpha = 0.25$:

$$E_{\mathrm{xc}}^{\mathrm{PBE0}} = \frac{1}{4}E_{\mathrm{x}}^{\mathrm{HF}}[\rho] + \frac{3}{4}E_{\mathrm{x}}^{\mathrm{PBE}}[\rho] + E_{\mathrm{c}}^{\mathrm{PBE}}[\rho] \quad (2.28)$$

To reduce computational cost, truncated or range-separated hybrid functionals are often used. In truncated hybrids, the Coulomb operator is modified to include

only short-range interactions:

$$g(r) = \begin{cases} \frac{1}{r} & \text{if } r < r_s \\ 0 & \text{if } r \geq r_s \end{cases} \tag{2.29}$$

An example is the PBE0_TC_LRC functional, which is based on PBE0 [49].

Range-separated functionals divide the interaction into short- and long-range parts:

$$E_{\text{xc}}^{\text{Hybrid}} = \alpha E_{\text{xc}}^{\text{HF,SR}}(\mu)[\rho] + (1-\alpha) E_{\text{x}}^{\text{GGA,SR}}(\mu)[\rho] + E_{\text{x}}^{\text{GGA,LR}}(\mu)[\rho] + E_{\text{c}}^{\text{GGA}}[\rho] \tag{2.30}$$

The parameter μ is a screening parameter that defines the separation between short- and long-range interactions. A prominent example is the HSE06 functional, which, like PBE0_TC_LRC, is based on the PBE functional and uses $\alpha = 0.25$:

$$E_{\text{XC}}^{\text{HSE06}} = \frac{1}{4} E_{\text{x}}^{\text{HF,SR}}(\mu)[\rho] + \frac{3}{4} E_{\text{x}}^{\text{PBE,SR}}(\mu)[\rho] + E_{\text{x}}^{\text{PBE,LR}}(\mu)[\rho] + E_{\text{c}}^{\text{PBE}}[\rho] \tag{2.31}$$

The Coulomb operator is split using the error function erf and its complement erfc:

$$g(r) = \frac{\text{erfc}(\mu r)}{r} + \frac{\text{erf}(\mu r)}{r} \tag{2.32}$$

with

$$\text{erf}(x) = \frac{2}{\sqrt{\pi}} \int_0^x e^{-t^2}\, dt, \quad \text{erfc}(x) = 1 - \text{erf}(x) \tag{2.33}$$

The short-range part is used in the Hartree-Fock exchange, while the long-range part is excluded, leading to an effective Coulomb operator:

$$g(r) = \frac{\text{erfc}(\mu r)}{r} \tag{2.34}$$

This smoothly transitions between short and long-range interactions, similar in effect to the truncated operator but without a hard cutoff, as illustrated in Fig. 2.2. In the limit $\mu = 0$, the HSE06 functional reduces to PBE0 [50]. In the HSE06 functional, the screening parameter $\mu = 0.11$ Bohr is used [51]. This value has been shown to provide good band gap estimates for typical semiconductors. In a study by Garza *et al.* [52], HSE06 achieved a mean absolute percent error of approximately 15%, outperforming other hybrid functionals such as PBE0.

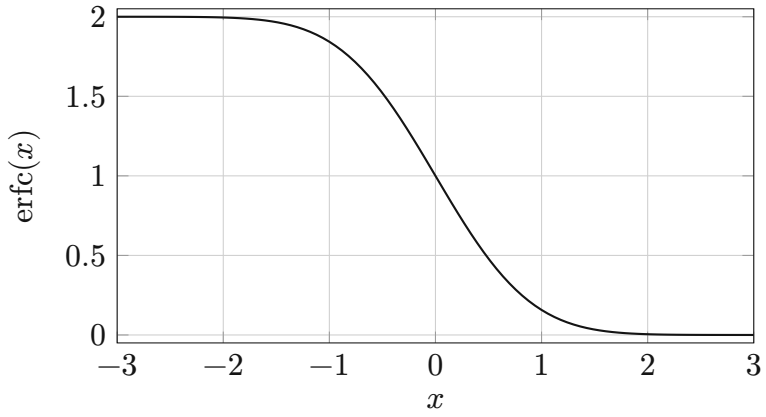

Figure 2.2: Plot of the complementary error function erfc(x).

2.7.5 Basis Sets

The second step in the iterative process shown in Fig. 2.1 is solving the Kohn-Sham equations 2.20. To do this, the wave functions $\psi_i(\mathbf{r})$ are expressed as a linear combination of basis functions. The theoretical foundation for this approach lies in function spaces, where a given function can be represented by a linear combination of suitable basis functions, possibly infinite in number. A well-known example is the Taylor series expansion, where the basis functions are monomials x^n, and the space of representable functions consists of analytic functions [53].

In DFT calculations, the electronic wave functions are similarly expanded in a basis set, although the number of basis functions must be finite due to computational constraints. The most commonly used basis sets are plane waves and Gaussian functions. In practice, a trade-off must be made between the number of basis functions and the ability to approximate the true wave function accurately. This trade-off directly affects the computational cost and the error introduced in the calculation.

Plane Waves

Considering the Fourier series, any square-integrable periodic function can be represented by a set of plane waves. To simplify the formulation, it is convenient to normalize the wave functions to the volume Ω:

$$\psi_i(\mathbf{r}) = \frac{1}{\sqrt{\Omega}} \sum_{\mathbf{q}} c_{i,\mathbf{q}} e^{i\mathbf{q}\cdot\mathbf{r}} \tag{2.35}$$

The plane waves must be orthonormal with respect to the standard inner product:

$$\frac{1}{\Omega}\int_{\Omega} e^{-i\mathbf{q}'\cdot\mathbf{r}} e^{i\mathbf{q}\cdot\mathbf{r}}\,\mathrm{d}^3r = \delta_{\mathbf{q},\mathbf{q}'} \tag{2.36}$$

If the effective potential $V_{\mathrm{KS}}^{\sigma}(\mathbf{r})$ in Equation 2.21 is also expanded in a Fourier series, and the wave vector is written as $\mathbf{q} = \mathbf{k} + \mathbf{G}_m$, the Kohn-Sham equations can be rewritten in matrix form:

$$\frac{1}{2}\sum_{m'}\left(|\mathbf{k}+\mathbf{G}_m|^2\delta_{m,m'} + V_{\mathrm{eff}}(\mathbf{G}_m - \mathbf{G}_{m'})\right)\mathbf{c}_{i,m'}(\mathbf{k}) = \varepsilon_i(\mathbf{k})\mathbf{c}_{i,m}(\mathbf{k}) \tag{2.37}$$

Here, $\mathbf{G}_m$ are reciprocal lattice vectors of the crystal and $\mathbf{k}$ is the wave vector within the first Brillouin zone. Although there are infinitely many $\mathbf{G}_m$ vectors, a finite number must be used in practice. This is controlled by an energy cutoff, which restricts the included plane waves based on their kinetic energy [27]. Only those plane waves whose kinetic energy is below this cutoff are considered in the calculation.

A challenge arises because components of the wave function with high spatial frequency, typically near the atomic core, require very large cutoffs to be resolved accurately. Electrons near the nucleus possess high kinetic energies and contribute significantly to this issue. For many applications, however, it is sufficient to focus on the valence electrons, as they are primarily responsible for chemical bonding. The core electrons can be treated using pseudopotentials, which will be introduced later.

Gaussian Basis

Instead of using completely delocalized plane waves, alternative basis sets can be employed that align more closely with the chemical intuition of localized orbitals. These basis functions are centered around each nucleus, aiming to represent the wave function more efficiently, particularly near atomic cores. However, unlike plane waves, these functions are not orthogonal, which introduces the need for an overlap matrix $S_{ij} = \langle\phi_i|\phi_j\rangle$, resulting in a generalized eigenvalue problem. The basis functions commonly used today are inspired by Slater-type orbitals, which are defined as [54]

$$\varphi(r,\theta,\phi)_{n,l,m} = r^{n-1}e^{-\alpha r}Y_{l,m}(\theta,\phi) \tag{2.38}$$

where $Y_{l,m}(\theta,\phi)$ are the spherical harmonics and α is a parameter.

Shavitt and Karplus demonstrated that these Slater-type orbitals can be approximated using Gaussian functions, based on the identity:

$$e^{-\zeta r} = \frac{\zeta}{2\sqrt{\pi}}\int_0^{\infty} s^{-\frac{3}{2}}\exp\left(-\frac{\zeta^2}{4s}\right)\exp(-sr^2)\,\mathrm{d}s \tag{2.39}$$

This transformation enables more efficient computation [55], though the identity itself is not directly used in practice. Instead, Gaussian-type basis functions are introduced in the form:

$$\varphi'(r,\theta,\phi)_{n,l,m} = r^{n-1}e^{-\alpha r^2}Y_{l,m}(\theta,\phi) \tag{2.40}$$

Further optimization is achieved by contracting several of these Gaussian primitives. This replaces the continuous integral in Equation 2.39 with a discrete sum using pre-optimized coefficients c_{in} and exponents α_{in} [56]:

$$\varphi''(r,\theta,\phi)_{n,l,m} = r^{n-1}\sum_i c_{in}e^{-\alpha_{in}r^2}Y_{l,m}(\theta,\phi) \tag{2.41}$$

This expression shows that, unlike plane wave methods where the representation quality is controlled by a single cutoff energy, the quality of Gaussian basis sets depends on multiple parameters. Today, a wide variety of Gaussian basis sets are available, with the coefficients c_{in} and exponents α_{in} carefully optimized for each element to best approximate its wave function [57].

Gaussian Plane Waves

The Gaussian plane waves (GPW) method combines the ideas of Gaussian and plane wave basis sets. Gaussian basis functions, while efficient for representing localized orbitals, are not directly applicable to periodic systems because they are not inherently periodic. To address this, the Gaussian basis functions are made periodic by summing over their periodic images:

$$\varphi_i^{\mathrm{P}}(\mathbf{r}) = \sum_{\mathbf{R}}\varphi_i(\mathbf{r}-\mathbf{R}) \tag{2.42}$$

Because the resulting functions are periodic, they can also be expressed using a Fourier series, allowing a dual representation in reciprocal (plane wave) space:

$$\rho(\mathbf{r}) = \sum_{\mathbf{G}}\rho(\mathbf{G})e^{i\mathbf{G}\cdot\mathbf{r}} = \sum_{\mu\nu}P_{\mu\nu}\varphi_\mu^{\mathrm{P}}(\mathbf{r})^*\varphi_\nu^{\mathrm{P}}(\mathbf{r}) \tag{2.43}$$

Here, $\underline{\mathbf{P}}$ is the density matrix expressed in the chosen Gaussian basis. This dual representation allows using whichever basis is more suitable for a particular part of the calculation, improving computational efficiency [58, 59].

Gaussian Augmented Plane Waves

The Gaussian augmented plane waves (GAPW) approach extends the GPW method by replacing the usual density expansion with coefficients $P_{\mu\nu}$, as seen in Equation 2.43, with the following decomposition:

$$\rho(\mathbf{r}) = \tilde{\rho}(\mathbf{r}) + \sum_A \rho_A(\mathbf{r}) - \sum_A \tilde{\rho}_A(\mathbf{r}) \tag{2.44}$$

In this formulation, the total electron density is separated into smooth and atom-centered components. $\tilde{\rho}(\mathbf{r})$ is a smooth density extended over all space, while $\rho_A(\mathbf{r})$ and $\tilde{\rho}_A(\mathbf{r})$ are atom-centered hard and soft densities, respectively [59].

$$\begin{aligned} \tilde{\rho}(\mathbf{r}) &= \frac{1}{\Omega} \sum_{\mathbf{G}} \rho(\mathbf{G}) e^{i\mathbf{G}\cdot\mathbf{r}} \\ \rho_A(\mathbf{r}) &= \sum_{\mu\nu} P^A_{\mu\nu} \varphi^P_\mu(\mathbf{r}) \varphi^{P*}_\nu(\mathbf{r}) \\ \tilde{\rho}_A(\mathbf{r}) &= \sum_{\mu\nu} \tilde{P}^A_{\mu\nu} \varphi^P_\mu(\mathbf{r}) \varphi^{P*}_\nu(\mathbf{r}) \end{aligned} \tag{2.45}$$

This partitioning improves the representation of the electron density near atomic cores using fewer basis functions, and follows an idea similar to that of pseudopotentials, discussed in Sec. 2.7.6. The GAPW method was originally developed for all-electron calculations, where no pseudopotentials are used. However, it can also be combined with pseudopotentials to further reduce the required energy cutoff [59–61].

Comparison

The choice of basis set depends on the material and the properties of interest. Plane waves are intrinsically periodic, orthogonal, and conceptually simple. Additionally, the size of the basis set can be systematically increased by raising the kinetic energy cutoff. Increasing the size of the basis set is less straightforward for a Gaussian basis. However, plane waves require a large number of functions to accurately describe the wave function near atomic nuclei and to capture the shape of orbitals, which can become computationally demanding.

In contrast, Gaussian basis sets are better suited to represent wave functions near nuclei and are particularly useful in computational chemistry. Their non-periodic nature makes them well-suited for isolated systems such as single molecules. Due to their computational advantages, the GPW and GAPW methods are increasingly used in solid-state physics. However, these methods are conceptually more complex: the basis functions are not orthogonal, the density representation is more involved, and the basis depends on the atomic positions. This positional dependence must be taken into account when comparing systems with different atomic configurations.

There is no universally best basis set and various codes support different sets. In this thesis, the GAPW method combined with pseudopotentials was chosen,

as it provides a good balance between computational efficiency and accuracy of forces for a given cutoff. This section does not aim to be exhaustive and focuses primarily on the basis sets used in this work. For a more comprehensive discussion, the reader is referred to the literature [27, 62].

2.7.6 Pseudopotentials

Most relevant phenomena in quantum chemistry are governed primarily by the outer-shell (valence) electrons [27]. Core electrons are tightly bound to the nucleus and do not significantly contribute to the electronic structure relevant for bonding or other material properties. However, their high kinetic energies make them computationally expensive to treat explicitly.

Since the wave functions of core electrons are only weakly influenced by the chemical environment, their effects can be incorporated as an auxiliary potential. Pseudopotentials take advantage of this by replacing the explicit treatment of core electrons with an effective potential for each atomic species. This greatly reduces the computational cost while retaining sufficient accuracy for most applications [27].

Several types of pseudopotentials (PPs) exist, including ultrasoft pseudopotentials [63], projector augmented wave (PAW) methods [64], and norm-conserving pseudopotentials. The latter are discussed in more detail here, as they are used in the calculations presented in this thesis.

The central idea is to modify the potential in such a way that, after removing the core electron wave functions and incorporating their effects into the potential, the remaining valence electrons behave as if the core electrons were still present. To validate this approximation, the pseudo wave functions of the valence electrons are compared to the corresponding all-electron wave functions of the full system.

Norm-conserving Pseudopotentials

A key requirement for any PP is transferability, meaning it should yield accurate results across different chemical environments. In 1979, Hamann *et al.* introduced criteria for constructing norm-conserving pseudopotentials and proposed a method for generating them [65]:

- The eigenvalues of the pseudo and all-electron valence states must agree for selected reference configurations.
- The all-electron and pseudo valence wave functions must match beyond a chosen core radius r_c.

- For $r > r_c$, the integrated charge densities of the all-electron and pseudo wave functions must be equal for each valence state, ensuring norm conservation: $\int_0^r \rho(\mathbf{r})\ \mathrm{d}^3 r$ is the same for both systems.
- The logarithmic derivatives and their first energy derivatives of the all-electron and pseudo wave functions must also agree for $r > r_c$.

The last two conditions are important for ensuring the accuracy and transferability of the pseudopotential. They guarantee that, beyond the core region, the electronic potential and scattering behavior are effectively the same as in the all-electron system [65].

GTH Pseudopotential

The PP used in the calculations conducted in this thesis is the GTH pseudopotential, developed by Goedecker, Teter, and Hutter [66]. This analytic PP is characterized by at most seven parameters per element for those in the first two rows of the periodic table. It is designed to have favorable decay properties in both real and reciprocal (Fourier) space, making it efficient and well-suited for solid-state simulations. The GTH PP is composed of a local and a non-local part, with the total potential given by:

$$V_{\mathrm{PP}}(r) = V_{\mathrm{loc}}(r) + \sum_{l}^{l_{\max}} V_{\mathrm{nl}}^{l}(r) \tag{2.46}$$

The local part has the following analytic form [67]:

$$\begin{aligned} V_{\mathrm{loc}}(r) = &- \frac{Z_{\mathrm{ion}}}{r} \operatorname{erf}\left(\frac{r}{\sqrt{2} r_{\mathrm{c}}}\right) \\ &+ \exp\left(-\frac{1}{2}\left(\frac{r}{r_{\mathrm{c}}}\right)^2\right) \sum_{i=1}^{4} C_i \left(\frac{r}{r_c}\right)^{2i-2} \end{aligned} \tag{2.47}$$

Here, Z_{ion} is the ionic (nuclear) charge, r_{c} is the cutoff radius, and C_i are element-specific optimized coefficients. The non-local part of the Hamiltonian is expressed as [67]

$$V_{\mathrm{nl}}^{l} = \sum_{m} \sum_{ij}^{N} h_{ij}^{l} \left|p_j^{lm}\right\rangle \left\langle p_i^{lm}\right| \tag{2.48}$$

with the projector functions defined by [67]:

$$\langle \mathbf{r} | p_i^{lm} \rangle = N_i^l Y^{lm}(\hat{\mathbf{r}}) r^{l+2i-2} \exp\left(-\frac{r^2}{2 r_c^2}\right) \tag{2.49}$$

In these expressions, $Y^{lm}(\hat{\mathbf{r}})$ are the spherical harmonics, N_i^l are normalization constants, and $h_{l,ij}$ are fitting coefficients [66, 67].

2.7.7 Auxiliary Density Matrix Method

When calculating the exchange-correlation energy in hybrid functionals, many integrals of the form

$$E_{\mathrm{X}}^{\mathrm{HF}}[P] = \sum_{ijkl} P_{ij} P_{kl} \int \int \psi_i^*(\mathbf{r}) \psi_j^*(\mathbf{r}') g(|\mathbf{r} - \mathbf{r}'|) \psi_k(\mathbf{r}') \psi_l(\mathbf{r}) \, \mathrm{d}^3 r \, \mathrm{d}^3 r' \tag{2.50}$$

must be evaluated. Here, $\underline{\mathbf{P}}$ is the density matrix, as introduced in the GPW method in Sec. 2.7.5. Given the coefficients $\mathbf{C}$ of the occupied orbitals in the chosen basis set, the density matrix can be expressed as:

$$\underline{\mathbf{P}} = \mathbf{C}\mathbf{C}^T \tag{2.51}$$

The Hartree energy involves a similar integral, which can be simplified in reciprocal space. However, this simplification does not apply to the exchange energy due to the index structure of the integrand.

Since the exchange integral contains four indices, the computational complexity scales as $\mathcal{O}(N^4)$, where N is the number of basis functions. To improve efficiency, screening techniques are used to omit contributions where $P_{ij}P_{kl}$ is negligible, introducing only minor errors in the total energy. Another effective strategy is the auxiliary density matrix method (ADMM), which approximates these integrals using a reduced basis set for the Hartree-Fock exchange (HFX) calculations. The wave functions $\psi_i(\mathbf{r})$ are approximated using a smaller auxiliary basis $\{\hat{\varphi}_\mu(\mathbf{r})\}$ [68]:

$$\hat{\psi}_i(\mathbf{r}) = \sum_\mu \hat{C}_{i,\mu} \hat{\varphi}_\mu(\mathbf{r}) \approx \psi_i(\mathbf{r}) \tag{2.52}$$

The coefficients $\hat{C}_{i,\mu}$ are obtained by minimizing the squared difference between the true and approximate wave functions. From these, the auxiliary density matrix $\hat{\underline{\mathbf{P}}}$, which is significantly smaller than the full matrix $\underline{\mathbf{P}}$, can be computed through a linear transformation of the original coefficients. The total exchange energy is then approximated as the sum of the exchange energy computed with the auxiliary density matrix, plus a correction term derived from the difference in GGA exchange energies between the full and reduced basis sets [68]:

$$E_{\mathrm{X}}^{\mathrm{HF}}[\underline{\mathbf{P}}] \approx E_{\mathrm{X}}^{\mathrm{HF}}[\hat{\underline{\mathbf{P}}}] + E_{\mathrm{X}}^{\mathrm{GGA}}[\underline{\mathbf{P}}] - E_{\mathrm{X}}^{\mathrm{GGA}}[\hat{\underline{\mathbf{P}}}] \tag{2.53}$$

2.7.8 Theory to Practice: CP2K

Developing software capable of performing DFT calculations for systems of relevant size is a significant challenge, not only due to the theoretical complexity but also because of the high-performance computing requirements. Several software packages are available for DFT simulations, including Quantum Espresso, VASP, ABINIT, and CP2K. These codes differ in many aspects, such as the choice of basis sets, intended applications, licensing models, and computational performance.

CP2K is a versatile program designed for a wide range of applications in computational chemistry and physics. It supports various DFT methods and is well-suited for large-scale simulations. The software can employ both GPW and GAPW basis sets, supports a broad selection of functionals and pseudopotentials and includes performance optimizations such as ADMM for hybrid functional calculations. Due to its flexibility and efficiency, CP2K is used in this thesis to compute the properties of the investigated materials. Its performance for large systems is particularly advantageous for the defect calculations presented in later chapters.

CHAPTER 3

MATERIAL PROPERTIES FROM DFT CALCULATIONS

For a basic screening of the properties of fluoride insulators, two key quantities are of interest: the band gap and the permittivity. This section introduces these properties, along with crystal structure and crystal defects, and explains how they can be calculated using DFT. Defects in insulators are of particular relevance, as they can lead to charge trapping and diffusion of defect species, which in turn may cause reliability issues in electronic devices, as presented in the introduction. The theoretical methods used to determine these material properties from DFT results are described in the following sections.

3.1 Crystal Structure

A crystalline material is characterized by its long-range order, meaning the atoms are arranged in a periodic structure. To describe a crystal structure, one must define both the unit cell and the atomic basis [8].

Unit Cell and Basis of a Crystal

The unit cell is specified by the lattice vectors $\mathbf{a}, \mathbf{b}, \mathbf{c}$, which, when repeated in space, tile the entire crystal with identical unit cells. Alternatively, one can view this periodicity as translational invariance: shifting the crystal by any integer linear combination of the lattice vectors leaves the structure unchanged [8].

$$\mathbf{R} = n_1\mathbf{a} + n_2\mathbf{b} + n_3\mathbf{c} \tag{3.1}$$

The set of all vectors $\mathbf{R}$ defines the Bravais lattice of the crystal. To fully describe the crystal structure, the atomic basis must also be specified. This is the set of atoms associated with a single unit cell, which is replicated at each lattice point to build the entire crystal.

These unit cells are not unique - different unit cells can be chosen to describe the same crystal. The *primitive unit cell* is the smallest possible repeating unit that fully captures the crystal's periodicity. However, sometimes a larger *conventional unit cell* is used instead [8]. The conventional cell is often preferred

for visualization, as it typically uses more intuitive lattice vectors and provides a clearer understanding of the crystal symmetry. For example, in the cubic CaF_2 crystal shown in Fig. 3.1, the primitive unit cell has non-orthogonal lattice vectors forming a 60° angle, while the conventional unit cell uses orthogonal vectors and contains 4 Ca and 8 F atoms.

3.1.1 Symmetry

Symmetry plays an important role in the calculations conducted in this thesis, as it can significantly reduce computational effort. This is particularly relevant for phonon structure calculations, as discussed in Sec. 3.3.1, and for restricting the number of possible diffusion pathways, as outlined in Sec. 5.3.1 [69].

In addition to computational advantages, symmetry also influences the physical properties of a material. It constrains the form of material tensors, such as the permittivity tensor, which can be used to assess the plausibility of the calculated results. For instance, a crystal with cubic symmetry must have a permittivity tensor that is a scalar multiple of the identity matrix. In other words, the material must be isotropic in its dielectric response [70].

Lattice Systems

Depending on the lattice vectors of the crystal, one of seven distinct lattice systems can be used to describe its symmetry [71]. Each system is characterized by the lengths of the lattice vectors a, b, c and the angles α, β, γ between them. These assignments are not unique and can be permuted without changing the underlying symmetry.

- **Triclinic** $a \neq b \neq c$
  $\alpha \neq \beta \neq \gamma \neq 90°$
- **Monoclinic** $a \neq b \neq c$
  $\alpha = \gamma = 90°, \beta \neq 90°$
- **Orthorhombic** $a \neq b \neq c$
  $\alpha = \beta = \gamma = 90°$
- **Tetragonal** $a = b \neq c$
  $\alpha = \beta = \gamma = 90°$
- **Rhombohedral** $a = b = c$
  $\alpha = \beta = \gamma \neq 90°$
- **Hexagonal** $a = b \neq c$
  $\alpha = \beta = 90°, \gamma = 120°$
- **Cubic** $a = b = c$
  $\alpha = \beta = \gamma = 90°$

Bravais Lattices

The seven crystal systems can be further divided into 14 unique Bravais lattices. These are classified based on the symmetry of the lattice system, as described above, and by the positions of lattice points within the unit cell [72].

- **Primitive (P)**: Lattice points are located only at the corners of the unit cell.
- **Base-Centered (A, B, C)**: Lattice points are at the corners and at the center of one pair of opposite faces.
- **Body-Centered (I)**: Lattice points are at the corners and in the center of the unit cell.
- **Face-Centered (F)**: Lattice points are at the corners and at the center of all faces of the unit cell.

Not all combinations of lattice system and positions are distinct and accounting for these equivalences gives a total number of 14 Bravais lattices [8].

Space Groups

A crystal's symmetry can also be described in greater detail using its point group and, more comprehensively, its space group. The space group includes all symmetry operations that leave the crystal unchanged [8]. These symmetry operations include those from the point group: rotations, reflections, inversions, and improper rotations, as well as additional symmetries specific to the crystal lattice, such as lattice translations, screw axes, and glide planes [8]. In total, there are exactly 230 unique space groups that can be used to classify crystal symmetries [73].

Several notation systems exist for enumerating these space groups. In this thesis, the Hermann-Mauguin notation, also known as international notation[1], is used. The Hermann-Mauguin name for a space group is constructed from the following components [74, 75]:

1. The Bravais lattice type (e.g., P, I, F, C, R).
2. The point group:
   (a) Rotation axes, denoted by n, where $360^\circ/n$ is the rotation angle.
   (b) Inversion centers, denoted by $\bar{1}$.

[1] This notation has been adopted as standard in the International Tables for Crystallography.

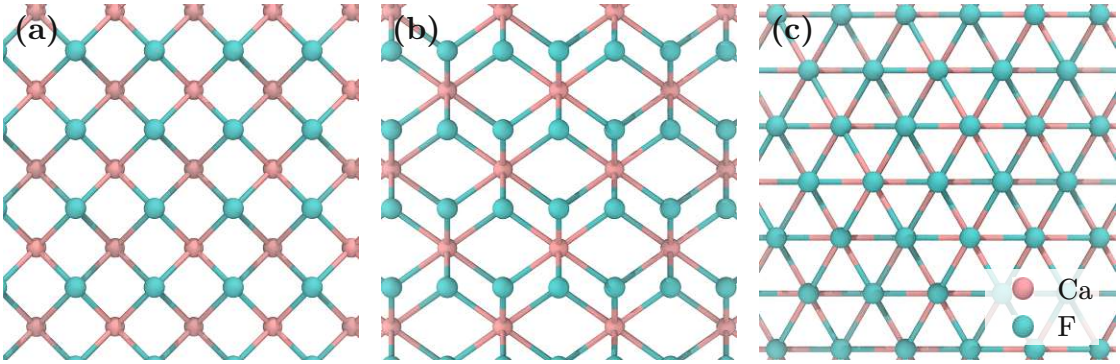

Figure 3.1: Ball and stick representation of a CaF_2 crystal, viewed along **(a)** a crystal axis, **(b)** a face diagonal, and **(c)** a body diagonal. The 4-, 2-, and 3-fold rotation axes are apparent in these representations. Cyan spheres represent F atoms, and pink spheres represent Ca atoms.

   (c) Rotoinversions, denoted by $\bar{n}$, combining $360°/n$ rotation followed by inversion.

   (d) Mirror planes, denoted by m.

   (e) Rotation-reflections, denoted by n/m, where the mirror plane is perpendicular to the rotation axis.

3. Screw axes, denoted by n_l, where $360°/n$ is the rotation angle and l is the fractional translation along the axis.

4. Glide planes, denoted by a letter indicating the direction of the glide (e.g., along lattice vectors or diagonals).

As an example, the CaF_2 crystal has the space group $F\,4/m\,\bar{3}\,2/m$, or in short notation $Fm\bar{3}m$. It is a face-centered cubic crystal, with four-fold rotation axes that have a perpendicular mirror plane (along the axes), three-fold rotoinversions (along the volume diagonals), and finally twofold rotation axes with a perpendicular mirror plane (along the face diagonals). The symmetry axes are visualized in Fig. 3.1, in which the crystal is viewed along the three different symmetry axes.

Wyckoff Positions

Within a unit cell, the positions of atomic nuclei can be classified using Wyckoff positions. When the symmetry operations of a space group are applied to a given atomic site, the atom may be mapped to one or more symmetry-equivalent

sites within the unit cell. Positions that are mapped among each other under the same set of symmetry operations are grouped together. More precisely, all points that share the same (conjugate) site symmetry group belong to the same Wyckoff position [76]. Each Wyckoff position is denoted by a multiplicity (the number of equivalent positions per unit cell) and a letter.

The complete listing of Wyckoff positions, along with their multiplicities and symmetry characteristics, is tabulated for each space group in the International Tables for Crystallography [77].

3.2 Electronic Band Gap

The electronic band gap is a key property of non-conducting materials. It represents the minimum energy difference in the forbidden region between the valence and conduction bands [8]. A large band gap characterizes an insulator, indicating that electrons are tightly bound to atoms and require significant energy to be excited. For semiconductors, the band gap is also crucial, as it directly influences the electrical properties of MOS devices. However, semiconductor band gaps are typically smaller than those of insulators. It is additionally important to distinguish between direct and indirect band gaps in semiconductors. This distinction is based on the positions of the conduction band minimum and valence band maximum in the Brillouin zone. In a direct band gap, both extrema occur at the same momentum, allowing optical transitions without the involvement of phonons. This property is essential for optoelectronic applications, as indirect semiconductors require momentum transfer for such transitions, making them less probable [8].

To estimate the band gap using DFT, the highest occupied molecular orbital (HOMO)-lowest unoccupied molecular orbital (LUMO) gap of the Kohn-Sham eigenenergies can be used. These eigenvalues are obtained from solving the Kohn-Sham equations within the self-consistent field (SCF) cycle. It is important to note that the Kohn-Sham eigenvalues and eigenfunctions do not have direct physical meaning, as they result from an auxiliary system of non-interacting electrons, as discussed in Sec. 2.7. Even the true (unknown) exchange-correlation functional does not yield the correct band gap using the HOMO-LUMO gap, due to a discontinuity in the exchange-correlation potential at integer particle numbers [46, 78].

For finite systems, the relationship between eigenvalues and excitation energies has been studied by Savin *et al.* [79], who investigated the physical meaning of the HOMO - LUMO gap obtained from DFT calculations. They found it to be a good approximation of the fundamental gap.

Perdew *et al.* found that for periodic systems and generalized Kohn-Sham methods fulfilling certain conditions, such as the hybrid functionals employed in this thesis, the HOMO - LUMO gap represents the fundamental gap of the chosen functional [80]. Nevertheless, these calculated band gaps still suffer from the discontinuity described above. Despite this limitation, hybrid potential HOMO-LUMO gaps, as discussed in 2.7.4, provide decent approximations of experimental band gaps [50] and offer a useful basis for comparing materials calculated with the same functional.

3.3 Harmonic Crystal

The separate treatment of nuclei and electrons is justified in the Born - Oppenheimer approximation, as discussed in Sec. 2.3. However, at finite temperatures, the nuclei are not fixed at lattice points but instead vibrate around their equilibrium positions. These vibrations give rise to several important physical phenomena in solids. Fundamental properties such as specific heat, thermal expansion, electronic relaxation time, and the ionic contribution to permittivity, as well as more complex phenomena like superconductivity and inelastic photon scattering, require a non-static lattice to explain them [8].

To obtain a simple description, only small displacements from equilibrium positions are considered. In this regime, the potential experienced by the nuclei can be approximated as that of a harmonic oscillator. Under this harmonic approximation, vibrational modes can be described by introducing phonons. While this model is effective for many properties, it cannot explain all behaviors of solids. For instance, thermal expansion and specific heat at high temperatures are not adequately described within the harmonic approximation [8].

3.3.1 Phonons

The potential $V(\mathbf{r}_{1,1}, \dots, \mathbf{r}_{k,l}, \dots)$ of the nuclei, which includes both their interaction with the electrons and the Coulomb repulsion among themselves, is defined by the atomic coordinates of the crystal. Here, the index k labels ions within a unit cell and l labels the unit cells themselves.

To study lattice vibrations within the harmonic approximation, only deviations from the equilibrium positions are considered. Displacement vectors $\mathbf{u}_{k,l} = \mathbf{r}_{k,l} - \mathbf{r}^0_{k,l}$ are introduced, representing the deviation of each ion from its equilibrium position.

Expanding the potential in a Taylor series around the equilibrium position, the first-order term vanishes and only the second-order term remains [81]:

$$V_{\text{harm}} = V_0 + \frac{1}{2}\sum_{kl}\sum_{k'l'} \mathbf{u}_{k,l}^{\top}\underline{\mathbf{\Phi}}_{k,l,k',l'}\mathbf{u}_{k',l'} + \ldots \tag{3.2}$$

Higher-order terms are neglected as the approximation is limited to small displacements.

The matrices $\underline{\mathbf{\Phi}}_{k,l,k',l'}$ are the force constant matrices and describe the interaction between atom k in unit cell l and atom k' in unit cell l'. Their components are defined as [81]:

$$\Phi^{\mu,\nu}_{k,l,k',l'} = \frac{\partial^2 V}{\partial \mathbf{u}^{\mu}_{k,l}\partial \mathbf{u}^{\nu}_{k',l'}}\bigg|_{\mathbf{u}=0} = -\frac{\partial \mathbf{F}^{\nu}_{k',l'}}{\partial \mathbf{u}^{\mu}_{k,l}}\bigg|_{\mathbf{u}=0} \tag{3.3}$$

The Hamiltonian of the ionic system is then given by:

$$H = \sum_{k,l}\frac{\mathbf{p}^2_{k,l}}{2m_k} + \frac{1}{2}\sum_{k,l}\sum_{k',l'}\mathbf{u}^{\top}_{k,l}\underline{\mathbf{\Phi}}_{k,l,k',l'}\mathbf{u}_{k',l'} \tag{3.4}$$

A solution to the equation of motion can be found by using the following ansatz [81]:

$$\mathbf{u}_{k,l}(\mathbf{q},\lambda) = \frac{1}{\sqrt{Nm_k}}\mathbf{U}_k(\mathbf{q},\lambda)\exp(i(\mathbf{q}\cdot\mathbf{R}_l \pm \omega_{\mathbf{q},\lambda}t)) \tag{3.5}$$

Here, $\mathbf{q}$ is the phonon wave vector and λ denotes the phonon mode. $\mathbf{R}_l$ is the lattice vector to reach unit cell l. Inserting this ansatz into the equations of motion and simplifying the resulting expressions leads to the eigenvalue equation [81]:

$$\omega^2_{\lambda}(\mathbf{q})\mathbf{U}_{k,\lambda}(\mathbf{q}) = \sum_{k'}\sqrt{\frac{1}{m_k m_{k'}}}\underline{\mathbf{C}}_{k,k'}(\mathbf{q})\mathbf{U}_{k',\lambda}(\mathbf{q}) \tag{3.6}$$

The dynamical matrix[2] is defined as [81]:

$$\underline{\mathbf{D}}_{k,k'}(\mathbf{q}) = \sqrt{\frac{1}{m_k m_{k'}}}\underline{\mathbf{C}}_{k,k'}(\mathbf{q}) = \sum_{l'}\underline{\mathbf{\Phi}}_{k,l,k',l'}\exp(i\mathbf{q}\cdot(\mathbf{R}_{l'}-\mathbf{R}_l)) \tag{3.7}$$

Due to translational symmetry, the matrix is independent of the index l. The polarization vector $\mathbf{U}_{k,\lambda}(\mathbf{q})$ describes the direction and magnitude of atomic displacement for each phonon mode. The dynamical matrix $\underline{\mathbf{D}}_{k,k'}$ has dimensions $3N \times 3N$, where N is the number of atoms per unit cell, resulting in $3N$ phonon modes in total. These modes are classified as either acoustic or optical. Acoustic modes exhibit linear dispersion for small wave vectors [81].

[2] This section uses the D-type definition of the dynamical matrix [69].

Calculating Phonons with DFT

To calculate the phonon modes, the force constant matrix must be obtained. While forces on atoms can be computed using the Hellmann-Feynman theorem [82, 83] with a single-point calculation in the framework of DFT, this approach is not sufficient for calculating the force constant matrix, which involves derivatives of the forces with respect to atomic displacements. To compute these second derivatives, either density functional perturbation theory or the so-called "frozen phonon" method can be employed [84]. The latter, which approximates the required derivatives using finite differences in a supercell, is used in this thesis. In the frozen phonon approach, the unit cell is replicated multiple times to form a supercell, and selected atoms are displaced slightly from their equilibrium positions. The number of replications determines which $\mathbf{q}$-points in the Brillouin zone are sampled. The magnitude of the displacements affects the numerical accuracy of the resulting force constant matrices. Forces are then calculated for each displaced configuration. In principle, at least $3N$ different displacements are needed to construct the full matrix, where N is the number of atoms in the unit cell. However, symmetry considerations can greatly reduce the number of necessary calculations [69].

As with many numerical approaches, there is a trade-off between computational effort and accuracy, particularly in choosing the size of the displacement and the extent of the supercell replication.

Phonopy Software Within this thesis, the PHONOPY software was used to calculate the phonon properties of the materials. Using the SPGLIB library, it can automatically determine the symmetry of a structure [85] and create a minimal number of displacements to calculate the force constant matrix. It only needs to consider one nucleus at each Wyckoff position, and the symmetry operations of the space group can be further used to reduce the number of displacements needed.

3.4 Permittivity

Permittivity is a material property that quantifies the polarization induced within the material when subjected to an external electric field. When an external electric field is applied to a crystal, both the nuclei and the electrons contribute to the polarization field since they are charged particles.

Nuclei are much heavier and thus are much slower to respond to any electrical field, which is also invoked in the Born-Oppenheimer appoximation. This means that for high-frequency electric fields, like the field associated with a photon in

the optical spectrum, the nuclei are not able to respond and therefore do not contribute to the permittivity. Hence, it makes sense to define the total permittivity for low frequencies as the sum of the electronic and ionic contributions [86]:

$$\underline{\varepsilon}_r(\omega \to 0) = \underline{\varepsilon}_{\text{el}} + \underline{\varepsilon}_{\text{ion}} \tag{3.8}$$

The nomenclature in the literature can be confusing because the electronic permittivity is sometimes referred to as the "static" permittivity, indicating that the nuclei remain static. This term should not be confused with the permittivity at zero frequency, which is also called static in typical engineering applications.

The macroscopic polarization density $\mathbf{P}$ and the macroscopic electric field $\mathbf{E}$ are related by the permittivity tensor $\underline{\varepsilon}_r$ according to:

$$\mathbf{P} = \varepsilon_0(\underline{\varepsilon}_r - \mathbb{1})\mathbf{E} = \varepsilon_0\underline{\chi}\mathbf{E} \tag{3.9}$$

Here, ε_0 is the vacuum permittivity and $\underline{\chi}$ is the electric susceptibility tensor, which relates the polarization density to the electric field. The polarization density $\mathbf{P}$ for a crystal can be defined as the dipole moment $\mathbf{p}$ per unit volume Ω:

$$\mathbf{P} = \frac{\mathbf{p}}{\Omega} \tag{3.10}$$

This dipole moment can be calculated using DFT in combination with the Berry phase formalism.

3.4.1 Berry Phase Formalism

It is important to note that polarization in a periodic system is not unique and is defined only up to a quantum of polarization [87]. The same polarization state can be represented by multiple polarization vectors, each differing by an integer linear combination of polarization lattice vectors.

This does not affect physical observables, as only differences in polarization are measurable. However, it can complicate calculations, since care must be taken to correctly handle polarization jumps when moving between different polarization lattice vectors. The polarization difference between an initial state 0 and a polarized state f can be calculated as follows [87]:

$$\delta\mathbf{P} = \frac{1}{\Omega}\underbrace{\sum_i [q_i^f \mathbf{r}_i^f - q_i^0 \mathbf{r}_i^0]}_{\text{Ionic}} - \frac{2ie}{(2\pi)^3}\sum_n \int_{\text{BZ}} \langle u_{n\mathbf{k}}^f | \frac{\partial u_{n\mathbf{k}}^f}{\partial \mathbf{k}} \rangle - \langle u_{n\mathbf{k}}^0 | \frac{\partial u_{n\mathbf{k}}^0}{\partial \mathbf{k}} \rangle \, \mathrm{d}^3\mathbf{k} \tag{3.11}$$

Here, Ω is the volume of the unit cell and $u_{n\mathbf{k}}$ are the Bloch functions as defined in Eq. 2.6. The first term is the ionic contribution, and the second term is the electronic contribution.

In this thesis, CP2K is used to calculate polarization employing the Berry phase formalism.

3.4.2 Calculating the Electronic Permittivity

To compute the electronic permittivity tensor $\underline{\varepsilon}_{\text{el}}$, a small (periodic) electric field is applied along three orthogonal directions. For this calculation the unit cell and atomic coordinates are not allowed to relax, *i.e.* they remain fixed. This means that only the electron density can respond to the field, reflecting conditions at high frequencies. The electronic permittivity tensor is then calculated from the polarization differences using:

$$\varepsilon_{\text{el},\mu\nu} = \frac{1}{\varepsilon_0}\frac{\Delta P_\mu}{\Delta E_\nu} + \delta_{\mu,\nu}, \tag{3.12}$$

which directly follows from Eq. 3.9.

3.4.3 Born Effective Charges

The Born effective charge (BEC) tensor relates the amount of charge displaced to the small displacement of an ion. Equivalently, it describes the force acting on an ion when a small electric field is applied [86]. Formally, it is defined by the change in polarization caused by a displacement of an ion [86]

$$Z^*_{i,\mu\nu} = \frac{\Omega}{e}\frac{\partial P_\mu}{\partial r_{i,\nu}} = \frac{1}{e}\frac{\partial F_{i,\mu}}{\partial E_\nu} \tag{3.13}$$

where Ω is the volume of the unit cell, i indexes the ion, P_μ is the polarization density along the μ direction, and $r_{i,\nu}$ denotes the displacement of the ion in the ν direction. For any insulating material, the sum of the BECs of all atoms in the unit cell must vanish [86]:

$$\sum_i \underline{\mathbf{Z}}^*_i = \mathbf{0}. \tag{3.14}$$

3.4.4 Ionic Permittivity

The ionic permittivity arises due to polarization caused by ion displacement in an external electric field. At low frequencies, the ionic permittivity is connected to the BEC and phonon modes at the Γ point of the Brillouin zone by [86]

$$\underline{\varepsilon}_{\text{ion},\mu\nu}(\omega) = \frac{1}{\varepsilon_0\Omega}\sum_\lambda \frac{S_{\lambda,\mu\nu}}{\omega_\lambda^2 - \omega^2} \tag{3.15}$$

with the oscillator strength tensor $\underline{\mathbf{S}}_\lambda$ defined as:

$$S_{\lambda,\mu\nu} = \left(\sum_{i\mu'} Z^*_{i,\mu\mu'} U_{\lambda,i,\mu'}(\mathbf{q}=0)\right)\left(\sum_{i\nu'} Z^*_{i,\nu\nu'} U_{\lambda,i,\nu'}(\mathbf{q}=0)\right) \tag{3.16}$$

$U_{\lambda,i}$ denotes the displacement vector of the i^{th} ion in the λ phonon mode with frequency ω_λ. The eigen-displacements must be normalized according to [86]:

$$\sum_{i,\mu} m_i U^*_{\lambda,i,\mu} U_{\lambda',i,\mu} = \delta_{\lambda,\lambda'}. \tag{3.17}$$

3.5 Defects

Real crystals are never perfect, they always contain some form of defects. These defects can be categorized by their dimensionality: point defects, line defects, or plane defects. In this thesis, only point defects are investigated, with a focus on fluorine vacancies.

3.5.1 Point Defects

Point defects can be intrinsic or extrinsic. Intrinsic defects are composed of the same elements as the host crystal, whereas extrinsic defects involve foreign elements [88]. Extrinsic defects may be introduced intentionally, as dopants, or occur unintentionally as impurities. Point defects can be classified into several categories shown in Fig. 3.2:

- **Vacancy**: An atom is missing from a lattice site.
- **Self-interstitial**: A host atom occupies an interstitial site that is normally unoccupied.
- **Substitutional defect**: An atom, not residing in this site normally, replaces a host atom at a lattice site.
- **Interstitial**: A foreign atom resides in an interstitial site.
- **Frenkel defect**: A host atom is displaced from its lattice site into an interstitial site, forming a vacancy-interstitial pair.

In certain contexts, defects are desirable, such as dopands in a semiconductor, which are usually substitutional defects. For instance, when a donor atom with an additional electron in the shell is incorporated in the host lattice, the electron is easily excited into the conduction band, increasing the conductivity of the material.

In contrast, for insulators in MOS devices, such defects are generally undesirable. However, there are exceptions where defects are deliberately introduced, such as in charge trapping layers used in memory devices [89, 90].

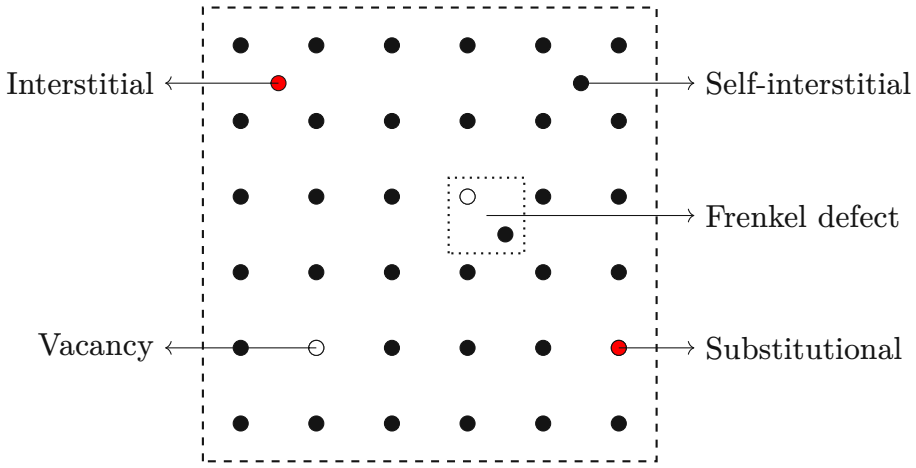

Figure 3.2: Schematic representation of different point defects in a lattice.

3.5.2 Defect Formation Energy

The formation energy of a defect quantifies the energy difference between a crystal containing the defect and the pristine crystal, accounting for the chemical potential of the atoms involved in the defect. If a defect can occupy multiple Wyckoff positions or exist in different charge states, the configuration with the lowest formation energy will be most stable under thermodynamic equilibrium at a given Fermi level [12].

The formation energy of a defect is defined by [12]:

$$E^f[X^q] = E_{\text{tot}}[X^q] - E_{\text{tot}}[\text{bulk}] - \sum_i n_i \mu_i + q E_{\text{F}} + E_{\text{corr}} \tag{3.18}$$

where $E_{\text{tot}}[X^q]$ is the total energy of the cell with a defect configuration X with charge q. E_{bulk} is the energy of the bulk material and μ_i is the chemical potential of the element i that is added ($n_i > 0$) or removed from the system in order to create the defect. E_{F} is the Fermi energy and E_{corr} is a correction term for the periodic images due to the periodic boundary conditions [91]. Several correction schemes have been proposed to account for the finite size of the supercell. A commonly used correction is the Freysoldt-Neugebauer-van de Walle (FNV) correction, which is based on the work of Freysoldt *et al.* [92].

Defects can be in different charge states, with different formation energies depending on the Fermi energy of the system. The Fermi energy is typically referenced to the valence band edge of the material, which is approximated as the HOMO of the neutral, bulk structure.

Transitions between defects in different charge states are described by non-radiative multi-phonon processes, which go beyond the scope of this thesis. A detailed description of these transitions is given in [93].

Calculation of Defect Formation Energies with DFT

The total energies of both the pristine crystal and the defect-containing structure can be trivially calculated using DFT. Before doing so, both structures must be relaxed to their equilibrium positions. This relaxation is performed using a gradient-based optimizer that searches for a local energy minimum (which might not necessarily be the global minimum). Further details on this procedure are provided in Sec. 4.1.5.

Chemical potentials are usually approximated using the total energy of the most stable compound of the element in question. For instance, the total energy of F_2 is calculated and then divided by two to estimate the chemical potential of elemental fluorine. However, this approach only provides upper or lower bounds for the chemical potential, since the actual value within the crystal depends on the specific growth conditions of the material.

Tools such as SXDEFECTALIGN [92] and CoFFEE [94] are available to compute the FNV correction term.

3.5.3 Diffusion of Defects

Some atoms in a crystal can move within the lattice over time by overcoming a characteristic transition energy barrier E_a. This process is driven by the thermal motion of atoms in the lattice, where an atom can statistically gain energy from its surroundings, which are typically treated as a heat bath. As a result, the atom moves from one site to another, leading to a macroscopic phenomenon known as diffusion.

This process is macroscopically described by Fick's laws [88]. Fick's first law, valid for an isotropic medium in this form, is given by

$$\mathbf{J} = -D\nabla n \tag{3.19}$$

where $\mathbf{J}$ is the atomic flux, D is the diffusion coefficient, and n is the concentration of the diffusing species. It describes the local flux as a response to a concentration gradient. Fick's second law, which follows from the first, governs the time evolution of the concentration:

$$\frac{\partial n}{\partial t} = D\nabla^2 n \tag{3.20}$$

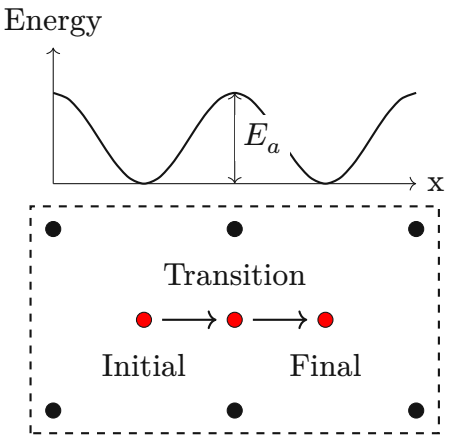

Figure 3.3: Schematic representation of a diffusion process. The interstitial moves from the initial state to the transition state and to the final state. A sketch of the energy profile of the process is shown above.

The diffusion coefficient is highly temperature-dependent and follows an Arrhenius law:

$$D = D_0 \exp\left(-\frac{E_a}{k_B T}\right) \tag{3.21}$$

where D_0 is the pre-exponential factor, E_a is the activation energy, k_B is Boltzmann's constant, and T is the temperature [88].

The temperature dependence of the diffusion coefficient can be understood by examining the microscopic mechanism of diffusion. At this scale, a particle moves randomly across a potential energy surface, transitioning from one local minimum to another. This process can be described using transition state theory, first developed by Eyring, Evans, and Polanyi [95, 96].

Transition state theory assumes that the system is initially in a thermal equilibrium and that once a transition over the energy barrier occurs, the system does not revert to the original position but instead relaxes into the new minimum. In this framework, atomic nuclei are treated as classical particles. However, this approximation can break down for light atoms, such as hydrogen, where nuclear tunneling plays a significant role [97].

The reaction rate from the initial state i to the final state j can be described by [98]

$$k_{ij} = \langle v_f \rangle P(x_t) \tag{3.22}$$

where $\langle v_f \rangle$ is the average velocity pointing towards the final state and $P(x_t)$ is the probability of finding the particle at the transition state. Assuming a thermal equilibrium, the average velocity can be described by the Boltzmann

distribution, which leads to the following result [98]:

$$\langle v_f \rangle = \sqrt{\frac{k_B T}{2\pi m}} \tag{3.23}$$

When approximating the minimum with a harmonic (parabolic) potential, the probability $P(x_t)$ is found to be

$$P(x_t) \approx \frac{1}{\sqrt{\frac{2\pi k_B T}{m\omega_0}}} e^{-\frac{E_a}{k_B T}} \tag{3.24}$$

Using this probability, the total reaction rate can be found [98]:

$$k_{ij}^{tst} = \frac{\omega_0}{2\pi} e^{-\frac{E_a}{k_B T}} \tag{3.25}$$

It has the same form as the Arrhenius equation 3.21, connecting the empirically found equation with microscopic arguments [98]. The parameter $\frac{\omega_0}{2\pi}$ is the attempt frequency, which is governed by the phonon spectrum of the material and is typically is in the order of 10^{13} Hz [99, 100].

3.5.4 Calculating Diffusion Barriers with DFT

First, the transition state must be identified. It corresponds to a first-order saddle point on the potential energy surface along the path between the initial and final states. Finding this point is not trivial, as the potential energy surface is high-dimensional and expensive to evaluate due to the already high computational cost of single-point energy calculations.

Optimization techniques such as the nudged elastic band (NEB) method [101] and variations like the climbing image nudged elastic band (CI-NEB) method [102], are used to determine both the transition state and the reaction path. Alternatively, the transition state can be found via local optimization methods like the Dimer method [103], though in practice, this approach can present certain limitations which will be discussed in more detail below.

The attempt frequency, which can be determined from the vibrational modes of the defect in the lattice, is not considered in this thesis. The activation energy is sufficient to provide a comparison of the relative diffusivity between different fluorides studied in this work.

Nudged Elastic Band Method

To find the minimum energy path between two states, including the transition state, the NEB method is a widely used approach. It is based on the concept of

an elastic band connecting the initial and final states, stretched over the potential energy surface. This band is modeled by a series of discrete points called "images" or "replicas," which are linked by virtual springs. The coordinates of these images are optimized to minimize the total energy of the band, while the spring forces maintain approximately equal spacing between images. Each image experiences two forces: the spring force from its neighboring images and the reverse physical force due to the potential energy surface [104]:

$$\mathbf{F}_i^{\text{total}} = \mathbf{F}_i^{\text{spring}} + \mathbf{F}_i^{\text{phy}} \tag{3.26}$$

with

$$\mathbf{F}_i^{\text{spring}} = k(\mathbf{R}_{i+1} - 2\mathbf{R}_i + \mathbf{R}_{i-1}) \qquad \mathbf{F}_i^{\text{phy}} = -\nabla V|_{\mathbf{R}_i} \tag{3.27}$$

where k is the spring constant and $\mathbf{R}_i$ is the position of the nuclei in image i. However, this original or "plain" elastic band method [104] tends to cut corners when the path crosses curved regions of the potential energy surface. Intuitively, this can be understood when imagining a real rubber band stretched over a concave surface. To mitigate this, the method adjusts the force components so that the spring force acts only along the tangent of the path, while the physical force is projected perpendicular to the path [101]. Given a local tangent $\mathbf{t}_i$ at image i, the corrected NEB force becomes:

$$\mathbf{F}_i^{\text{total NEB}} = \left[\mathbf{F}_i^{\text{phy}} - \left(\mathbf{F}_i^{\text{phy}} \cdot \mathbf{t}_i\right)\mathbf{t}_i\right] + \left(\mathbf{F}_i^{\text{spring}} \cdot \mathbf{t}_i\right)\mathbf{t}_i \tag{3.28}$$

The tangent vector $\mathbf{t}_i$ is typically approximated as:

$$\mathbf{t}_i \approx \frac{\mathbf{R}_{i+1} - \mathbf{R}_{i-1}}{|\mathbf{R}_{i+1} - \mathbf{R}_{i-1}|} \tag{3.29}$$

Projecting the forces in this way allows the spring interactions to control the image spacing while keeping each image aligned with the potential energy surface, thereby avoiding the corner-cutting issue. Despite this, the finite number of images can still result in missing the exact saddle point. To address this, the climbing image nudged elastic band (CI-NEB) method was developed [102]. In this extension, the image with the highest energy is allowed to climb along the potential surface by removing the spring forces and allowing the physical force to push it uphill. This ensures the image converges to the saddle point, representing the transition state. Figure 3.4 (left) illustrates the difference between standard NEB and the CI-NEB method.

A NEB calculation requires an initial guess for all intermediate images. A simple approach is to linearly interpolate between the atomic positions of the initial and final states. However, this can result in poor convergence. A more accurate guess, such as geodesic interpolation proposed by Zhu *et al.* [105], improves convergence. The authors showed that geodesic interpolation outperformed other schemes, and therefore it was used throughout this thesis.

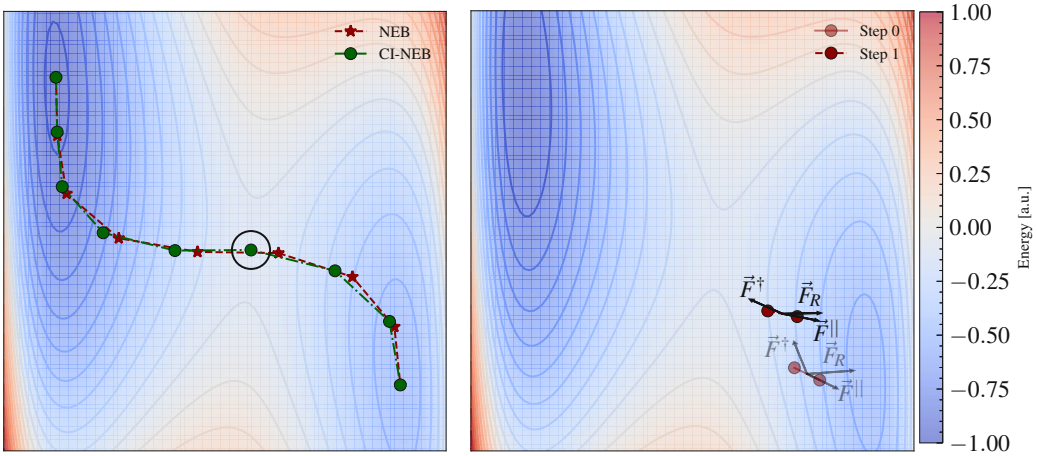

Figure 3.4: (**left**) Comparison of the reaction paths found by NEB and the climbing image NEB method. The circle marks the transition state of the example potential surface. The markers are at the location of the images of each band. (**right**) Illustration of the dimer method. The dimer is rotated to minimize the energy, and then translated according to the chosen translation method.

Dimer Method

The dimer method is a computationally less expensive technique for locating a transition state between two minima on the potential energy surface. It relies on the idea that two closely spaced, rigidly connected points (forming a ”dimer”) will have minimum energy when aligned perpendicular to the ridge of a potential energy surface.

The two points in the dimer represent configurations of the system and are used to estimate curvature. In each step of the optimization, the dimer is rotated to minimize its energy, or equivalently, to achieve vanishing torque. This rotation identifies the direction of maximum negative curvature, which typically points toward the transition state [103]. Once the optimal orientation is found, the dimer is translated in the direction of the effective force $\mathbf{F}^{\dagger}$, defined as:

$$\mathbf{F}^{\dagger} = \mathbf{F}_R - 2(\mathbf{F}_R \cdot \mathbf{t})\mathbf{t} \tag{3.30}$$

Here, $\mathbf{F}_R$ is the total force acting on the dimer, which points toward the nearest local minimum, and $\mathbf{t}$ is the direction of the dimer. By inverting the component of $\mathbf{F}_R$ that is parallel to the dimer (i.e., the maximum negative curvature direction), the resulting force $\mathbf{F}^{\dagger}$ drives the system toward the saddle point. This direction can be used for optimization via a modified molecular dynamics simulation or as the search direction in a conjugate gradient method [103]. An illustration of the dimer method is shown in Fig. 3.4 (right).

One challenge of the dimer method is that multiple saddle points may connect different minima, and it is not always trivial to verify that the correct transition state has been found. The NEB method also encounters this issue, but it offers a clearer view of the full path and energy profile connecting the images. To improve finding a relevant transition state, variants such as the κ-dimer method have been developed by Xiao *et al.* [106]. This method guides the dimer along ridges of the potential energy surface where the minimal directional curvature within an isopotential hyperplane is negative. This condition helps ensure better convergence to the true transition state [106].

CHAPTER 4
SCREENING INSULATORS

This chapter presents a first screening of thirteen fluoride compounds to identify potentially promising candidates as insulators. A consistent first-principles approach using a hybrid functional is introduced in this chapter and used to compute key properties such as band gap and permittivity of the selected materials. This step is providing a basis for selecting candidates for further study.

4.1 Methodology

As a first step, thirteen promising fluorides have been selected for investigation in this work. To ensure comparability, the same computational methodology has been consistently applied across all materials, as described in the following.

4.1.1 Basis Set, Functional, and Pseudopotentials

For all calculations conducted in this thesis, the HSE06 hybrid functional [50, 107] has been employed. This functional provides improved electronic band gap estimates compared to (semi-)local functionals, albeit with increased computational cost. The double-zeta valence polarized `DZVP-MOLOPT-SR-GTH` basis set was chosen for describing the wave functions within the GAPW method. Additionally, the auxiliary basis set `BASIS_ADMM_UZH` was used to efficiently compute the Hartree-Fock exchange. Basis sets for the lanthanides La and Ce were kindly provided by Prof. Sanliang Ling. Although these basis sets have not yet been thoroughly tested, the resulting band gaps and bond lengths obtained for the studied compounds are in reasonable agreement with experimental data. The Goedecker-Teter-Hutter-pseudopotentials [66] have been employed to describe the core electrons in all calculations.

4.1.2 Supercells and k-Point Sampling

Almost all quantities in DFT are evaluated as integrals over the Brillouin zone. This is typically achieved by sampling the Brillouin zone with a grid of k-points and approximating the integral by summing over these points. Various schemes, such as the Monkhorst-Pack grid [108], have been developed to efficiently perform

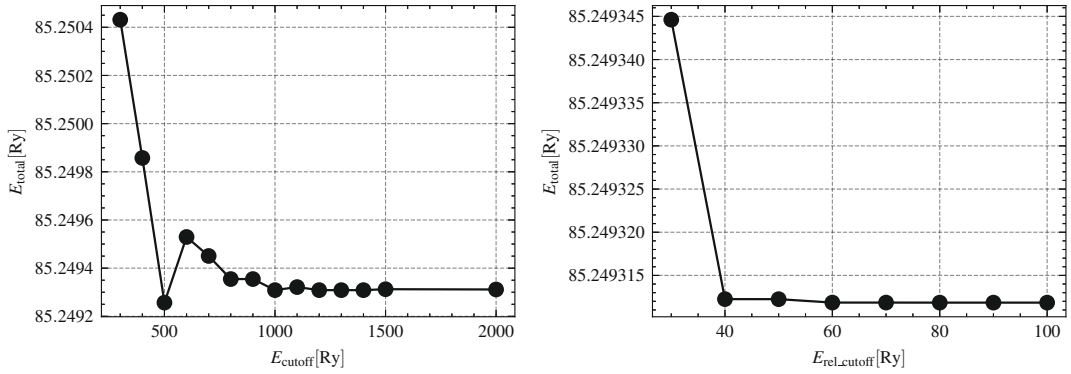

Figure 4.1: The total energy of a CaF_2 crystal as a function of the cutoff parameters. Convergence is observed around 1200 Ry for `CUTOFF` and around 60 Ry for `REL_CUTOFF`.

this sampling. Because CP2K only supports Γ-point calculations for some of the methods employed, supercells were constructed for all materials to reduce the size of the Brillouin zone. This improves the approximation of the integral, even when only the Γ point is used[1].

For all studied materials, the supercells were chosen such that each lattice vector was at least 14 Å in length.

4.1.3 Cutoffs

The cutoff energy is a critical parameter, as a lower cutoff reduces computational cost but may compromise the accuracy of results. A more detailed discussion of this relationship is provided in Sec. 2.7.5, where basis sets are introduced. To strike a balance between accuracy and efficiency, convergence tests were performed. In CP2K, two main cutoff parameters are relevant: `CUTOFF` and `REL_CUTOFF`. To determine an appropriate cutoff energy, the `CUTOFF` parameter was varied while keeping `REL_CUTOFF` fixed at a high value of 100 Ry. The cutoffs were chosen based on the convergence of the total energy. When the energy variation falls below a (chosen) threshold of 10^{-5} Ry, it is considered converged. Once the optimal `CUTOFF` is determined, a similar procedure is applied to the `REL_CUTOFF` parameter. An example convergence test for a small CaF_2 cell is shown in Fig. 4.1.

It was found that phonon force calculations require significantly higher cutoff energies to achieve convergence in a GPW calculation. To reduce the necessary

[1]It should be noted that Hartree-Fock exchange calculations with k-point sampling have become available through the RI-HFXk method [109]. However, this was not explored further in this work, since relaxed supercells are required for the subsequent defect calculations regardless.

cutoff, the GAPW method was employed. Nevertheless, this method still demands high cutoffs due to the stringent convergence criteria on forces. While other properties, such as the total energy, may already be converged, insufficient force convergence can lead to spurious imaginary phonon frequencies, which are unphysical for stable structures and indicate numerical issues. This behavior is a known limitation of atom-centric basis sets, as discussed in the review by Pallikara *et al.* [84]. For phonon spectra, plane-wave based methods often require up to twice the cutoff energy compared to total energy convergence, while atom-centric basis sets may require increases of up to a factor of ten. Convergence tests for phonon calculations in this work showed that using a `CUTOFF` of 2000 Ry and a `REL_CUTOFF` of 80 Ry yielded reliably converged results for all studied materials.

4.1.4 Thresholds and Convergence Criteria

The SCF cycle is considered converged when a predefined convergence criterion is satisfied. In CP2K, this criterion is set using the `EPS_SCF` parameter, whose interpretation depends on the chosen optimization method. Most calculations in this work were performed using the orbital transform (OT) optimization method. In this case, the convergence criterion corresponds to the maximum gradient of the total energy with respect to changes in the orbital coefficients. For all such calculations, `EPS_SCF` was set to 10^{-8} Hartree.

Additionally, the precision used in evaluating the overlap matrix elements must be controlled. Elements smaller than a defined threshold are neglected and considered to be zero. In this work, this threshold was set to 10^{-6}.

Another important parameter for both accuracy and computational efficiency when using hybrid functionals is the screening parameter `EPS_SCHWARZ`, which was set to 10^{-8}. This parameter determines whether a two-electron integral needs to be evaluated, based on an upper bound estimated using the Schwarz inequality [110].

4.1.5 Calculating Material Properties

For an initial screening of materials, the band gap and dielectric constant are of particular interest. The band gap is obtained directly from the DFT calculation and is taken as the energy difference between the HOMO and LUMO (see also the discussion in Sec. 3.2).

To determine the total dielectric permittivity, both the electronic and ionic contributions must be considered. The electronic dielectric tensor can, in principle, be derived from the polarizability tensor, which may be calculated directly using a linear response method available with a GPW basis in CP2K. However,

at the time of writing, this method is not yet available for the GAPW basis set. As a result, a finite difference approach is used to calculate the electronic permittivity. The BEC tensor and phonon modes are also computed and subsequently used to calculate the ionic contribution to the permittivity, as discussed in Chap. 3.

4.1.6 Calculation Workflow

To determine the permittivity and band gap of a material, several other calculation steps have to be first carried out as illustrated in Fig. 4.2.

Creating and Relaxing the Crystal

Crystal structures of the materials of interest were obtained using the Materials Project application programming interface (API) [111, 112], and then symmetrized using Phonopy. From the symmetrized conventional unit cell, a manually selected supercell was constructed. Typically, these supercells had lattice vectors of at least 14 Å in length, with approximately 200 atoms per cell, depending on the specific material.

The energy of each cell was minimized using the limited-memory Broyden-Fletcher-Goldfarb-Shanno (LBFGS) method [113], which optimized both atomic positions and lattice vectors while preserving crystal symmetry. Energy minimization ensures that the structure corresponds to the material's ground state and is free from external stress. In cases where the chosen convergence criteria for residual forces and pressure were not met using LBFGS alone, the cell was further relaxed using the Broyden-Fletcher-Goldfarb-Shanno (BFGS) method [114]. The optimization continued until the maximum residual force was below 10^{-5} Hartree/Bohr and the remaining pressure was less than 10^{-3} GPa. These rather strict bounds were chosen because phonon calculations are very sensitive to the geometry of the relaxed cell. Insufficient relaxation can lead to spurious imaginary phonon modes.

Once the cell was fully relaxed, several input files for subsequent calculations were prepared. These could be executed independently, allowing efficient use of available computational resources.

Phonon Calculations

Frozen phonon calculations, as introduced in Sec. 3.3.1, were prepared by displacing atoms in the supercell using Phonopy, which reduces the number of required single-point calculations by exploiting symmetry. Specifically, only one

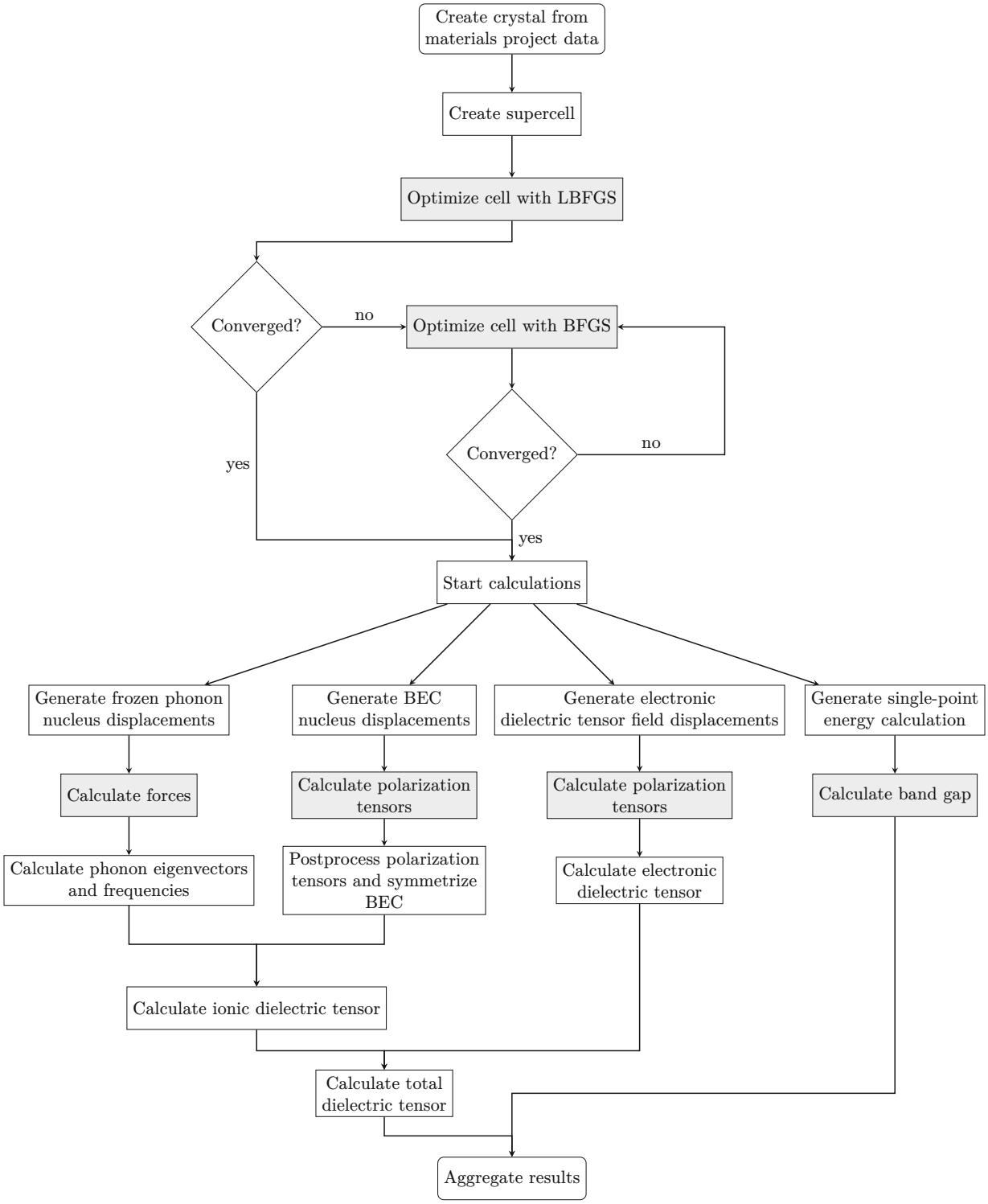

Figure 4.2: Flowchart of the calculations conducted to calculate total static permittivity and band gap. All light gray boxes correspond to calculations made with CP2K.

atom per Wyckoff position must be considered, and displacement vectors are chosen according to the crystal's symmetry. For instance, in a high-symmetry CaF_2 crystal, only on Ca atom and one F atom are displaced in a single direction, which reduces the number of required calculations to just two. When central finite differences are used, *i.e.* displacements in both positive and negative directions from the equilibrium position, four calculations are needed to account for symmetric displacements and eliminate errors from any residual forces.

In contrast, a naive approach that does not make use of symmetry would require up to 3[nuclei] × 3[directions](×2[±disp.]) = 9 (18) displacements.

Furthermore, symmetry considerations were used to reduce numerical noise in the calculation. PHONOPY ensures that symmetry constraints for force constants as well as the acoustic sum rule is satisfied.

In all calculations presented in this thesis, the displacement distance was set to 0.01 Å in both positive and negative directions. The resulting forces were then post-processed using PHONOPY to calculate the phonon eigenvectors and frequencies at the Γ point, as well as the full phonon dispersion. The latter can be found in Appendix B.

Born Effective Charges

The atoms in the Wyckoff positions displaced in the phonon calculations were also displaced for the BEC calculations. Due to the restriction of Γ-point calculations in CP2K, supercells were employed for these computations as well. All equivalent atoms in each unit cell of the supercell were displaced simultaneously in the same direction. The displacement distance was set to 0.01 Å, consistent with the phonon calculations.

The polarization tensors, computed using the Berry phase formalism in CP2K, were post-processed to evaluate the BEC tensors as defined in Eq. 3.13. These tensors were then symmetrized to enforce the symmetry constraints dictated by the crystal structure, thereby reducing numerical noise and ensuring physically meaningful results.

Electronic Dielectric Tensor

For the same crystal structure an electric field is applied in the three x, y, and z directions. The polarization tensors were calculated with CP2K and subsequently, the electronic dielectric tensor was calculated using finite differences as discussed in Sec. 3.4.2.

Ionic Dielectric Tensor

The results from the phonon and BEC calculations were used to compute the ionic dielectric tensor. The three acoustic modes were excluded from the calculation, as they do not contribute to the dielectric tensor at the Γ point. At this point, acoustic modes correspond to rigid translations of the entire crystal, resulting in zero oscillator strength, but could introduce large numerical errors in the calculation of the dielectric tensor. In practice, these modes often exhibit small negative frequencies due to numerical inaccuracies in the phonon calculations where ideally, for stable structures, the frequencies of the acoustic modes should be exactly zero at the Γ point.

Total dielectric tensor

Finally, the electronic and ionic dielectric tensors are combined to obtain the total dielectric tensor. To estimate the effective permittivity of a polycrystalline material, the eigenvalues of the total dielectric tensor can be averaged. Upper and lower bounds for the effective permittivity are given by [112, 115]:

$$\frac{3}{1/\lambda_1 + 1/\lambda_2 + 1/\lambda_3} \leq \varepsilon_{\text{total}} \leq \frac{1}{3}(\lambda_1 + \lambda_2 + \lambda_3) \tag{4.1}$$

where λ_i are the eigenvalues of the total dielectric tensor.

Reducing the tensor to a single scalar value allows for easy comparison between different materials. This approach is additionally justified by the assumption that commonly used deposition methods produce polycrystalline materials. The complete dielectric tensors for all materials considered can be found in the appendix of this work.

4.2 Materials and Results

All materials investigated within this thesis were studied using the methodology described in Fig. 4.2. The results are shown in Fig. 4.3, where the band gap is plotted against the low-frequency permittivity of the respective fluoride.

Furthermore, experimental results are available for some materials. The range of these experimental values is displayed in the plot by the width and height of the ellipses. It can be seen that the band gap is underestimated for most materials, except for BiF_3, which is unusual for hybrid functional DFT calculations as discussed in Sec. 2.7.4. The calculated permittivities are in good agreement with experimental values for materials like CaF_2 and LaF_3, BiF_3 is an outlier with a significantly higher permittivity compared to experimental values. One of the two experimental sources for BiF_3 measured nanoparticles with spatial dimensions of

Material	Bandgap [eV]	Relative Permittivity
CaF_2	10.24 – 12.1 [116, 117]	6.798 – 6.84 [118–121]
SrF_2	9.73 – 11.25 [116, 117]	6.45 – 7.69 [120, 121]
BiF_3	3.94 – 5.1 [122, 123]	40 [124]
LaF_3	9.4 – 10.51 [125–127]	13 – 14 [128, 129]
PbF_2	5.84 [130]	26.3 [131]
CeF_4	3.95 [132]	17 [132]
YF_3	10 – 10.53 [127, 133]	14.1 [134]

Table 4.1: References for experimental data of the materials shown in Fig. 4.3

30 nm [122] which could be a reason for the deviation of experimental results compared to the theoretical results.

Four materials were selected for further examination: CaF_2, BiF_3, LaF_3, and ZrF_4. CaF_2 was selected not only because it has already been used to demonstrate a working device [19], but also because it is a well-studied material that can be used to benchmark the used methodology. ZrF_4 was chosen as a material with properties close to the average electronic property range of all studied fluorides. It is used as another benchmark material, to see if further studied properties could be beneficial for an otherwise average material. BiF_3 was chosen for its unusually high permittivity, while LaF_3 was selected for its high permittivity and high band gap, making it an ideal candidate for electronic device applications.

Different possible, but potentially unstable, crystalline phases were evaluated for all of these materials and also displayed in Fig 4.3. These structures are not expected to be stable under normal conditions, but depending on the growth parameters, those phases might still exist as thin films.

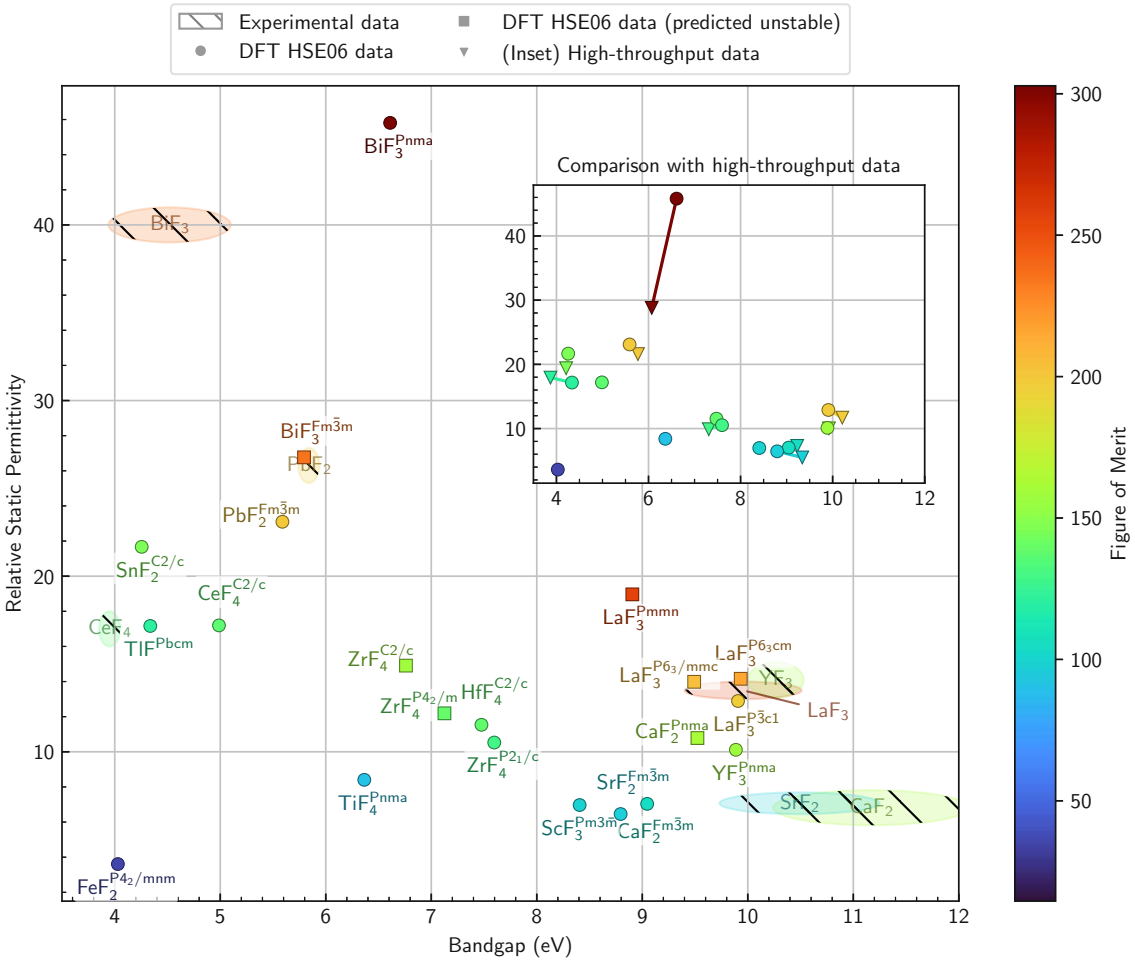

Figure 4.3: Results of the screening of selected materials. For CaF_2, BiF_3, LaF_3 and ZrF_4 predicted unstable structures were also calculated marked with squares. The figure of merit is $\varepsilon_r \cdot E_{\text{gap}}$. The space group of the structure is indicated as the exponent. The range of experimental values, as far as available from literature, is shown as ellipses. The inset compares the results of this thesis to available GGA+U DFT calculations. The references for experimental data can be found in Table 4.1. The data referenced in the inset for comparison from other DFT calculations is from high throughput calculations performed by Lee *et al.* [18]

CHAPTER 5
FLUORINE VACANCIES

Defects in a crystal can have different charge states, as discussed in Sec. 3.5 and the energy levels of these charge transitions with respect to the Fermi level can have a significant impact on the device stability when used as a gate dielectric. In scaled MOS devices, charge traps can cause bias temperature instability (BTI) [135], RTN [136], and hysteresis effects [137], which are undesirable for the device reliability [13, 138]. Furthermore, different charge states of defects within the band gap can also cause trap-assisted gate leakage currents depending on their relative position to the band edges [139] which is also discussed in the introduction Chap. 1.

Fluorides have been reported to exhibit high ionic conductivity [16], which is attributed to low energy barriers for migration of fluorine ions within the lattice. This property makes fluorides attractive candidates for use as ionic conductors in battery applications [140]. However, the high mobility of fluorine ions may negatively impact the reliability of MOS devices. Nevertheless, the migration of fluorine ions contributes to an enhanced static dielectric constant at low frequencies, as observed by Meng *et al.* [16].

In this chapter, the charge transitions at vacancy defects and fluorine vacancy migration in the fluorides picked in Chapter 4 are studied. These properties can be utilized in future studies with TCAD simulations, where the electronic properties of the material can be used to predict the device behavior [141].

5.1 Methodology

In this chapter migration barriers of fluorine vacancies in the lattice, as well as the projected density of states (PDOS) of each material with a vacancy defect are calculated. The workflow for calculating the properties of fluorine vacancy defects is illustrated in Fig. 5.1.

As a first step, a F atom is removed from the lattice at each Wyckoff position. The geometry of the resulting defect structure is then relaxed until the maximum force falls below 10^{-4} Hartree/Bohr. For each charge state of the defect, the total energy, PDOS, molecular orbitals, and electrostatic potential generated by the total electron density are computed. Subsequently, the energy correction for each charge state is determined using SXDEFECTALIGN, a tool that implements the

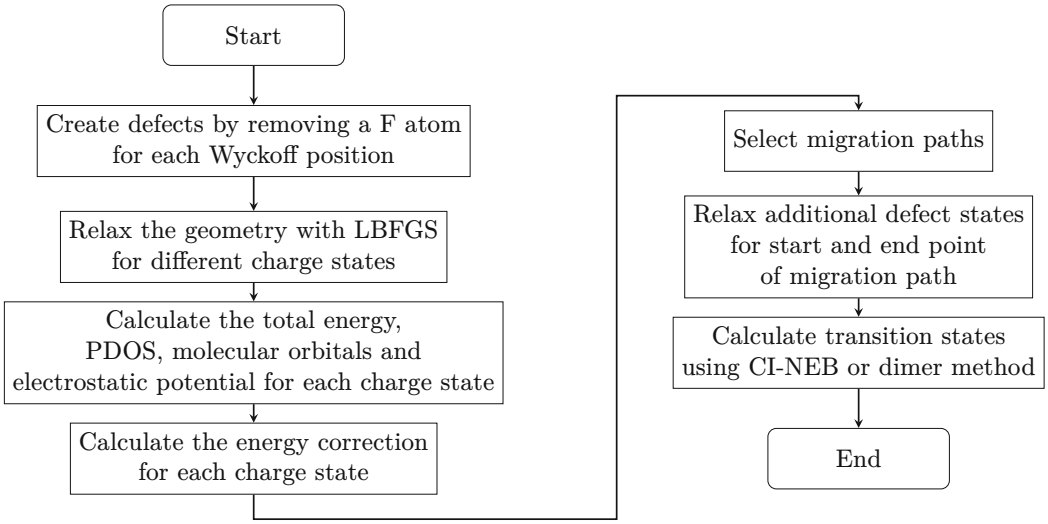

Figure 5.1: Flow chart of the methodology used to calculate the fluorine vacancy states and migration barriers.

FNV correction [92], which is essential for accurately computing defect formation energies.

Based on the results of these calculations, specific migration paths of interest are identified, and the corresponding transition barriers are computed. A more detailed discussion of this process is presented in Sec. 5.3.

5.2 Formation Energies

The formation energies of vacancy defects for all relevant Wyckoff positions in the studied materials provide insight on their thermodynamic stability. This is essential to understand the impact of these defects as charge traps as well as their most relevant charge state for further analysis of migration behavior.

5.2.1 CaF_2 - Calcium Fluoride

CaF_2 is the simplest material studied within this thesis due to its highly symmetric $Fm\bar{3}m$ cubic space group. There is only one Wyckoff position for the fluorine atom, which is the 8*c* position.

The defect formation energy as a function of the Fermi level for the fluorine vacancy in CaF_2 is shown in Fig. 5.2. As one can see, the defect is most stable for the +1 charge state for almost the entire range of Fermi levels inside the electronic band gap. This can be expected, as the fluorine atom usually binds one electron from the lattice to fill up its outer shell, which is now missing.

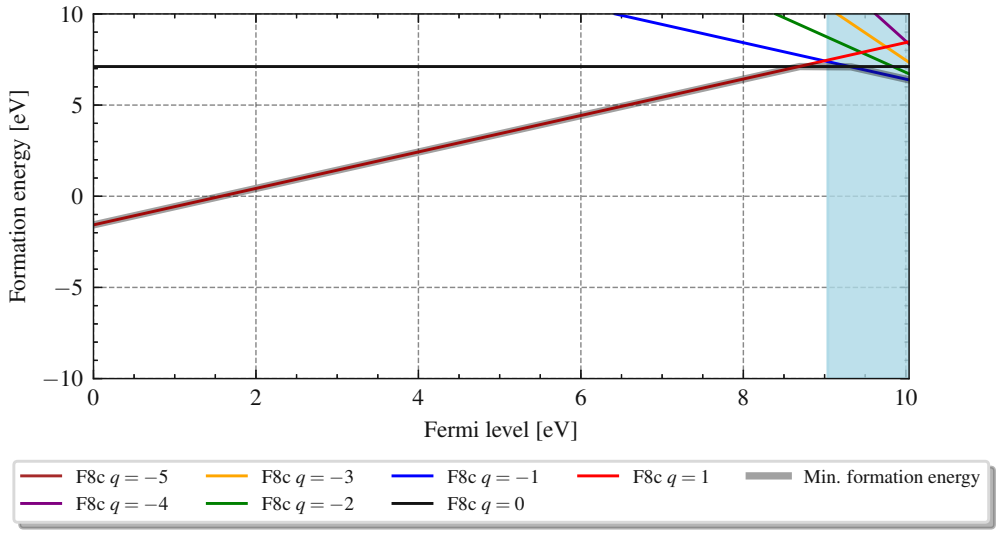

Figure 5.2: Defect formation energy for the fluorine vacancy in CaF_2 depending on the Fermi level, which is referenced to the valence band edge. The thick line shows the lowest energy at each Fermi level, and thus the most probable charge state of the defect. The light blue area indicates the conduction band.

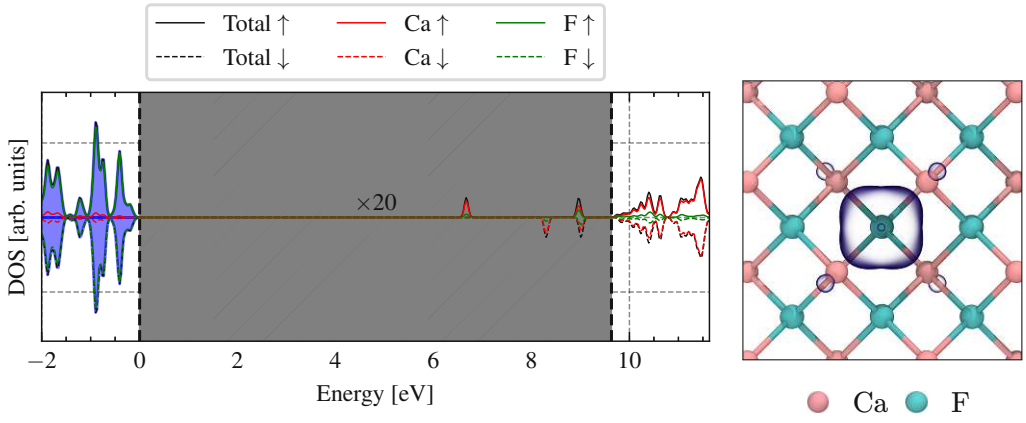

Figure 5.3: Spin polarized PDOS **(left)**, and localized orbital shape of the LUMO **(right)** for the fluorine vacancy in CaF_2. Multiple localized charge states are visible in the band gap. The band gap density (gray shaded area) is multiplied by 20 to make defect states visible. The blue area represents the filled states in the neutral state of the structure.

5.2.2 BiF_3 - Bismuth Trifluoride

BiF_3 has two Wyckoff positions for the fluorine atoms, which correspond to the $4c$ and $8d$ positions. The crystal structure is orthorhombic and belongs to the *Pnma* space group. The relaxed lattice vectors are $a = 6.87$ Å, $b = 7.26$ Å and $c = 4.44$ Å.

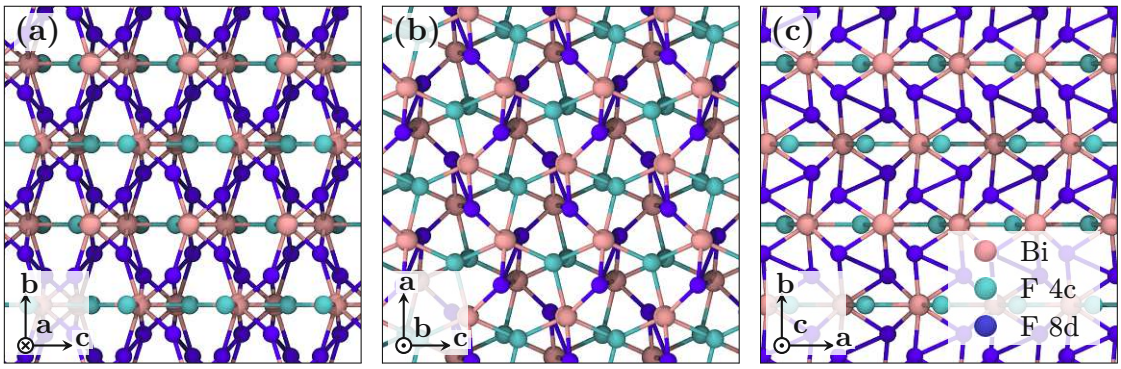

Figure 5.4: Crystal structure of BiF_3 when looking along the (a) a-axis, (b) b-axis and (c) c-axis. Bi is displayed in pink, while F $4c$ is turquoise and F $8d$ is blue.

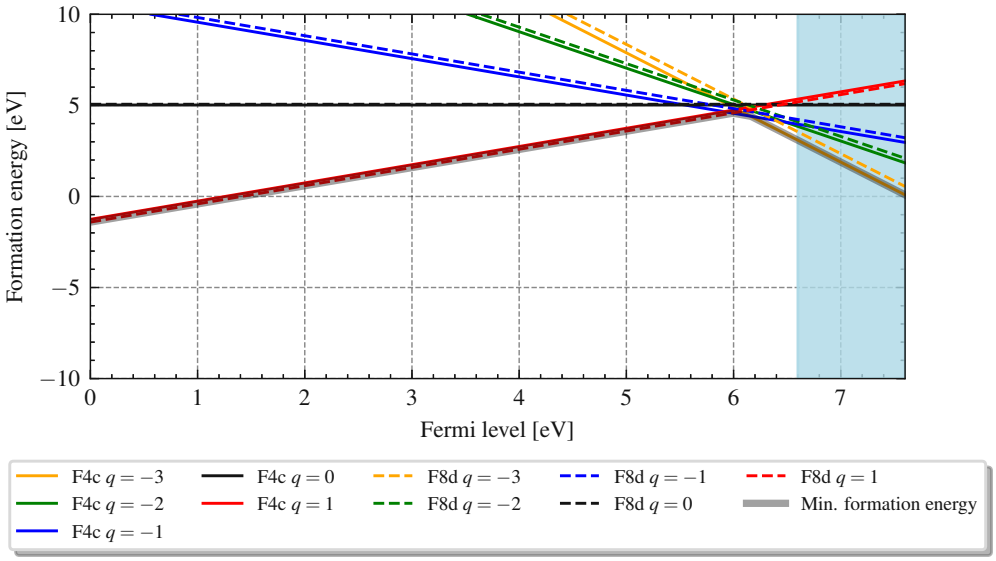

Figure 5.5: Defect formation energy for the fluorine vacancies in BiF_3 depending on the Fermi level, which is referenced to the valence band edge. The thick line shows the lowest energy at each Fermi level, and thus the most probable charge state of the defect. The light blue area indicates the conduction band.

The formation energies as a function of the Fermi level are shown in Fig. 5.5.

Charge State	Minimum Energy Position	Position	Formation Energy Difference
+1	8*d*	4*c*	150 meV
0	4*c*	8*d*	40 meV
−1	4*c*	8*d*	250 meV
−2	4*c*	8*d*	200 meV
−3	4*c*	8*d*	460 meV

Table 5.1: Formation energy difference between two possible fluorine vacancy positions in BiF_3 for different charge states. The minimum energy position is the most stable position for the given charge state.

From the two possible different vacancy positions, the vacancy at 4*c* has a higher formation energy for the +1 charge state than the 8*d* position. For the negative charge states, the vacancy at the 4*c* position is more favorable.

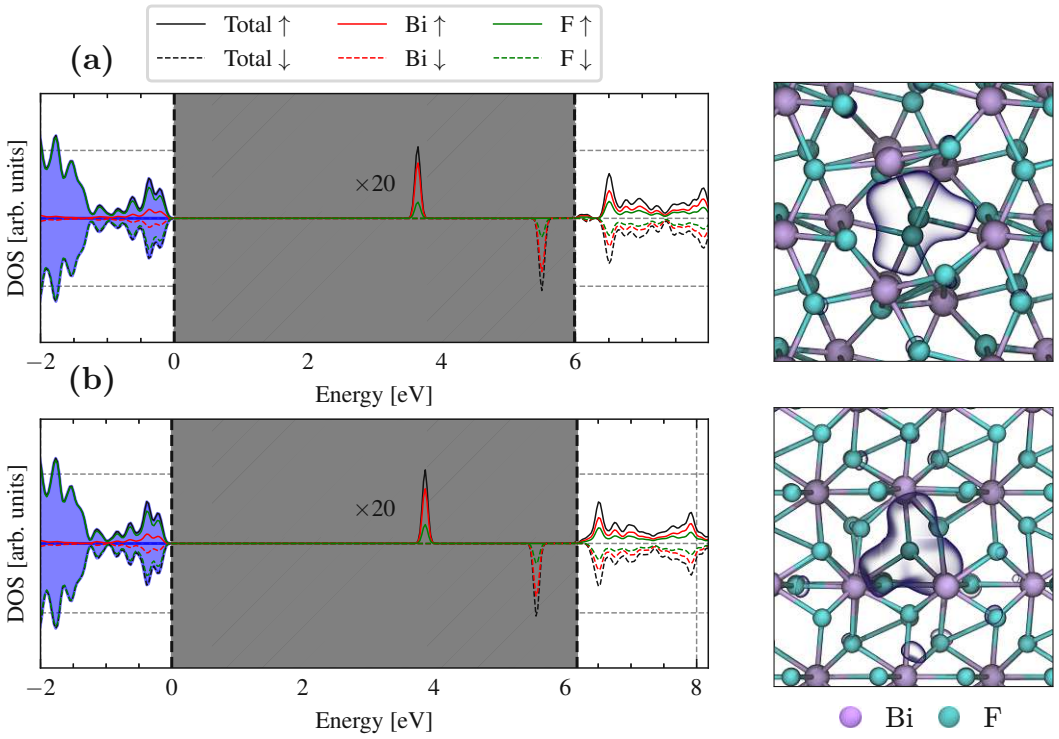

Figure 5.6: Spin polarized PDOS **(left)**, localized orbital shape of the LUMO **(right)** for the fluorine vacancy at position 4c **(a)** and 8d **(b)** in BiF_3 like in Fig. 5.3.

5.2.3 LaF_3 - Lanthanum Trifluoride

LaF_3 has three Wyckoff positions for the fluorine atom, which are the $2a$, $4d$ and $12g$ positions. The crystal structure is trigonal and belongs to the $P\bar{3}c1$ space group. The relaxed lattice vectors are $a = b = 7.20$ Å and $c = 7.366$ Å.

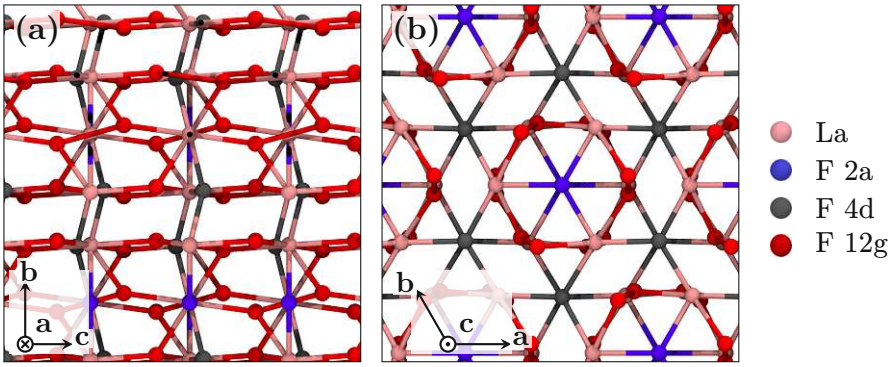

Figure 5.7: Crystal structure of LaF_3 when looking along the (a) a lattice vector, (b) c lattice vector. La is displayed in pink, while F $2a$ is blue, F $4d$ is gray and F $12g$ is red.

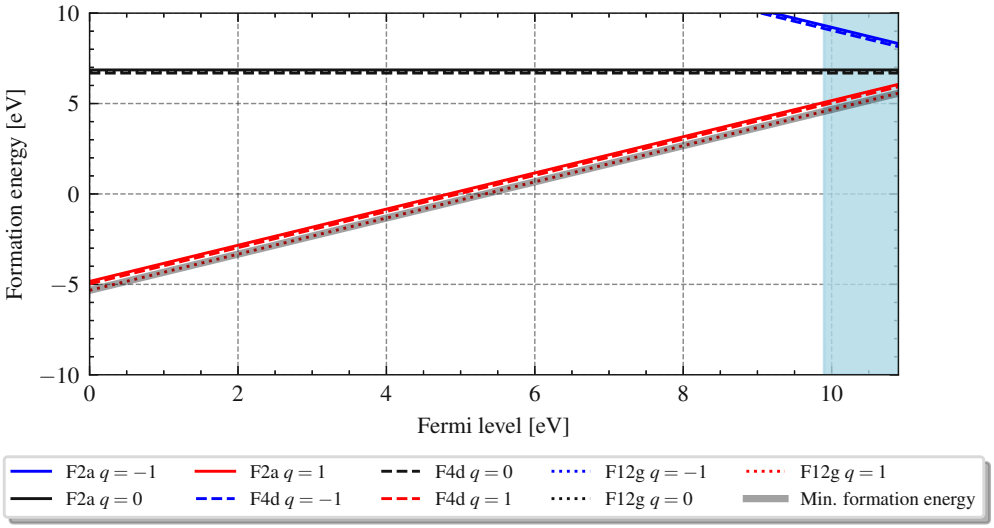

Figure 5.8: Defect formation energy for the fluorine vacancies in LaF_3 depending on the Fermi level, which is referenced to the valence band edge. The thick line shows the lowest energy at each Fermi level, and thus the most probable charge state of the defect. The light blue area indicates the conduction band.

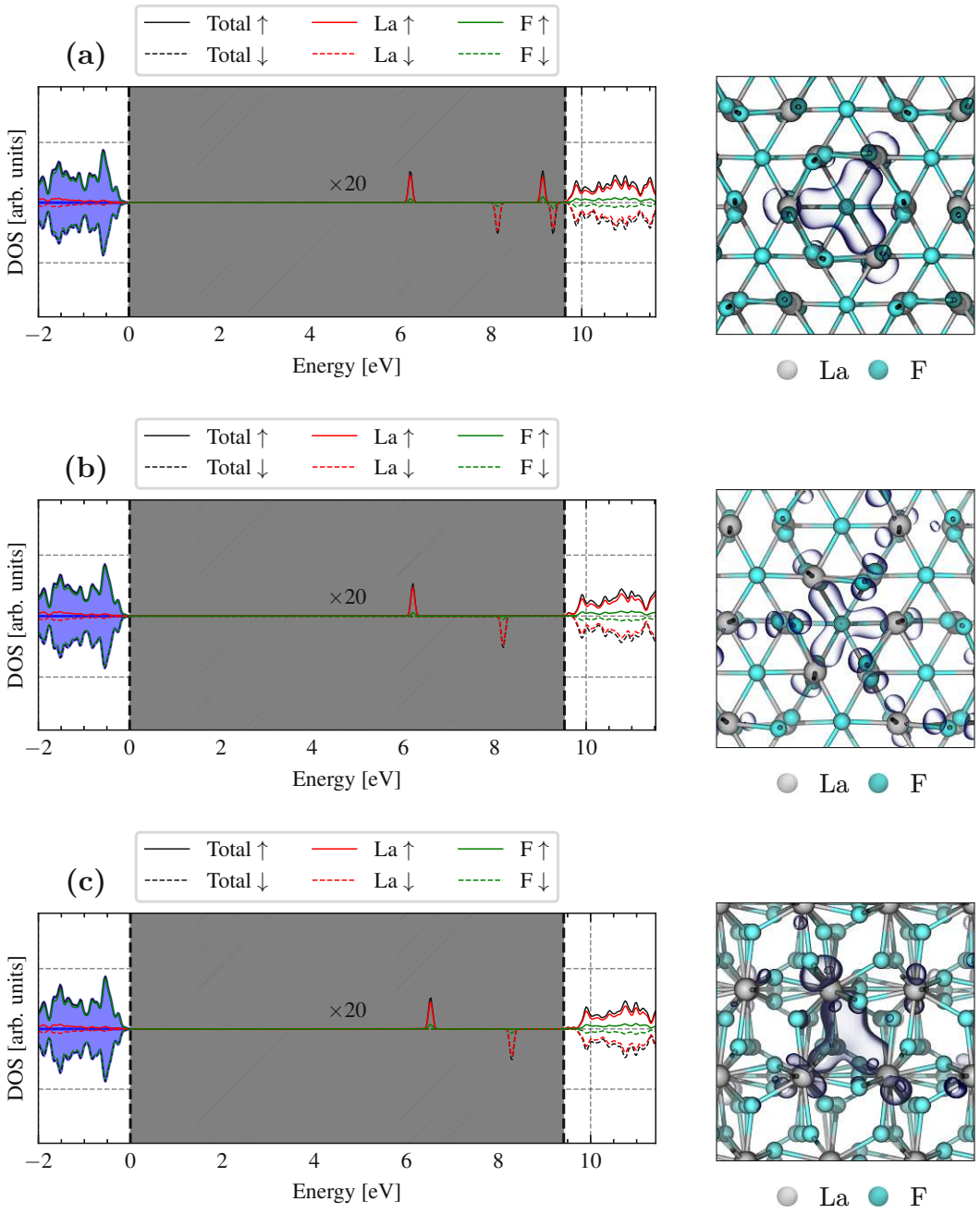

Figure 5.9: Spin polarized PDOS **(left)**, localized orbital shape of the LUMO **(right)** for the fluorine vacancy at position 2a **(a)**, 4d **(b)** and 12g **(c)** in LaF_3. Multiple localized charge states are visible in the band gap. The band gap density (gray shaded area) is multiplied by 20 to make defect states visible. The blue area represents the filled states at neutral state of the structure.

For LaF_3, the +1 charge state of the vacancy is most stable for the entire Fermi level range inside the band gap. The $12g$ position is the most favorable for the defect, as it has the lowest formation energy, with a difference of 360 meV compared to the $4d$ position. Interestingly, the shape of the defect LUMO looks similar for the $4d$ and $2a$ positions, which are similar in energy. The orbital for the $12g$ position is slightly distorted and oriented differently.

Charge State	Minimum Energy Position	Position	Formation Energy Difference
+1	$12g$	$4d$	360 meV
+1	$12g$	$2a$	490 meV
0	$4d$	$12g$	100 meV
0	$4d$	$2a$	170 meV
−1	$4d$	$12g$	110 meV
−1	$4d$	$2a$	170 meV

Table 5.2: Formation energy differences between two possible fluorine vacancy positions in LaF_3 for different charge states. The minimum energy position is the most stable position for the given charge state.

5.2.4 ZrF_4 - Zirconium Tetrafluoride

ZrF_4 has four Wyckoff positions for the fluorine atom, which are all in the equally named group 4e. To distinguish them, they are labeled as $4e_1$, $4e_2$, $4e_3$ and $4e_4$. The crystal structure is monoclinic and belongs to the $P2_1/c$ space group.

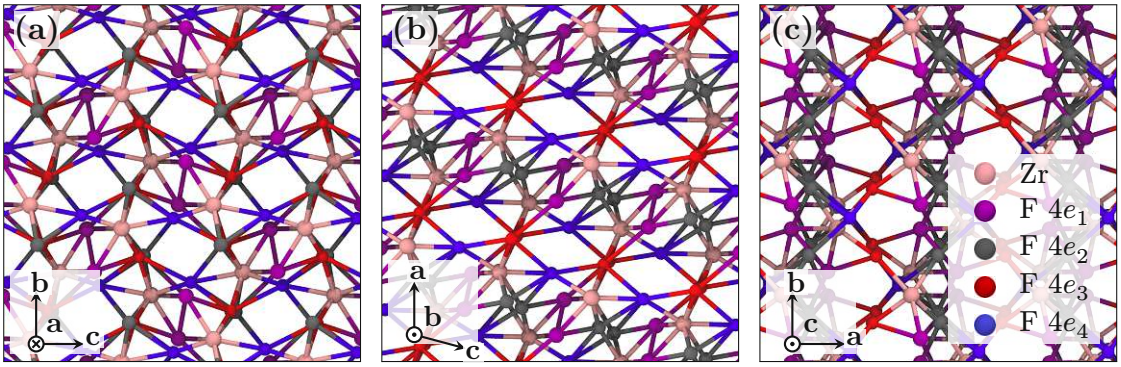

Figure 5.10: Crystal structure of ZrF_4 when looking along the (a) a-axis, (b) b-axis and (c) c-axis. Zr is displayed in pink, while the other positions of F are indicated by purple $4e_1$, gray $4e_2$, red $4e_3$ and blue $4e_4$.

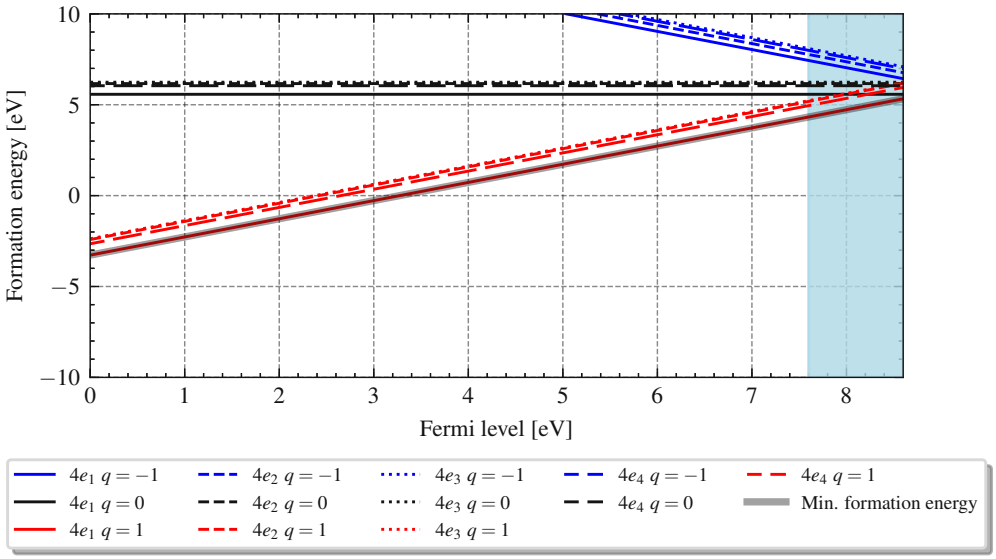

Figure 5.11: Defect formation energy for the fluorine vacancies in ZrF_4 depending on the Fermi level, which is referenced to the valence band edge. The thick line shows the lowest energy at each Fermi level, and thus the most probable charge state of the defect. The light blue area indicates the conduction band.

ZrF_4 is also simple in the sense that, across all Fermi levels in the band gap, the +1 charge state is the most favorable for every defect position. Among them, the $4e_1$ position is the most thermodynamically stable site for a vacancy. For the +1 charge state, the $4e_2$ and $4e_3$ positions are unstable in the sense that no energy barrier prevents a transition toward the $4e_1$ position. When a fluorine atom is removed from either $4e_2$ or $4e_3$, and the structure is relaxed, a neighboring fluorine from a $4e_1$ position moves to occupy the vacancy. This effectively results in a vacancy at the $4e_1$ site. The two energy levels shown in Fig. 5.11 and Fig. 5.12 were obtained by fixing the fluorine atom in the $4e_1$ position while relaxing the rest of the structure.

As also observed in LaF_3, the LUMO shape at the $4e_1$ site differs significantly from that at the other positions since it does not show the characteristic state emerging between the two Zr atoms. Instead, the orbital is localized on a single Zr atom with additional localization near neighboring F atoms. This difference in shape could be seen as a further indication to the fact that the $4e_1$ position is different from the other three positions - in this case lower in energy.

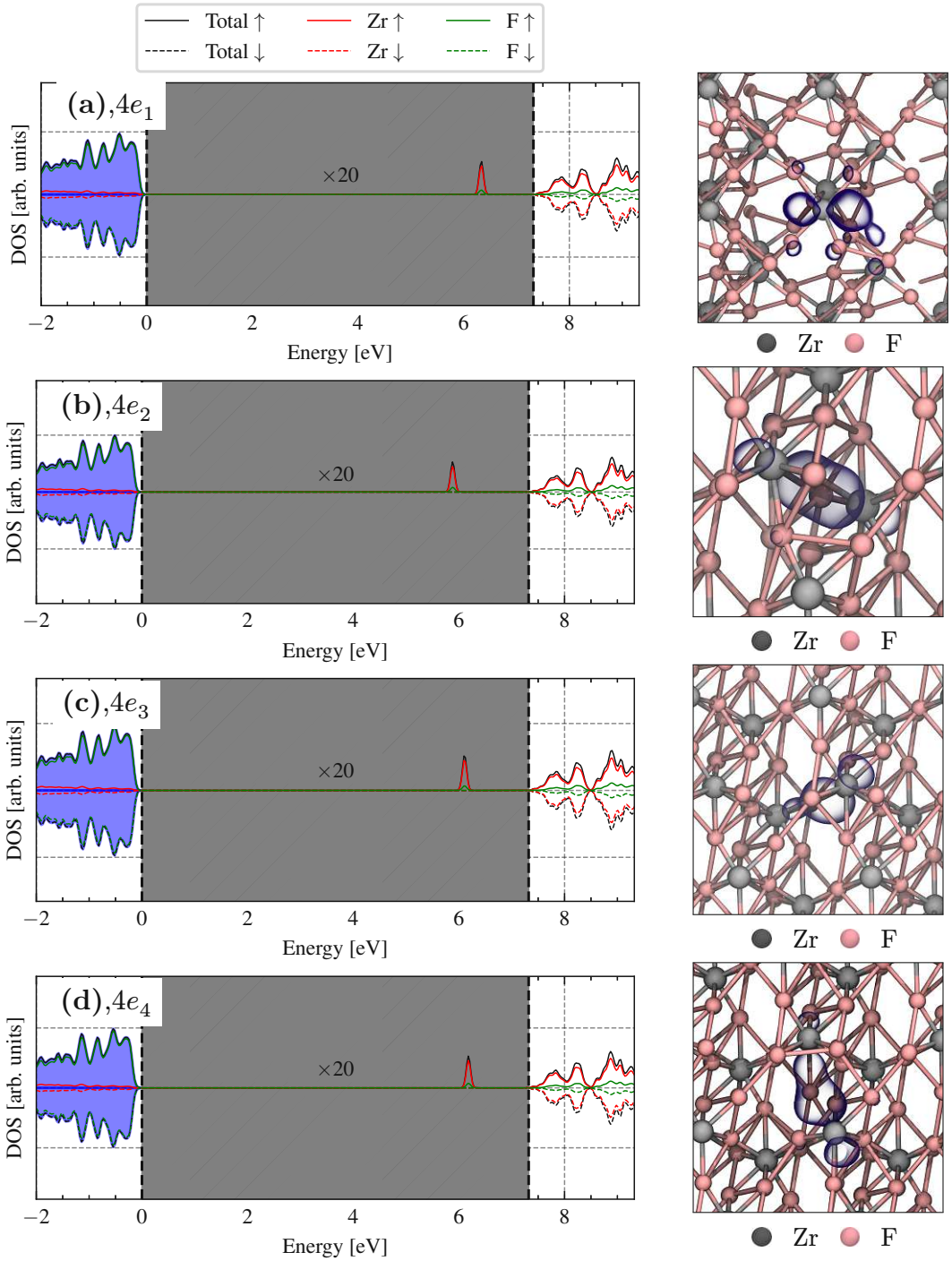

Figure 5.12: Spin polarized PDOS **(left)**, localized orbital shape of the LUMO **(right)** for the fluorine vacancy at position $4e_1$ **(a)**, $4e_2$ **(b)**, $4e_3$ **(c)**, $4e_4$ **(d)** in ZrF_4. The band gap density (gray shaded area) is multiplied by 20 to make defect states visible. The blue area represents the filled states at neutral state of the structure.

Charge State	Minimum Energy Position	Position	Formation Energy Difference
+1	$4e_1$	$4e_2$	860 meV
+1	$4e_1$	$4e_3$	900 meV
+1	$4e_1$	$4e_4$	620 meV
0	$4e_1$	$4e_2$	590 meV
0	$4e_1$	$4e_3$	660 meV
0	$4e_1$	$4e_4$	470 meV
−1	$4e_1$	$4e_2$	330 meV
−1	$4e_1$	$4e_3$	650 meV
−1	$4e_1$	$4e_4$	560 meV

Table 5.3: Formation energy differences between two possible fluorine vacancy positions in ZrF_4 for different charge states. The minimum energy position is the most stable position for the given charge state.

5.3 Transition Barriers

To analyze fluorine migration in the various fluorides via the vacancy diffusion mechanism, this section investigates the transition barriers between fluorine vacancy sites, as introduced in Sec. 5.2. These energy barriers are critical parameters that govern diffusion activation, which follows an Arrhenius-type behavior as described in Sec. 3.5.3.

While numerous diffusion paths are possible within a crystal, only the most probable transitions are considered to limit the computational cost. Since NEB calculations are particularly resource-intensive, selecting the most relevant migration paths is essential.

5.3.1 Selecting Transition Paths

For two materials, ZrF_4 and LaF_3, only the most stable charge state (+1) across all Fermi levels is considered. CaF_2 exhibits two viable charge states (0 and +1), while BiF_3 is more complex, featuring three low-energy charge states depending on the Fermi level: −3 and −1 at the 4*c* position, and +1 at the 8*d* position. Only transitions between these low-energy positions are analyzed since they are most likely to occur in the crystal. To ensure all relevant positions are accessible for any vacancy defect, allowing global diffusion, a graph-based approach is employed to identify and evaluate possible transition pathways between the vacancy sites.

Reducing Equivalent Transition Paths

The aim is to find the transition barriers that are necessary for global diffusion and find the limiting step for this diffusion process. To achieve this, barriers are analyzed starting from the shortest physical distances, continuing until a vacancy can reach every relevant position in the crystal. To identify the most relevant, non-equivalent migration paths algorithmically, the following procedure is used:

First, the distances between all atoms in the relevant positions are computed, including periodic images. An undirected graph is then constructed, where the vertices represent the possible migration sites. Edges are added iteratively, starting with the shortest distances. After each iteration, the graph is checked for connectivity, meaning that every vertex must be reachable from every other vertex. Once the graph is fully connected, the algorithm terminates and returns the set of distances and corresponding transitions identified up to that point. A pseudocode sketch of the algorithm is shown in Alg. 5.1.

From the set of identified transitions, one representative transition was selected for each distance manually, which was then used to compute the corresponding energy barrier. Additional parameters, such as the degree of the nodes in the graph or the number of connected components at each step, can also assist in the final, manual selection of migration paths. This procedure provides a systematic approach to identifying the most relevant migration pathways and helps to filter out unlikely transitions. To validate this approach, the next additional transition with a larger physical distance that is not required to ensure graph connectivity, was also evaluated. For all materials considered, this extra transition exhibited a much higher energy barrier, making it irrelevant for the diffusion process since the position can be reached via a lower-energy path.

These additional results, which are included in the following sections, support the effectiveness of the proposed methodology in identifying the most critical and energetically favorable migration paths.

Calculating Transition Barriers

From the generated transition paths, the initial and final states were relaxed using the LBFGS method until the maximum force was below 10^{-4} Hartree/Bohr. The geodesic interpolation method [105] was then employed to construct an initial trajectory, typically consisting of 9 images. This interpolated path served as the starting point for a CI-NEB calculation or, taking the middle image, as a starting point for the dimer method, depending on the expected complexity of the transition path.

To ensure global diffusion is possible throughout the crystal, it is important to identify the highest energy barrier among the selected transitions as the most

Algorithm 5.1: Pseudocode for identifying relevant transition path candidates in a crystal. Performance optimization was not prioritized in any way since the computational bottleneck are the NEB calculations.

```
Data: List of atoms and lattice vectors, relevant Wyckoff postion
Result: Set of relevant transition paths and their distances
begin
    Determine Wyckoff positions of the given atoms
    wyckoffAtoms ← atoms in relevant Wyckoff positions
    candidateTransitions ← ∅
    for atomA ∈ wyckoffAtoms do
        for atomB ∈ wyckoffAtoms \ {atomA} do
            for latticeVec ∈ latticeVectors ∪ {0} do
                distance ← |pos(atomA) − pos(atomB) + latticeVec|
                candidateTransitions[distance] ←
                 candidateTransitions[distance] ∪ (atomA, atomB)
            end
        end
    end
    sortedDistances ← sort(keys(candidateTransitions))
    graphAtoms, graphEdges ← wyckoffAtoms, ∅
    relevantDistances ← ∅
    for dist ∈ sortedDistances do
        graphEdges ← graphEdges ∪ candidateTransitions[dist]
        relevantDistances ← relevantDistances ∪ {dist}
        if (graphAtoms, graphEdges) is a connected graph then
            break
        end
    end
    return relevantDistances, graphEdges
end
```

important barrier. This barrier likely governs the overall diffusion behavior, as it represents the limiting step required to maintain a connected network of migration paths.

5.3.2 NEB and Dimer Settings

For all transition state calculations, either the CI-NEB method or the κ-dimer method [106], as described in Sec. 3.5.3, was used. In cases where it was suspected that the dimer method might not locate the correct transition state, or where convergence could not be achieved within a single run, the CI-NEB method was applied instead. Although computationally more expensive, the CI-NEB method is generally more robust and provides a complete picture of the transition path. To validate the results obtained with the dimer method, the identified transition state was visually inspected at first. Additionally, a linear interpolation between the initial, transition, and final states was performed and the energies of the interpolated images were evaluated. If the results did not align with expectations, the CI-NEB method was subsequently employed to ensure accuracy.

Conjugate gradients were used for the rotation and translation steps of the dimer method with an angle tolerance of 5° and a maximum remaining force of $4.5 \cdot 10^{-4}$ Hartree/Bohr.

For the CI-NEB calculations, a spring constant of 0.05 Hartree/Bohr^2, a maximum force of 0.02 Hartree/Bohr, and a maximum displacement of $2 \cdot 10^{-4}$ Bohr was used.

5.3.3 CaF_2 - Calcium Fluoride

There is just one unique transition path for CaF_2, for which the barrier is calculated for charge states +1 and 0. The results are shown in Tab. 5.4.

These barriers are in line with experimental results, which yield 0.36 eV for the migration of an F center [142]. The +1 defect charge state, which corresponds to the 0.27 eV barrier, is also thermodynamically the most favorable.

Charge State	Distance	Barrier Height
0	2.75 Å	1.28 eV
+1	2.75 Å	0.27 eV

Table 5.4: CaF_2 transition barriers. The provided distance is the distance between the start and end point in the pristine crystal structure. The real diffusion length is not exactly the same since the relaxed structure features different equilibrium positions due to the distortion introduced by the defect.

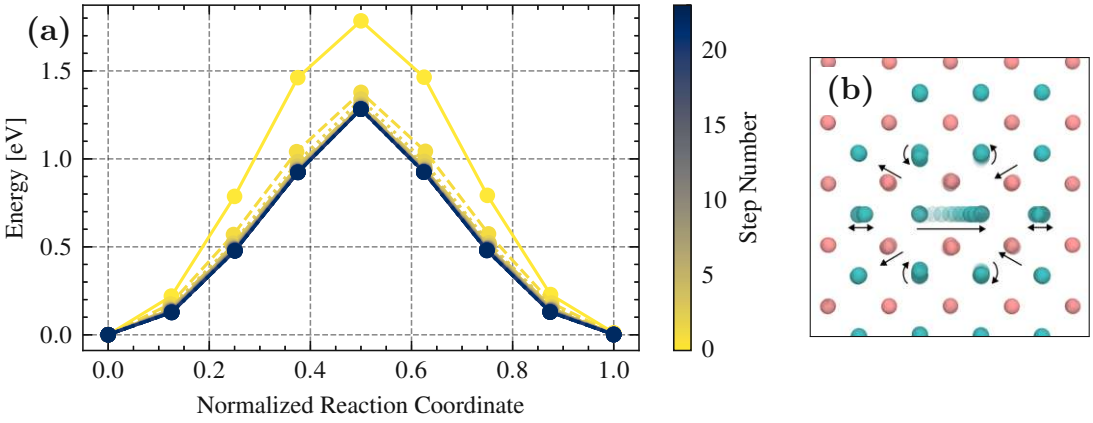

Figure 5.13: Example of a NEB calculation for the migration of a fluorine vacancy with charge state 0 in CaF_2. The energy of the band is shown in (a) over all iterations. In the migration path (b), one can see that the neighbors are slightly distorted by the defect. The motion of the nuclei is indicated by the arrows.

An example of the result of a NEB calculation is shown in Fig. 5.13. One can see that the energy of the band is minimized with increasing iterations and ends when the convergence criteria are met. The migration path is a straight line for the F ion, while the surrounding of the defects are slightly strained.

5.3.4 BiF_3 - Bismuth Trifluoride

There are three unique transitions between the 8*d* sites for the +1 charge state that are necessary to enable global diffusion, as shown in Table 5.5. For comparison, a transition between the 4*c* and 8*d* sites was also calculated. The resulting barrier from 4*c* to 8*d* is comparable to the diffusion barriers observed within the 8*d* positions. This suggests that a vacancy initially located at a 4*c* site is likely to relax into an 8*d* position, further supporting the conclusion that the 8*d* site is the energetically most favorable location for the defect.

Sorokin *et al.* measured an activation energy of 0.48 eV using conductivity measurements [143], which is significantly higher than the barriers calculated in this work. This discrepancy may arise from alternative dominant diffusion mechanisms in the material or from the involvement of different defect charge states that were not considered in the present study. Additional experimental data and further DFT calculations are required to clarify the underlying microscopic diffusion mechanisms in this material.

Charge State	Transition	Distance	Barrier Height
+1	$8d \leftrightarrow 8d$	2.60 Å	0.080 eV
+1	$8d \leftrightarrow 8d$	2.63 Å	0.063 eV
+1	$8d \leftrightarrow 8d$	2.72 Å	0.098 eV
[+1]	$[8d \leftrightarrow 8d]$	[3.69 Å]	[1.375 eV]
{+1}	$\{4c \leftarrow 8d\}$	{2.86 Å}	{0.26 eV}
{+1}	$\{4c \rightarrow 8d\}$	{2.86 Å}	{0.10 eV}

Table 5.5: BiF_3 transition barriers. The provided distance is the distance between the start and end point in the pristine crystal structure. The real diffusion length is not exactly the same since the relaxed structure features different equilibrium positions due to the distortion introduced by the defect. The barrier in *brackets* is an additional barrier that is not needed for a complete graph computed to confirm the validity of the proposed methodology to identify the paths with the lowest migration barriers. An additional transition between the $4c$ and $8d$ site is also computed for comparison and shown in *braces*. It does not contribute to the graph connectivity in any way, but was examined to confirm the fact that the $4c$ site is not involved in the diffusion process.

5.3.5 LaF_3 - Lanthanum Trifluoride

The calculated diffusion barriers in LaF_3 are shown in Table 5.6. The barrier of 0.196 eV is required to reach global diffusion in the crystal.

Charge State	Transition	Distance	Barrier Height
+1	$12g \leftrightarrow 12g$	2.57 Å	0.114 eV
+1	$12g \leftrightarrow 12g$	2.69 Å	0.117 eV
+1	$12g \leftrightarrow 12g$	2.75 Å	0.196 eV
[+1]	$[12g \leftrightarrow 12g]$	[3.60 Å]	[1.524 eV]

Table 5.6: LaF_3 transition barriers between $12f$ positions like Table 5.5.

In conductivity measurements conducted by Roos *et al.* [146], different migration barriers were observed at various temperatures, showing approximately isotropic behavior. The measured activation energies were around 0.84 eV at low temperatures and 0.26 eV and 0.46 eV at higher temperatures, as schematically illustrated in Fig. 5.14. Additional measurements by Sinitsyn *et al.* [145] reported activation barriers of 1.22 eV, 0.18 eV, and 0.34 eV. The authors suggested that primarily the $2a$ and $4d$ fluorine ions contribute to the conductivity, which does not align with the findings in this thesis.

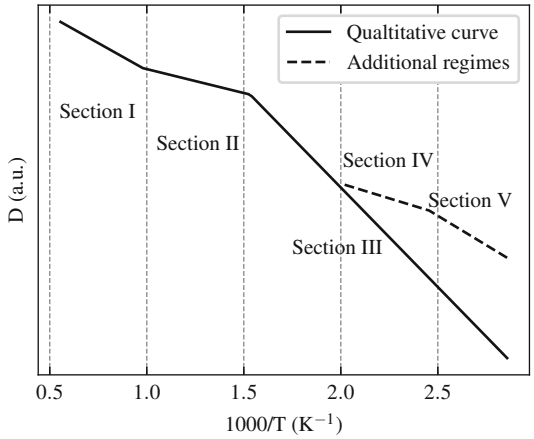

Figure 5.14: Qualitative Arrhenius plot illustrating diffusion in LaF_3. This schematic plot is meant to aid interpretation and does not reflect actual measurements. At very low temperatures, Fujara *et al.* [144] reported the appearance of two additional diffusion mechanisms with distinct activation energies. However, these features were not confirmed by other studies [145, 146] and are therefore indicated as dashed lines in the plot.

Doping the material with elements such as Ba or Sr has been shown to alter these barriers, increasing the energy for transitions between $12f$ positions and decreasing it for jumps involving the $2a$ and $4d$ positions [146].

A study combining NMR and conductivity measurements [144] revealed aging effects in the material. These effects lowered the diffusion barriers, and it was shown that different diffusion mechanisms emerged after multiple heating cycles. The authors proposed that the freshly grown crystal contained fewer fluorine vacancies, which began to form with aging. This study also reported a lower diffusion barrier of around $0.1 - 0.2\,\text{eV}$ in the secondary diffusion regime, attributed to external defects not considered in this work.

Nevertheless, the $0.26\,\text{eV}$ migration barrier is suggested by Roos *et al.* to correspond to vacancy diffusion throughout the crystal [146], which aligns with the calculated barriers between the $12g$ fluorine defect positions presented in this work.

5.3.6 ZrF_4 - Zirconium Tetrafluoride

ZrF_4 contains 16 fluorine atoms per unit cell, equally distributed among four distinct $4e$ positions. However, only the $4e_1$ position is stable, resulting in relatively large distances between feasible diffusion sites. Due to their instability,

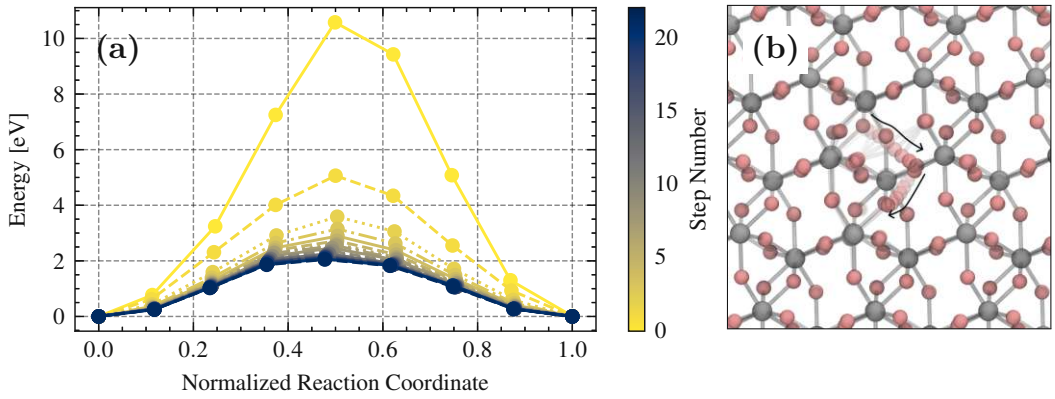

Figure 5.15: Example of a combined transition path in ZrF_4 from $4e_1$ to $4e_1$ via a $4e_2$ position. The energy of the band over all iterations of the NEB calculation is shown in **(a)**, while **(b)** shows the migration path of the fluorine vacancy indicating motion with arrows. There are two nuclei involved and they move at the same time. The fluorine ions are shown in light pink, while Zr atoms are shown in gray.

the $4e_2$ and $4e_3$ positions are not suitable as initial or final states for transition state calculations.

Using the same methodology applied to other materials, relevant migration paths were identified. Given the large distances between stable $4e_1$ positions, both direct transitions (where fluorine ions move directly from one $4e_1$ position to another) and indirect transitions (involving intermediate unstable positions $4e_2$ or $4e_3$) were considered. An example illustrating such a migration pathway is depicted in Fig. 5.15.

The calculated barriers are not converged to the same accuracy as for the other materials. However, they are sufficiently converged to show the comparatively high barriers for these transitions.

The results indicate that the migration barriers between the $4e_1$ positions are very high, likely due to the large physical distances between these sites. It is important to note that all calculated barriers use the $4e_1$ positions as both start and end points. Transitions involving other positions were also considered, but since $4e_2$ and $4e_3$ positions are unstable, only transitions between $4e_1$ and $4e_4$ remain potentially relevant. To evaluate this, the final transition required for global diffusion, as identified by the proposed methodology, was calculated. This path also yielded a high barrier of more than 3.5 eV.

These findings suggest that fluorine vacancy migration in ZrF_4 is associated with significantly higher activation barriers than the other examined fluorides.

Charge State	Transition	Distance	Barrier Height
+1	$4e_1 \leftrightarrow 4e_1$	2.34 Å	0.04 eV
+1	$4e_1 \leftarrow 4e_2 \rightarrow 4e_1$	4.14 Å	1.8 eV
+1	$4e_1 \leftrightarrow 4e_1$	4.14 Å	2.3 eV
+1	$4e_1 \leftrightarrow 4e_1$	4.15 Å	1.6 eV
+1	$4e_1 \leftarrow 4e_2 \rightarrow 4e_1$	4.15 Å	2 eV
+1	$4e_1 \leftarrow 4e_3 \rightarrow 4e_1$	4.15 Å	3 eV
+1	$4e_1 \leftarrow 4e_3 \rightarrow 4e_1$	4.526 Å	2.8 eV

Table 5.7: ZrF_4 transition barriers between $4e_1$ positions as in Table 5.5. It is important to note that all transitions listed are necessary to enable global diffusion throughout the crystal. Therefore, the highest barriers, rather than the lowest, determine the overall diffusion behavior. For instance, while the extremely low barrier of 0.04 eV may appear favorable, it does not dominate the diffusion process if higher barriers are present elsewhere along the path. The Transition column in the table indicates the specific migration path considered. Arrows denote the migration route taken. For example, the 4.15 Å transition barrier was evaluated both for direct migration and for two more complex paths via the $4e_2$ and $4e_3$ positions, as illustrated in Fig. 5.15.

Nevertheless, it is possible that alternative diffusion paths not examined in this work could exist. Additionally, other defect types such as fluorine interstitials or extrinsic impurities may play a role in the diffusion mechanisms of this material.

No experimental data on the diffusion activation energy in ZrF_4 was found in the literature. Further studies, for instance using molecular dynamics simulations, could provide additional insight. Given the substantially different and more complex diffusion process compared to the other fluorides, present results should be viewed only as an initial exploration of the diffusion characteristics of ZrF_4.

5.4 Discussion

In contrast to BiF_3 and CaF_2, fluorine vacancies in ZrF_4 and LaF_3 are only stable in the +1 charge state for all Fermi levels within their band gap. This means that these defects are likely electrically inactive and do not cause instabilities such as BTI, RTN, and trap-assisted tunneling, however, due to their fixed positive charge, they can lead to a permanent voltage shift in MOS devices.

BiF_3, CaF_2 and LaF_3 show low vacancy migration barriers, which are mostly in line with experimental results, whenever available. Ionic diffusion can enhance the static dielectric constant of the material, but due to the slow nature of

diffusion, this only occurs at very low frequencies [16]. However, the hysteresis caused by the ion drift in MOS devices [137] negatively influences the reliability of devices and needs to be carefully studied in further TCAD simulations if the material is used in devices. ZrF_4 seems to behave quite different in this regard, as the barriers were found to be very high, which could be beneficial for the reliability of devices.

Limitations

Only some possible diffusion paths were considered to keep the amount of calculations manageable within the scope of this work. For BiF_3 two further charge states (-1 and -3) also have a range of Fermi levels where they have the lowest formation energy. They were not considered in this work, as the $+1$ state is the most stable for a wide range of Fermi levels. The theoretical results of BiF_3 are quite different from the limited available experimental data, considering just band gap and permittivity results. This could be a sign that the real material might have a different microscopic structure than expected and that other defects or impurities change the behavior of the material.

Experimental studies in LaF_3 linked diffusion behavior to other defect positions, which are less likely to form according to the formation energy analysis in this thesis. Additional theoretical considerations towards diffusion of these different defect states are needed to better understand the complex diffusion behavior of LaF_3. Many other impurities and crystal defects are possible and need to be thoroughly studied. As discussed in previous sections, such defects could enable other diffusion mechanisms and introduce additional trap levels.

CHAPTER 6

CONCLUSIONS AND OUTLOOK

A semi-automated workflow for the calculation of the permittivity and band gap was developed that could be further enhanced to fully enable high-throughput calculations using CP2K and PHONOPY. Using this framework, the permittivity and band gap of thirteen different fluoride compounds were calculated and compared to experimental and theoretical values.

After this screening, four interesting candidates that have potential as insulators in future devices were selected for further exploration. The transition energy barriers for fluorine vacancy diffusion were calculated for four selected materials. In this process, a graph-based method to limit the amount of required barrier calculations was developed, which was also verified to identify relevant low energy migration pathways.

LaF_3 seems to be a promising material to be used as an insulator. It has a decent permittivity of 14.2 and a large calculated band gap of 9.91 eV. Additionally, the vacancy defects have the lowest formation energy for the charge +1 state for all external potentials. It has a rather low diffusion barrier for F vacancy migration, which could further increase low frequency permittivity, but might not be beneficial for device reliability, due to an associated hysteresis.

BiF_3 is also an interesting material due to its very high calculated permittivity of 46 and decent band gap of 6.6 eV. However, differences to the available experimental data are comparatively large, which could indicate that the experimentally examined material differs in microscopic structure from the perfect crystal structure used in the calculations. The vacancy defects might exist in various charge states, and have very low calculated diffusion barriers. This is very likely not optimal for device reliability, but cannot be conclusively stated without further investigation. Unfortunately, it is also listed as a chemically corrosive material, which might complicate fabrication and device integration [147], although only one source reports corrosivity against metals. ZrF_4 with a computed band gap of 7.6 eV and permittivity of 10.8 was also found to be a good candidate, mainly because of its high fluorine vacancy diffusion barrier. Further investigation is needed for this material to see if no migration pathways were missed with the employed NEB calculations.

In general, the results of this thesis confirm favorable properties of fluorides also found in other studies, and enhances the understanding of vacancy defects

in these materials. Based on the presented findings, a path for further research towards integration of fluorides as insulators is proposed:

- Study different diffusion charge states for BiF_3 and different defect positions for LaF_3.
- Investigate further point defects in the materials LaF_3 and BiF_3.
- Examine ZrF_4 using molecular dynamics simulations to see if the diffusion barriers were correctly identified in this work.
- Conduct TCAD simulations of MOS devices using obtained material properties to see their influence on device behavior.
- Experimental deposition of fluoride thin films using evaporation or epitactic growth techniques and characterization to verify the suitability for device integration.
- Fabrication and characterization of devices using these materials as gate dielectric.

APPENDIX A

MATERIAL PARAMETERS

Table A.1: Main material parameters of the simulated crystal structures

Material	A [Å]	B[Å]	C [Å]	α[°]	β[°]	γ[°]	Band Gap [eV]	ε_{tot}
BiF_3^{Fm3m}	5.77	5.77	5.77	90.0	90.0	90.0	5.79	26.77
BiF_3^{Pnma}	6.88	7.26	4.44	90.0	90.0	90.0	6.61	46.56
$CaF_2^{Fm\bar{3}m}$	5.50	5.50	5.50	90.0	90.0	90.0	9.05	7.09
CaF_2^{Pnma}	5.98	3.62	7.06	90.0	90.0	90.0	9.52	10.79
$CeF_4^{C2/c}$	12.63	21.37	8.27	90.0	126.3	90.0	4.99	17.20
$FeF_2^{P4_2/mnm}$	4.59	4.59	3.03	90.0	90.0	90.0	4.03	3.61
$HfF_4^{C2/c}$	11.69	9.88	7.65	90.0	126.1	90.0	7.48	11.65
$LaF_3^{P\bar{3}c1}$	7.20	7.20	7.37	90.0	90.0	120.0	9.91	14.22
$LaF_3^{P6_3cm}$	7.19	7.19	7.37	90.0	90.0	120.0	9.93	14.16
$LaF_3^{P6_3/mmc}$	4.16	4.16	7.38	90.0	90.0	120.0	9.49	13.99
LaF_3^{Pmmn}	4.17	5.32	4.56	90.0	90.0	90.0	8.91	18.96
$PbF_2^{Fm\bar{3}m}$	6.00	6.00	6.00	90.0	90.0	90.0	5.59	23.41
$ScF_3^{Pm3\bar{m}}$	4.04	4.04	4.04	90.0	90.0	90.0	8.41	7.01
$SnF_2^{C2/c}$	13.19	5.15	14.14	90.0	107.7	90.0	4.26	21.38
$SrF_2^{Fm\bar{3}m}$	5.83	5.83	5.83	90.0	90.0	90.0	8.79	6.40
TiF_4^{Pnma}	23.95	3.87	9.92	90.0	90.0	90.0	6.37	8.42
TlF^{Pbcm}	6.26	5.70	5.17	90.0	90.0	90.0	4.34	17.29
YF_3^{Pnma}	6.45	6.90	4.36	90.0	90.0	90.0	9.89	10.60
$ZrF_4^{C2/c}$	11.90	10.04	7.78	90.0	126.1	90.0	6.76	14.91
$ZrF_4^{P2_1/c}$	5.64	5.63	8.03	90.0	105.7	90.0	7.60	10.77
$ZrF_4^{P4_2/m}$	7.97	7.97	7.79	90.0	90.0	90.0	7.12	12.19

Table A.2: Electronic and ionic permittivity tensors for all materials.

Material	$\underline{\boldsymbol{\varepsilon}}_{\mathrm{el}}$	$\underline{\boldsymbol{\varepsilon}}_{\mathrm{ion}}$
$BiF_3^{Fm\bar{3}m}$	$\begin{bmatrix} 3.62 & 0 & 0 \\ 0 & 3.62 & 0 \\ 0 & 0 & 3.62 \end{bmatrix}$	$\begin{bmatrix} 34.34 & 0 & 0.10 \\ 0 & 34.34 & 0 \\ 0.10 & 0 & 0.74 \end{bmatrix}$
BiF_3^{Pnma}	$\begin{bmatrix} 3.07 & 0 & 0 \\ 0 & 3.01 & 0 \\ 0 & 0 & 2.94 \end{bmatrix}$	$\begin{bmatrix} 53.72 & 0 & 0 \\ 0 & 42.44 & 0 \\ 0 & 0 & 34.50 \end{bmatrix}$
$CaF_2^{Fm\bar{3}m}$	$\begin{bmatrix} 1.91 & 0 & 0 \\ 0 & 1.91 & 0 \\ 0 & 0 & 1.91 \end{bmatrix}$	$\begin{bmatrix} 5.13 & 0 & 0 \\ 0 & 5.24 & 0 \\ 0 & 0 & 5.17 \end{bmatrix}$
CaF_2^{Pnma}	$\begin{bmatrix} 1.95 & 0 & 0 \\ 0 & 1.99 & 0 \\ 0 & 0 & 1.98 \end{bmatrix}$	$\begin{bmatrix} 8.96 & 0 & 0 \\ 0 & 7.56 & 0 \\ 0 & 0 & 9.91 \end{bmatrix}$
$CeF_4^{C2/c}$	$\begin{bmatrix} 2.48 & 0 & -0.11 \\ 0 & 2.67 & 0 \\ -0.11 & 0 & 2.48 \end{bmatrix}$	$\begin{bmatrix} 15.40 & 0 & 0 \\ 0 & 13.69 & 0.05 \\ 0 & 0.05 & 14.88 \end{bmatrix}$
$FeF_2^{P4_2/mnm}$	$\begin{bmatrix} 2.35 & 0 & 0 \\ 0 & 2.35 & 0 \\ 0 & 0 & 2.45 \end{bmatrix}$	$\begin{bmatrix} 1.22 & 0 & 0 \\ 0 & 1.22 & 0 \\ 0 & 0 & 1.23 \end{bmatrix}$
$HfF_4^{C2/c}$	$\begin{bmatrix} 2.16 & 0 & -0.08 \\ 0 & 2.34 & 0 \\ -0.08 & 0 & 2.19 \end{bmatrix}$	$\begin{bmatrix} 10 & 0 & 0.14 \\ 0 & 7.89 & 0 \\ 0.14 & 0 & 10.36 \end{bmatrix}$
$LaF_3^{P\bar{3}c1}$	$\begin{bmatrix} 2.37 & 0 & 0 \\ 0 & 2.37 & 0 \\ 0 & 0 & 2.37 \end{bmatrix}$	$\begin{bmatrix} 12.97 & 0 & 1.07 \\ 0 & 11.99 & 0 \\ 1.07 & 0 & 10.60 \end{bmatrix}$
$LaF_3^{P6_3cm}$	$\begin{bmatrix} 2.37 & 0 & 0 \\ 0 & 2.37 & 0 \\ 1.88 & 1.88 & 4.26 \end{bmatrix}$	$\begin{bmatrix} 11.87 & 0.82 & 0 \\ 0.82 & 12.92 & 0 \\ 0 & 0 & 8.69 \end{bmatrix}$
$LaF_3^{P6_3/mmc}$	$\begin{bmatrix} 2.32 & -0.01 & 0 \\ -0.01 & 2.31 & 0 \\ 0 & 0 & 2.38 \end{bmatrix}$	$\begin{bmatrix} 12.22 & 0 & 0 \\ 0 & 12.22 & 0 \\ 0 & 0 & 10.50 \end{bmatrix}$
LaF_3^{Pmmn}	$\begin{bmatrix} 2.58 & 0 & 0 \\ 0 & 2.59 & 0 \\ 0 & 0 & 2.51 \end{bmatrix}$	$\begin{bmatrix} 13.83 & 0 & 0 \\ 0 & 19.53 & 0.03 \\ 0 & 0.03 & 15.85 \end{bmatrix}$
$PbF_2^{Fm\bar{3}m}$	$\begin{bmatrix} 2.70 & 0 & 0 \\ 0 & 2.70 & 0 \\ 0 & 0 & 2.70 \end{bmatrix}$	$\begin{bmatrix} 21.34 & 0.01 & 0 \\ 0.01 & 20.41 & 0 \\ 0 & 0 & 20.39 \end{bmatrix}$

$ScF_3^{Pm\bar{3}m}$	$\begin{bmatrix} 1.88 & 0 & 0 \\ 0 & 1.88 & 0 \\ 0 & 0 & 1.88 \end{bmatrix}$	$\begin{bmatrix} 5.14 & 0 & 0 \\ 0 & 5.14 & 0 \\ 0 & 0 & 5.14 \end{bmatrix}$
$SnF_2^{C2/c}$	$\begin{bmatrix} 2.89 & 0 & 0.02 \\ 0 & 2.78 & 0 \\ 0.02 & 0 & 2.89 \end{bmatrix}$	$\begin{bmatrix} 31.91 & 0.25 & 0 \\ 0.25 & 8.36 & 0 \\ 0 & 0 & 15.31 \end{bmatrix}$
$SrF_2^{Fm\bar{3}m}$	$\begin{bmatrix} 1.87 & 0 & 0 \\ 0 & 1.87 & 0 \\ 0 & 0 & 1.87 \end{bmatrix}$	$\begin{bmatrix} 4.54 & 0 & 0 \\ 0 & 4.54 & 0 \\ 0 & 0 & 4.54 \end{bmatrix}$
TiF_4^{Pnma}	$\begin{bmatrix} 2.08 & 0 & 0 \\ 0 & 1.92 & 0 \\ 0 & 0 & 2.05 \end{bmatrix}$	$\begin{bmatrix} 2.21 & 0 & 0 \\ 0 & 15.01 & 0 \\ 0 & 0 & 1.99 \end{bmatrix}$
TlF^{Pbcm}	$\begin{bmatrix} 3.50 & 0 & 0 \\ 0 & 3.51 & 0 \\ 0 & 0 & 3.53 \end{bmatrix}$	$\begin{bmatrix} 4.04 & 0 & 0 \\ 0 & 12.03 & 0 \\ 0 & 0 & 25.26 \end{bmatrix}$
YF_3^{Pnma}	$\begin{bmatrix} 2.32 & 0 & 0 \\ 0 & 2.26 & 0 \\ 0 & 0 & 2.20 \end{bmatrix}$	$\begin{bmatrix} 6.96 & 0 & 0 \\ 0 & 6.44 & 0 \\ 0 & 0 & 11.61 \end{bmatrix}$
$ZrF_4^{C2/c}$	$\begin{bmatrix} 2.42 & 0 & -0.04 \\ 0 & 2.45 & 0 \\ -0.04 & 0 & 2.29 \end{bmatrix}$	$\begin{bmatrix} 14.05 & 0 & 0.07 \\ 0 & 9.07 & 0 \\ 0.07 & 0 & 14.46 \end{bmatrix}$
$ZrF_4^{P2_1/c}$	$\begin{bmatrix} 2.37 & 0 & 0.01 \\ 0 & 2.37 & 0 \\ 0.01 & 0 & 2.44 \end{bmatrix}$	$\begin{bmatrix} 6.64 & 0 & 0.42 \\ 0 & 8.14 & 0 \\ 0.42 & 0 & 10.37 \end{bmatrix}$
$ZrF_4^{P4_2/m}$	$\begin{bmatrix} 2.37 & 0 & 0 \\ 0 & 2.37 & 0 \\ 0 & 0 & 2.36 \end{bmatrix}$	$\begin{bmatrix} 10.61 & 0 & 0 \\ 0 & 10.61 & 0 \\ 0 & 0 & 8.25 \end{bmatrix}$

APPENDIX B

PHONON DISPERSION OF SIMULATED STRUCTURES

In this section, the phonon dispersion of all stable compounds examined in this work are shown. The phonon dispersion relations describe how vibrational frequencies (phonons) in a crystal depend on their wave vector q.

In DFT simulations, the presence of negative (imaginary) phonon frequencies indicates dynamic instability. Such modes suggest that the current crystal structure is not at a true energy minimum and may spontaneously distort to a more stable configuration. These instabilities can arise from numerical issues or signify potential phase transitions. If a crystal structure exhibits imaginary frequencies while being expected to be stable (e.g. through experimental data) this is an indication that the DFT calculation setup (supercell, cutoffs) might not be suited for this material [84].

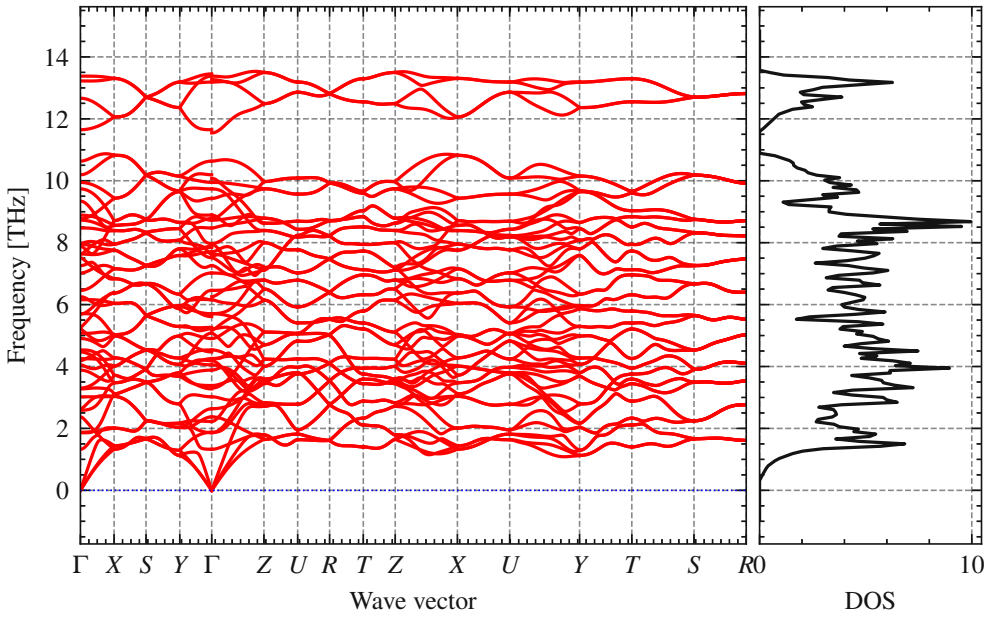

Figure B.1: Phonon dispersion of BiF_3

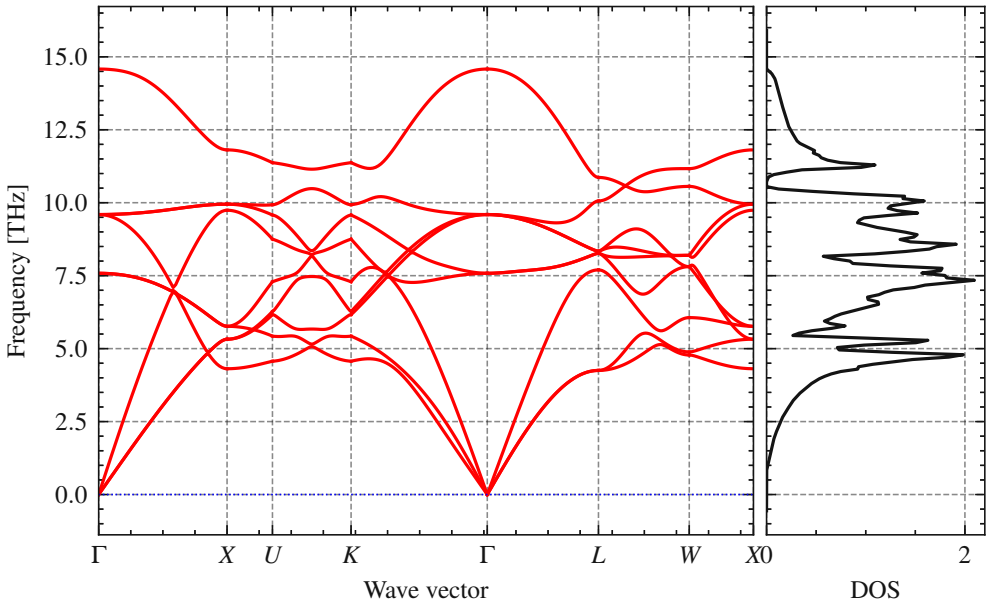

Figure B.2: Phonon dispersion of CaF_2

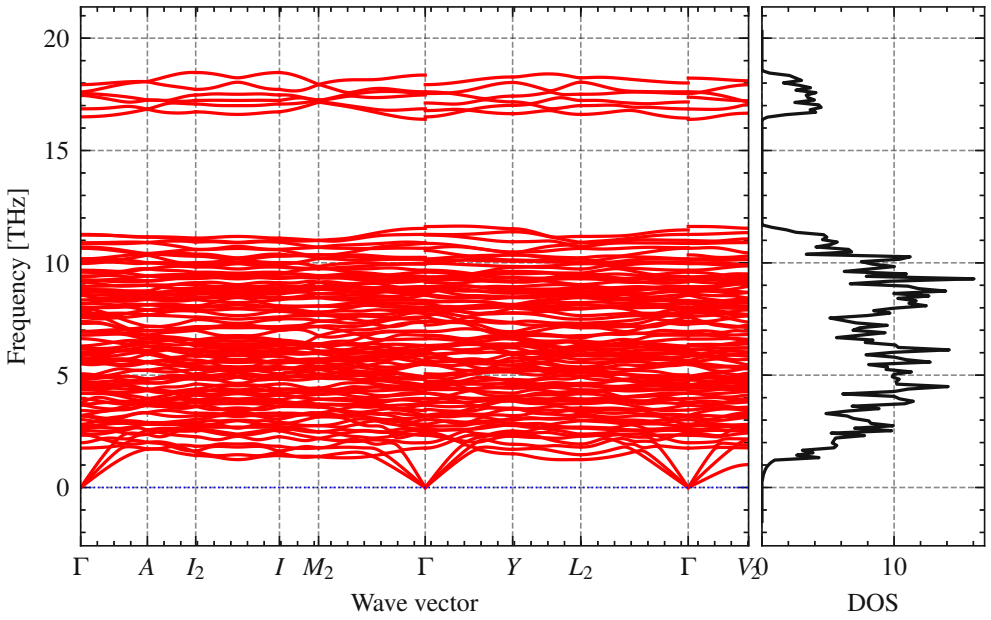

Figure B.3: Phonon dispersion of CeF_4

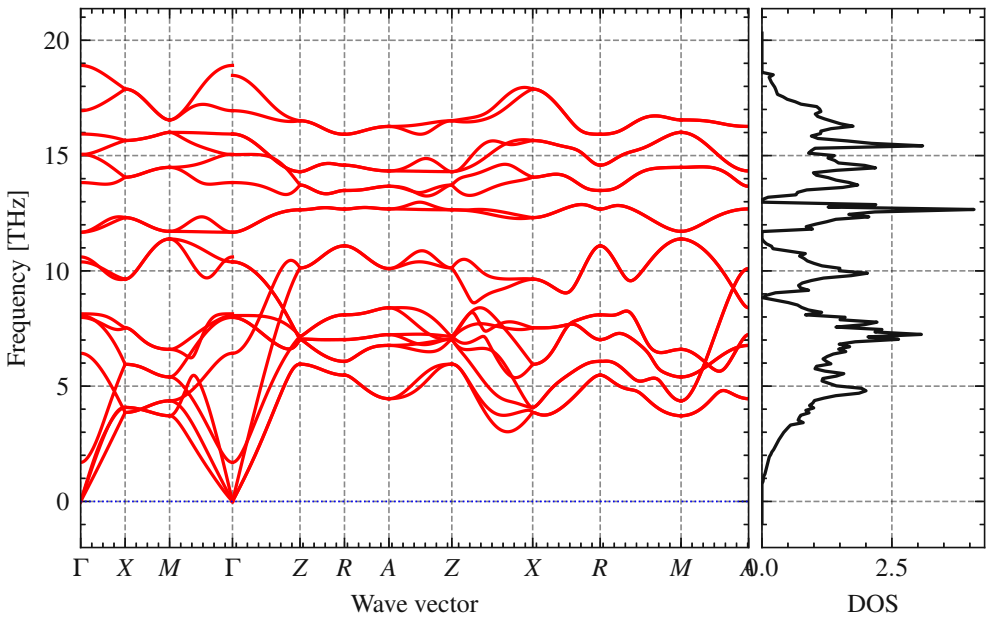

Figure B.4: Phonon dispersion of FeF_2

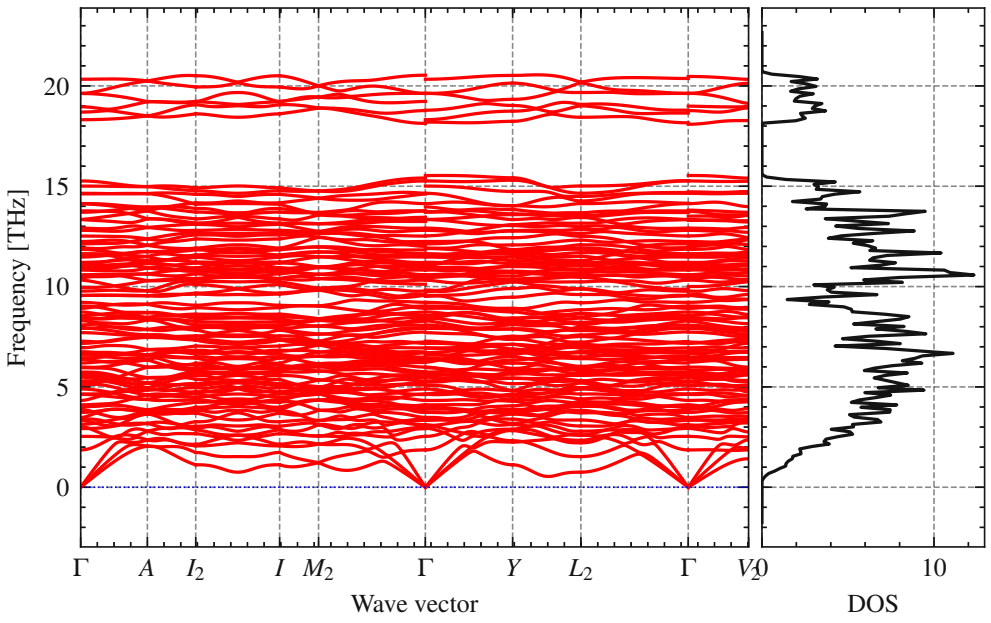

Figure B.5: Phonon dispersion of HfF_4

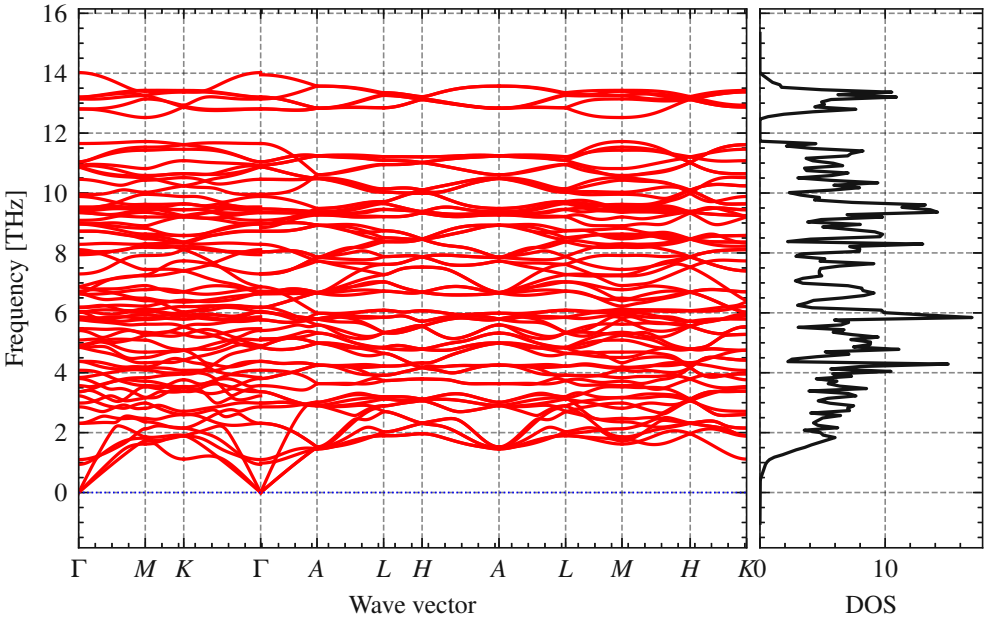

Figure B.6: Phonon dispersion of LaF_3

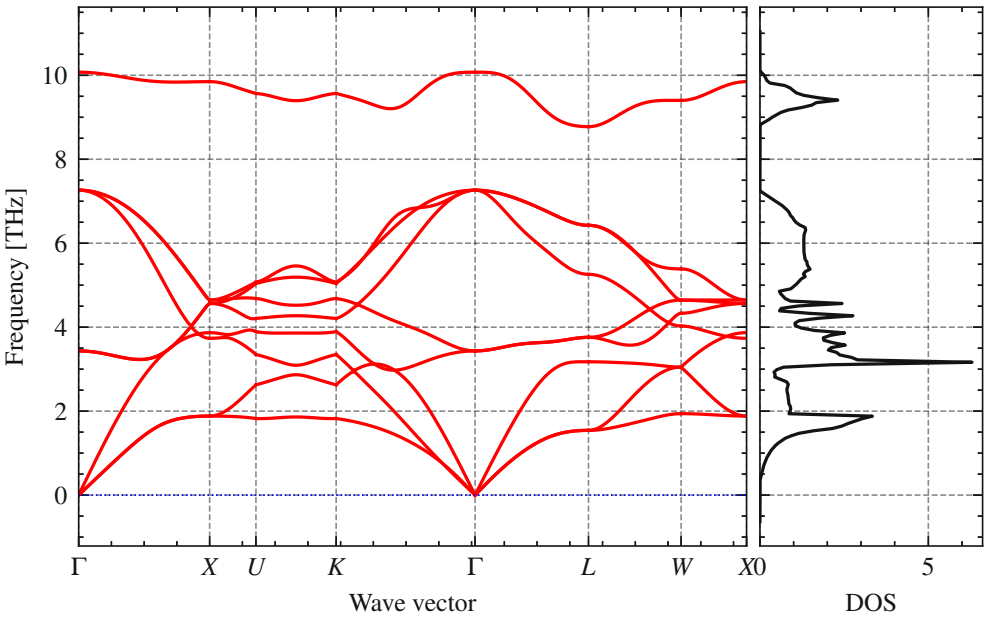

Figure B.7: Phonon dispersion of PbF_2

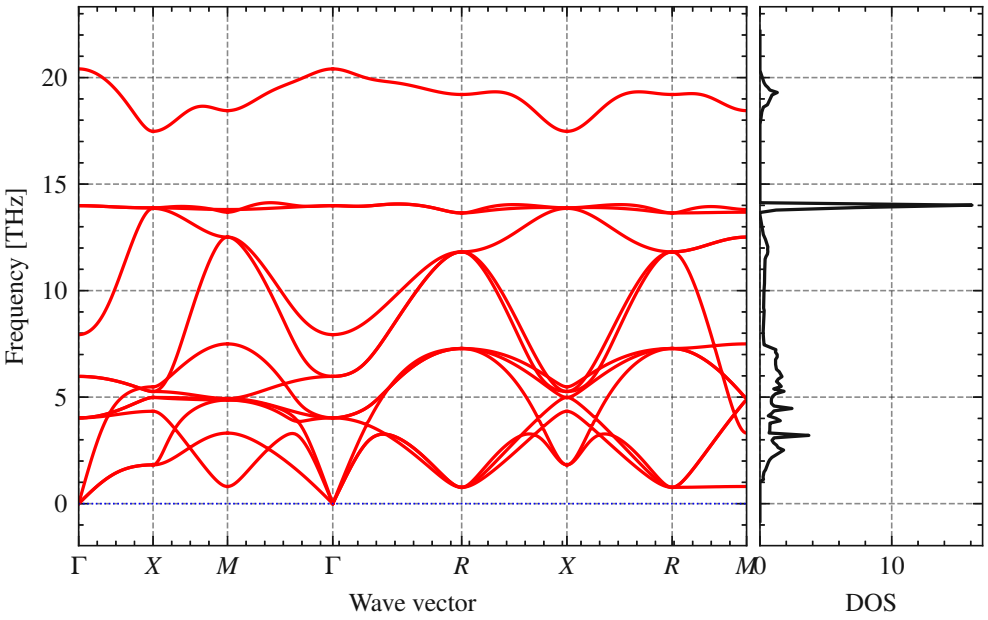

Figure B.8: Phonon dispersion of ScF_3

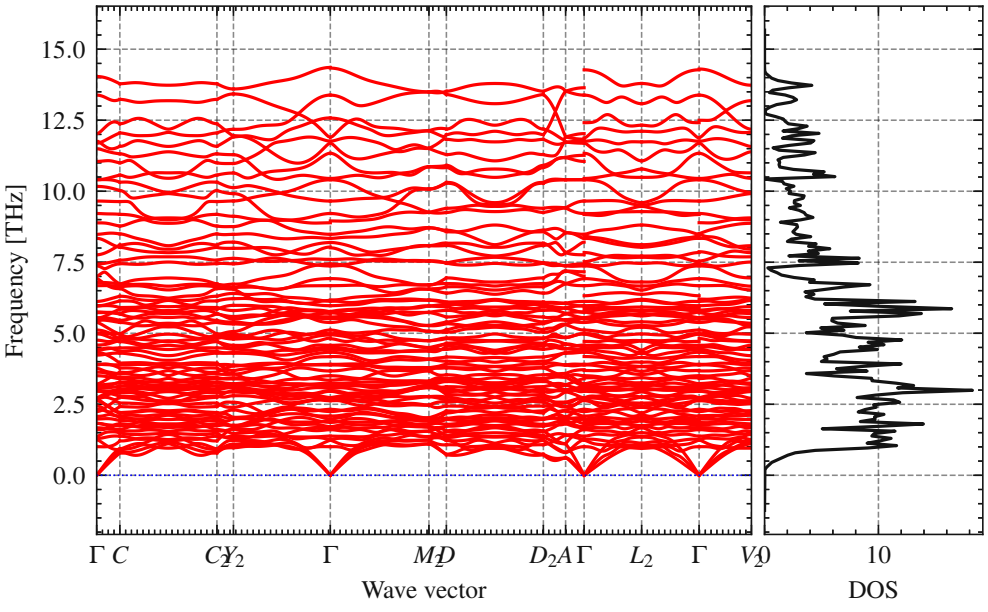

Figure B.9: Phonon dispersion of SnF_2

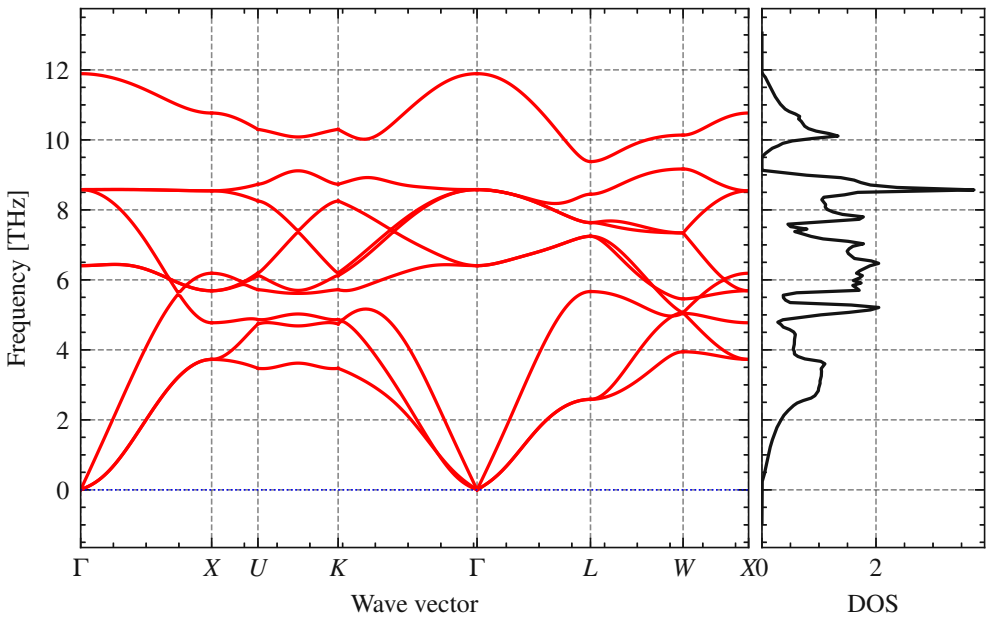

Figure B.10: Phonon dispersion of SrF_2

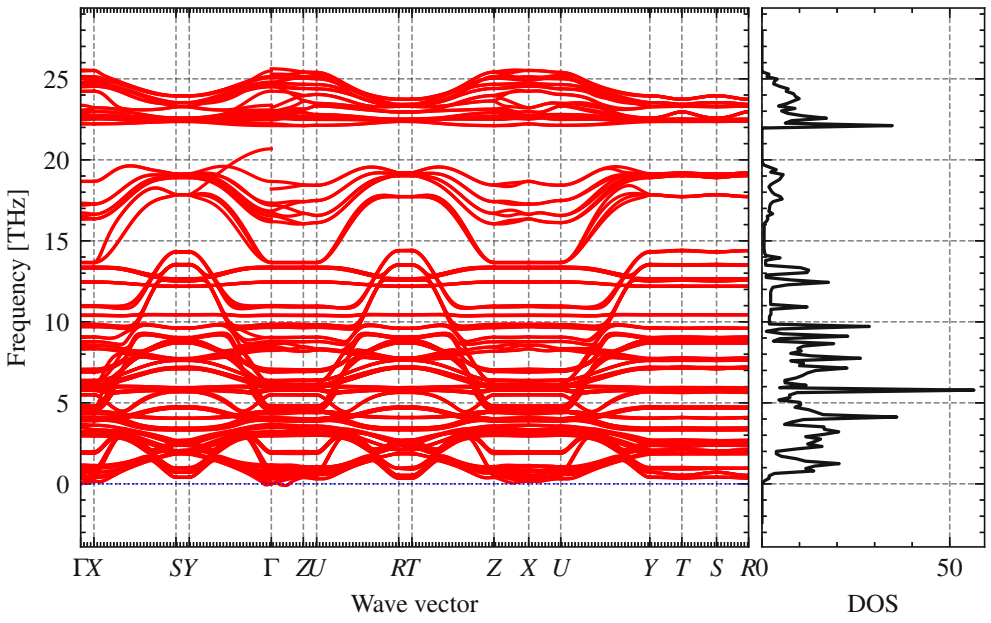

Figure B.11: Phonon dispersion of TiF_4

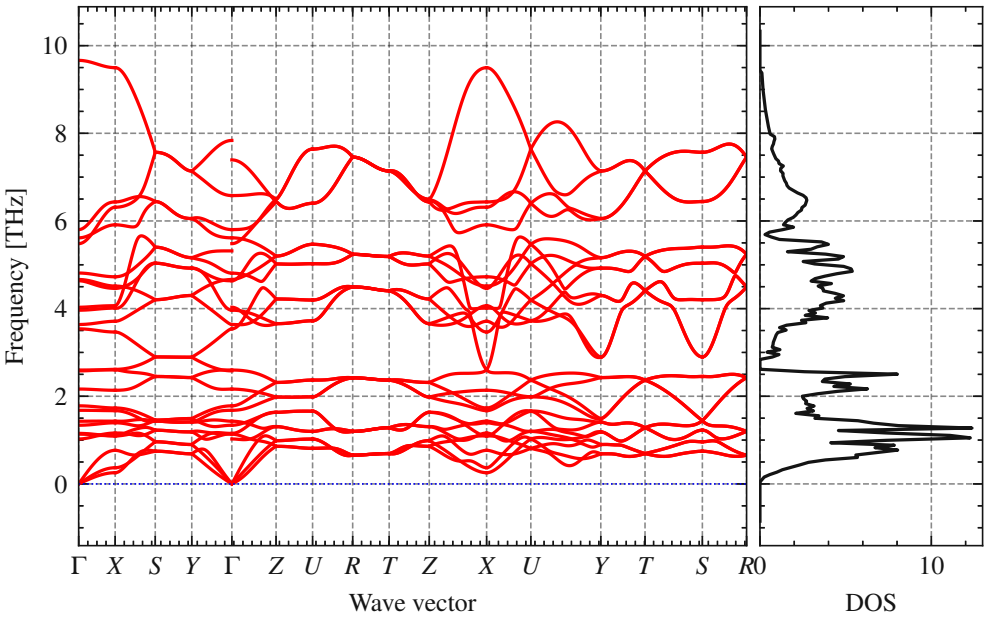

Figure B.12: Phonon dispersion of TlF

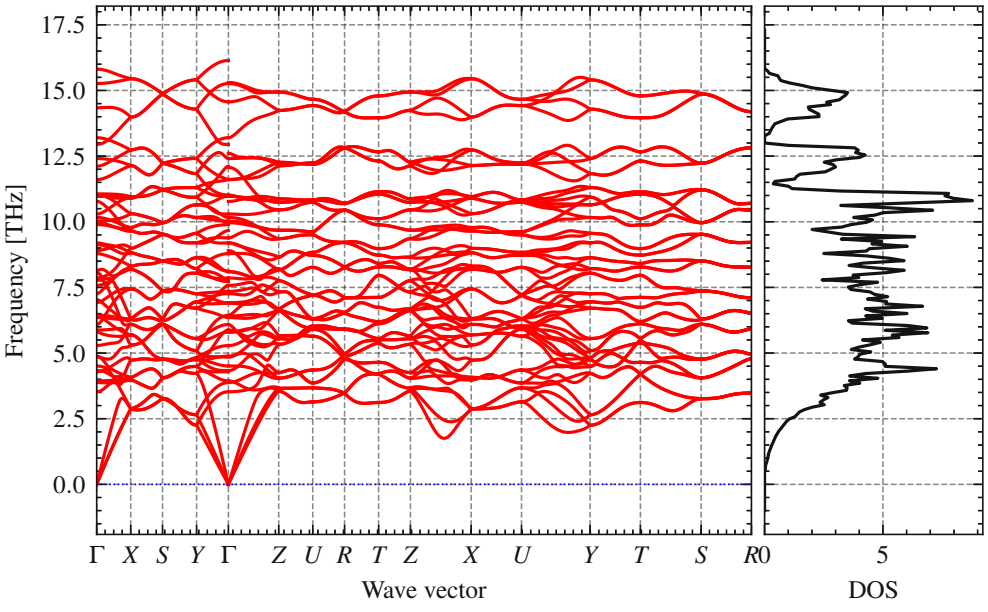

Figure B.13: Phonon dispersion of YF_3

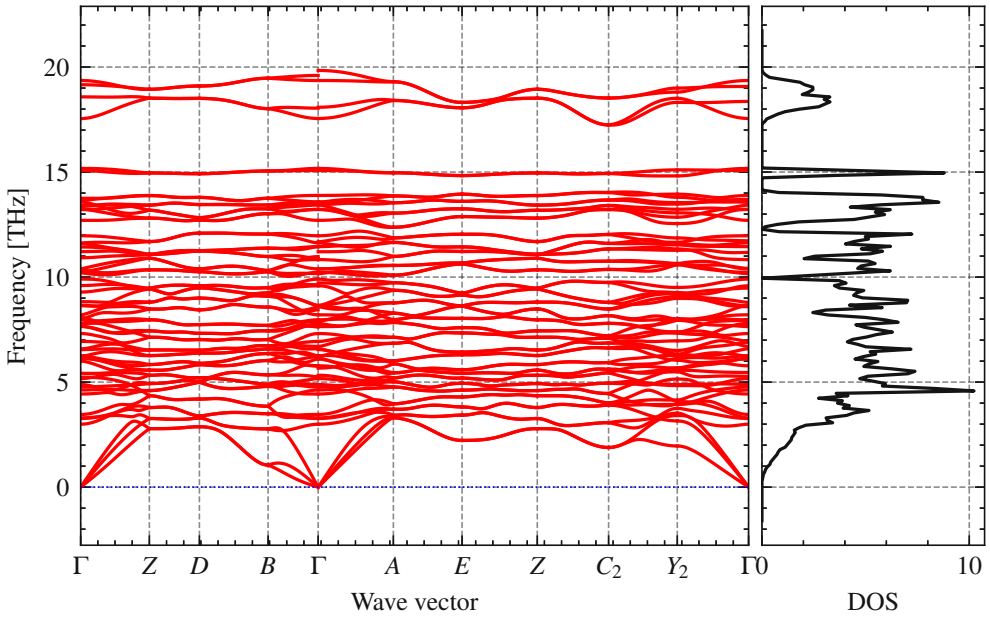

Figure B.14: Phonon dispersion of ZrF_4

BIBLIOGRAPHY

[1] C. R. Helms and B. E. Deal, Eds., *The Physics and Chemistry of SiO_2 and the Si-SiO_2 Interface*. Boston, MA: Springer US, 1988, ISBN: 978-1-4899-0776-9 978-1-4899-0774-5. DOI: 10.1007/978-1-4899-0774-5.

[2] J. Brews, W. Fichtner, E. Nicollian, and S. Sze, "Generalized guide for MOSFET miniaturization," *IEEE Electron Device Letters*, vol. 1, no. 1, pp. 2–4, Jan. 1980, ISSN: 1558-0563. DOI: 10.1109/EDL.1980.25205.

[3] X. Guo and T. Ma, "Tunneling leakage current in oxynitride: Dependence on oxygen/nitrogen content," *IEEE Electron Device Letters*, vol. 19, no. 6, pp. 207–209, Jun. 1998, ISSN: 1558-0563. DOI: 10.1109/55.678546.

[4] H. R. Huff, *High Dielectric Constant Materials: VLSI MOSFET Applications* (Springer Series in Advanced Microelectronics). Berlin: Springer, 2005, xxiv+710, ISBN: 978-3-540-21081-8.

[5] Institute of Electrical and Electronics Engineers, "IEEE International Roadmap for Devices and Systems, Executive Summary," 2022. DOI: 10.60627/C13Z-V363.

[6] T. Schram, S. Sutar, I. Radu, and I. Asselberghs, "Challenges of Wafer-Scale Integration of 2D Semiconductors for High-Performance Transistor Circuits," *Advanced Materials*, vol. 34, no. 48, p. 2 109 796, 2022, ISSN: 1521-4095. DOI: 10.1002/adma.202109796.

[7] B. V. Suresh, *Solid State Devices and Technology*. Pearson Education India, Sep. 2010, 538 pp., ISBN: 978-81-317-3236-6.

[8] N. W. Ashcroft, Mermin, N. David, and D. Wei, *Solid State Physics*, Revised edition. Singapore: Cengage Learning, 2016, ISBN: 978-981-4369-89-3.

[9] C. Wei et al., "Flexible molecular crystals for optoelectronic applications," *Chemical Society Reviews*, vol. 53, no. 8, pp. 3687–3713, Apr. 22, 2024, ISSN: 1460-4744. DOI: 10.1039/D3CS00116D.

[10] M. Salmani Jelodar et al., "Tunneling: The major issue in ultra-scaled MOSFETs," in *2015 IEEE 15th International Conference on Nanotechnology (IEEE-NANO)*, Jul. 2015, pp. 670–673. DOI: 10.1109/NANO.2015.7388694.

[11] C. Schleich et al., "Single-Versus Multi-Step Trap Assisted Tunneling Currents-Part I: Theory," *IEEE Transactions on Electron Devices*, vol. 69, no. 8, pp. 4479–4485, Aug. 2022, ISSN: 1557-9646. DOI: 10.1109/TED.2022.3185966.

[12] C. Freysoldt et al., "First-principles calculations for point defects in solids," *Reviews of Modern Physics*, vol. 86, no. 1, pp. 253–305, Mar. 28, 2014, ISSN: 0034-6861, 1539-0756. DOI: 10.1103/RevModPhys.86.253.

[13] T. Grasser, "Stochastic charge trapping in oxides: From random telegraph noise to bias temperature instabilities," *Microelectronics Reliability*, 2011 Reliability of Compound Semiconductors (ROCS) Workshop, vol. 52, no. 1, pp. 39–70, Jan. 1, 2012, ISSN: 0026-2714. DOI: 10.1016/j.microrel.2011.09.002.

[14] T. Grasser et al., "The Paradigm Shift in Understanding the Bias Temperature Instability: From Reaction–Diffusion to Switching Oxide Traps," *IEEE Transactions on Electron Devices*, vol. 58, no. 11, pp. 3652–3666, Nov. 2011, ISSN: 1557-9646. DOI: 10.1109/TED.2011.2164543.

[15] C. Schleich et al., "Single-Versus Multi-Step Trap Assisted Tunneling Currents-Part II: The Role of Polarons," *IEEE Transactions on Electron Devices*, vol. 69, no. 8, pp. 4486–4493, Aug. 2022, ISSN: 1557-9646. DOI: 10.1109/TED.2022.3185965.

[16] K. Meng et al., "Superionic fluoride gate dielectrics with low diffusion barrier for two-dimensional electronics," *Nature Nanotechnology*, vol. 19, no. 7, pp. 932–940, Jul. 2024, ISSN: 1748-3395. DOI: 10.1038/s41565-024-01675-5.

[17] E. Yon, W. Ko, and A. Kuper, "Sodium distribution in thermal oxide on silicon by radiochemical and MOS analysis," *IEEE Transactions on Electron Devices*, vol. ED-13, no. 2, pp. 276–280, Feb. 1966, ISSN: 1557-9646. DOI: 10.1109/T-ED.1966.15680.

[18] M. Lee, Y. Youn, K. Yim, and S. Han, "High-throughput ab initio calculations on dielectric constant and band gap of non-oxide dielectrics," *Scientific Reports*, vol. 8, no. 1, p. 14 794, Oct. 4, 2018, ISSN: 2045-2322. DOI: 10.1038/s41598-018-33095-6.

[19] Y. Y. Illarionov et al., "Ultrathin calcium fluoride insulators for two-dimensional field-effect transistors," *Nature Electronics*, vol. 2, no. 6, pp. 230–235, Jun. 2019, ISSN: 2520-1131. DOI: 10.1038/s41928-019-0256-8.

[20] S. E. Tyaginov et al., "Modeling of deep-submicron silicon-based MISFETs with calcium fluoride dielectric," *Journal of Computational Electronics*, vol. 13, no. 3, pp. 733–738, Sep. 2014, ISSN: 1569-8025, 1572-8137. DOI: 10.1007/s10825-014-0593-9.

[21] L. Huang, H. Liu, and W. Cui, "High-k monolayer CaF_2 as the Gate Dielectric for Two-Dimensional SiC-Based Field-Effect Transistors," *ACS Applied Electronic Materials*, vol. 5, no. 9, pp. 5082–5092, Sep. 26, 2023. DOI: 10.1021/acsaelm.3c00829.

[22] H. Umezawa et al., "Cu/CaF_2 Diamond Metal-Insulator-Semiconductor Field-Effect Transistor Utilizing Self-Aligned Gate Fabrication Process," *Japanese Journal of Applied Physics*, vol. 39, p. L908, 9A Sep. 1, 2000, ISSN: 1347-4065. DOI: 10.1143/JJAP.39.L908.

[23] L. J. Schowalter et al., "Epitaxial growth and characterization of CaF_2 on Si," *Journal of Applied Physics*, vol. 58, no. 1, pp. 302–308, Jul. 1, 1985, ISSN: 0021-8979. DOI: 10.1063/1.335676.

[24] S. Hashimoto, J.-L. Peng, W. M. Gibson, L. J. Schowalter, and R. W. Fathauer, "Strain measurement of epitaxial CaF_2 on Si (111) by MeV ion channeling," *Applied Physics Letters*, vol. 47, no. 10, pp. 1071–1073, Nov. 15, 1985, ISSN: 0003-6951. DOI: 10.1063/1.96383.

[25] D. Rieger, F. J. Himpsel, U. O. Karlsson, F. R. McFeely, J. F. Morar, and J. A. Yarmoff, "Electronic structure of the CaF_2/Si(111) interface," *Physical Review B*, vol. 34, no. 10, pp. 7295–7306, Nov. 15, 1986. DOI: 10.1103/PhysRevB.34.7295.

[26] O. R. N. Laboratory. "Frontier," Accessed: Jan. 24, 2025. [Online]. Available: https://www.olcf.ornl.gov/frontier/.

[27] R. M. Martin, *Electronic Structure: Basic Theory and Practical Methods*, 2nd ed. Cambridge University Press, Aug. 27, 2020, ISBN: 978-1-108-55558-6 978-1-108-42990-0. DOI: 10.1017/9781108555586.

[28] M. Born and R. Oppenheimer, "Zur Quantentheorie der Molekeln," *Annalen der Physik*, vol. 389, no. 20, pp. 457–484, 1927, ISSN: 1521-3889. DOI: 10.1002/andp.19273892002.

[29] D. J. Griffiths and D. F. Schroeter, *Introduction to Quantum Mechanics*, Third Edition. Upper Saddle River, NJ: Cambridge University Press, 2018, ISBN: 978-1-107-18963-8.

[30] F. Bloch, "Über die Quantenmechanik der Elektronen in Kristallgittern," *Zeitschrift für Physik*, vol. 52, no. 7, pp. 555–600, Jul. 1, 1929, ISSN: 0044-3328. DOI: 10.1007/BF01339455.

[31] D. R. Hartree, "The Wave Mechanics of an Atom with a Non-Coulomb Central Field. Part II. Some Results and Discussion," *Mathematical Proceedings of the Cambridge Philosophical Society*, vol. 24, no. 1, pp. 111–132, Jan. 1928, ISSN: 1469-8064, 0305-0041. DOI: 10.1017/S0305004100011920.

[32] J. C. Slater, "The Self Consistent Field and the Structure of Atoms," *Physical Review*, vol. 32, no. 3, pp. 339–348, Sep. 1, 1928. DOI: 10.1103/PhysRev.32.339.

[33] J. C. Slater, "Note on Hartree's Method," *Physical Review*, vol. 35, no. 2, pp. 210–211, Jan. 15, 1930. DOI: 10.1103/PhysRev.35.210.2.

[34] V. Fock, "Näherungsmethode zur Lösung des quantenmechanischen Mehrkörperproblems," *Zeitschrift für Physik*, vol. 61, no. 1, pp. 126–148, Jan. 1, 1930, ISSN: 0044-3328. DOI: 10.1007/BF01340294.

[35] D. R. Hartree and W. Hartree, "Self-consistent field, with exchange, for beryllium," *Proceedings of the Royal Society of London. Series A-Mathematical and Physical Sciences*, vol. 150, no. 869, pp. 9–33, 1935. DOI: 10.1098/rspa.1935.0085.

[36] P. Hohenberg and W. Kohn, "Inhomogeneous Electron Gas," *Physical Review*, vol. 136, B864–B871, 3B Nov. 9, 1964. DOI: 10.1103/PhysRev.136.B864.

[37] J. VandeVondele and J. Hutter, "An efficient orbital transformation method for electronic structure calculations," *The Journal of Chemical Physics*, vol. 118, no. 10, pp. 4365–4369, Mar. 8, 2003, ISSN: 0021-9606. DOI: 10.1063/1.1543154.

[38] V. Weber, J. VandeVondele, J. Hutter, and A. M. N. Niklasson, "Direct energy functional minimization under orthogonality constraints," *The Journal of Chemical Physics*, vol. 128, no. 8, p. 084 113, Feb. 29, 2008, ISSN: 0021-9606. DOI: 10.1063/1.2841077.

[39] W. Kohn and L. J. Sham, "Self-Consistent Equations Including Exchange and Correlation Effects," *Physical Review*, vol. 140, A1133–A1138, 4A Nov. 15, 1965. DOI: 10.1103/PhysRev.140.A1133.

[40] P. a. M. Dirac, "Note on Exchange Phenomena in the Thomas Atom," *Mathematical Proceedings of the Cambridge Philosophical Society*, vol. 26, no. 3, pp. 376–385, Jul. 1930, ISSN: 1469-8064, 0305-0041. DOI: 10.1017/S0305004100016108.

[41] D. M. Ceperley and B. J. Alder, "Ground State of the Electron Gas by a Stochastic Method," *Physical Review Letters*, vol. 45, no. 7, pp. 566–569, Aug. 18, 1980. DOI: 10.1103/PhysRevLett.45.566.

[42] J. P. Perdew, K. Burke, and M. Ernzerhof, "Generalized Gradient Approximation Made Simple," *Physical Review Letters*, vol. 77, no. 18, pp. 3865–3868, Oct. 28, 1996. DOI: 10.1103/PhysRevLett.77.3865.

[43] D. Rappoport, N. R. M. Crawford, F. Furche, and K. Burke, "Approximate Density Functionals: Which Should I Choose?" In *Encyclopedia of Inorganic Chemistry*, John Wiley & Sons, Ltd, 2009, ISBN: 978-0-470-86210-0. DOI: 10.1002/0470862106.ia615.

[44] Y. Wang and J. P. Perdew, "Correlation hole of the spin-polarized electron gas, with exact small-wave-vector and high-density scaling," *Physical Review B*, vol. 44, no. 24, pp. 13 298–13 307, Dec. 15, 1991. DOI: 10.1103/PhysRevB.44.13298.

[45] J. P. Perdew et al., "Restoring the density-gradient expansion for exchange in solids and surfaces," *Physical Review Letters*, vol. 100, no. 13, p. 136 406, Apr. 4, 2008, ISSN: 0031-9007, 1079-7114. DOI: 10.1103/PhysRevLett.100.136406. arXiv: 0711.0156 [cond-mat].

[46] J. P. Perdew and M. Levy, "Physical Content of the Exact Kohn-Sham Orbital Energies: Band Gaps and Derivative Discontinuities," *Physical Review Letters*, vol. 51, no. 20, pp. 1884–1887, Nov. 14, 1983. DOI: 10.1103/PhysRevLett.51.1884.

[47] A. D. Becke, "A new mixing of Hartree–Fock and local density-functional theories," *The Journal of Chemical Physics*, vol. 98, no. 2, pp. 1372–1377, Jan. 15, 1993, ISSN: 0021-9606. DOI: 10.1063/1.464304.

[48] C. Adamo and V. Barone, "Toward reliable density functional methods without adjustable parameters: The PBE0 model," *The Journal of Chemical Physics*, vol. 110, no. 13, pp. 6158–6170, Apr. 1, 1999, ISSN: 0021-9606. DOI: 10.1063/1.478522.

[49] M. Guidon, J. Hutter, and J. VandeVondele, "Robust Periodic Hartree-Fock Exchange for Large-Scale Simulations Using Gaussian Basis Sets," *Journal of Chemical Theory and Computation*, vol. 5, no. 11, pp. 3010–3021, Nov. 10, 2009, ISSN: 1549-9618. DOI: 10.1021/ct900494g.

[50] J. Heyd, G. E. Scuseria, and M. Ernzerhof, "Hybrid functionals based on a screened Coulomb potential," *The Journal of Chemical Physics*, vol. 118, no. 18, pp. 8207–8215, May 8, 2003, ISSN: 0021-9606. DOI: 10.1063/1.1564060.

[51] A. V. Krukau, O. A. Vydrov, A. F. Izmaylov, and G. E. Scuseria, "Influence of the exchange screening parameter on the performance of screened hybrid functionals," *The Journal of Chemical Physics*, vol. 125, no. 22, p. 224 106, Dec. 13, 2006, ISSN: 0021-9606. DOI: 10.1063/1.2404663.

[52] A. J. Garza and G. E. Scuseria, "Predicting Band Gaps with Hybrid Density Functionals," *The Journal of Physical Chemistry Letters*, vol. 7, no. 20, pp. 4165–4170, Oct. 20, 2016. DOI: 10.1021/acs.jpclett.6b01807.

[53] G. Strang, *Introduction to Linear Algebra, Sixth Edition*. Wellesley-Cambridge Press, Jan. 2022, 440 pp., ISBN: 978-1-7331466-7-8. DOI: 10.1137/1.9781733146678.

[54] J. C. Slater, "Atomic Shielding Constants," *Physical Review*, vol. 36, no. 1, pp. 57–64, Jul. 1, 1930. DOI: 10.1103/PhysRev.36.57.

[55] I. Shavitt and M. Karplus, "Multicenter Integrals in Molecular Quantum Mechanics," *The Journal of Chemical Physics*, vol. 36, no. 2, pp. 550–551, Jan. 15, 1962, ISSN: 0021-9606. DOI: 10.1063/1.1732550.

[56] H. Taketa, S. Huzinaga, and K. O-ohata, "Gaussian-Expansion Methods for Molecular Integrals," *Journal of the Physical Society of Japan*, vol. 21, no. 11, pp. 2313–2324, Nov. 15, 1966, ISSN: 0031-9015. DOI: 10.1143/JPSJ.21.2313.

[57] B. P. Pritchard, D. Altarawy, B. Didier, T. D. Gibson, and T. L. Windus, "New Basis Set Exchange: An Open, Up-to-Date Resource for the Molecular Sciences Community," *Journal of Chemical Information and Modeling*, vol. 59, no. 11, pp. 4814–4820, Nov. 25, 2019, ISSN: 1549-9596. DOI: 10.1021/acs.jcim.9b00725.

[58] G. Lippert, J. Hutter, and M. Parrinello, "A hybrid Gaussian and plane wave density functional scheme," *Molecular Physics*, vol. 92, no. 3, pp. 477–488, Oct. 1, 1997, ISSN: 0026-8976. DOI: 10.1080/002689797170220.

[59] T. D. Kühne et al., "CP2K: An Electronic Structure and Molecular Dynamics Software Package–Quickstep: Efficient and Accurate Electronic Structure Calculations," *The Journal of Chemical Physics*, vol. 152, no. 19, p. 194103, May 21, 2020, ISSN: 0021-9606, 1089-7690. DOI: 10.1063/5.0007045. arXiv: 2003.03868 [physics].

[60] G. Lippert, J. Hutter, and M. Parrinello, "The Gaussian and augmented-plane-wave density functional method for ab initio molecular dynamics simulations," *Theoretical Chemistry Accounts*, vol. 103, no. 2, pp. 124–140, Dec. 1, 1999, ISSN: 1432-2234. DOI: 10.1007/s002140050523.

[61] M. Krack and M. Parrinello, "All-electron ab-initio molecular dynamics," *Physical Chemistry Chemical Physics*, vol. 2, no. 10, pp. 2105–2112, Jan. 1, 2000, ISSN: 1463-9084. DOI: 10.1039/B001167N.

[62] B. Nagy and F. Jensen, "Basis Sets in Quantum Chemistry," in *Reviews in Computational Chemistry*, John Wiley & Sons, Ltd, 2017, pp. 93–149, ISBN: 978-1-119-35605-9. DOI: 10.1002/9781119356059.ch3.

[63] K. Laasonen, R. Car, C. Lee, and D. Vanderbilt, "Implementation of ultrasoft pseudopotentials in ab initio molecular dynamics," *Physical Review B*, vol. 43, no. 8, pp. 6796–6799, Mar. 15, 1991. DOI: 10.1103/PhysRevB.43.6796.

[64] P. E. Blöchl, "Projector augmented-wave method," *Physical Review B*, vol. 50, no. 24, pp. 17 953–17 979, Dec. 15, 1994. DOI: 10.1103/PhysRevB.50.17953.

[65] D. R. Hamann, M. Schlüter, and C. Chiang, "Norm-Conserving Pseudopotentials," *Physical Review Letters*, vol. 43, no. 20, pp. 1494–1497, Nov. 12, 1979. DOI: 10.1103/PhysRevLett.43.1494.

[66] S. Goedecker, M. Teter, and J. Hutter, "Separable dual-space Gaussian pseudopotentials," *Physical Review B*, vol. 54, no. 3, pp. 1703–1710, Jul. 15, 1996. DOI: 10.1103/PhysRevB.54.1703.

[67] M. Krack, "Pseudopotentials for H to Kr optimized for gradient-corrected exchange-correlation functionals," *Theoretical Chemistry Accounts*, vol. 114, no. 1, pp. 145–152, Sep. 1, 2005, ISSN: 1432-2234. DOI: 10.1007/s00214-005-0655-y.

[68] M. Guidon, J. Hutter, and J. VandeVondele, "Auxiliary Density Matrix Methods for hartree-fock exchange calculations," *Journal of Chemical Theory and Computation*, vol. 6, no. 8, pp. 2348–2364, Aug. 10, 2010, ISSN: 1549-9618. DOI: 10.1021/ct1002225.

[69] A. Togo, "First-principles Phonon Calculations with Phonopy and Phono3py," *Journal of the Physical Society of Japan*, vol. 92, no. 1, p. 012 001, Jan. 15, 2023, ISSN: 0031-9015, 1347-4073. DOI: 10.7566/JPSJ.92.012001.

[70] J. F. Nye and J. F. Nye, *Physical Properties of Crystals: Their Representation by Tensors and Matrices*. Oxford, New York: Oxford University Press, May 16, 1985, 352 pp., ISBN: 978-0-19-851165-6.

[71] J. J. Burckhardt, "Kristallsysteme und Kristallklassen - Weiß, Frankenheim, Hessel," in *Die Symmetrie der Kristalle: Von René-Just Haüy zur kristallographischen Schule in Zürich*, J. J. Burckhardt, Ed., Basel: Birkhäuser, 1988, pp. 31–47, ISBN: 978-3-0348-6027-7. DOI: 10.1007/978-3-0348-6027-7_4.

[72] J. J. Burckhardt, "Gitter und Netze. Frankenheim und Bravais," in *Die Symmetrie der Kristalle: Von René-Just Haüy zur kristallographischen Schule in Zürich*, J. J. Burckhardt, Ed., Basel: Birkhäuser, 1988, pp. 48–55, ISBN: 978-3-0348-6027-7. DOI: 10.1007/978-3-0348-6027-7_5.

[73] J. J. Burckhardt, "Fedorovs Entdeckung der 230 kristallographischen Raumsymmetriesysteme (von Erhard Scholz)," in *Die Symmetrie der Kristalle: Von René-Just Haüy zur kristallographischen Schule in Zürich*, J. J. Burckhardt, Ed., Basel: Birkhäuser, 1988, pp. 73–80, ISBN: 978-3-0348-6027-7. DOI: 10.1007/978-3-0348-6027-7_9.

[74] E. F. Bertaut, "Symbols for plane groups (two-dimensional space groups)," in *International Tables for Crystallography Volume A: Space-group Symmetry*, Th. Hahn, Ed., Dordrecht: Springer Netherlands, 2002, pp. 61–61, ISBN: 978-1-4020-5406-8. DOI: 10.1107/97809553602060000508.

[75] E. F. Bertaut, "Symbols for space groups," in *International Tables for Crystallography Volume A: Space-group Symmetry*, Th. Hahn, Ed., Dordrecht: Springer Netherlands, 2002, pp. 62–76, ISBN: 978-1-4020-5406-8. DOI: 10.1107/97809553602060000509.

[76] R. W. G. Wyckoff, *The Analytical Expression of the Results of the Theory of Space-Groups*. Washington: Carnegie Institution of Washington, 1922, vii, 180.

[77] M. I. Aroyo, Ed., *International Tables for Crystallography: Space-group Symmetry*, 2nd ed. Chester, England: International Union of Crystallography, Dec. 31, 2016, vol. A, ISBN: 978-0-470-97423-0. DOI: 10.1107/97809553602060000114.

[78] L. J. Sham and M. Schlüter, "Density-Functional Theory of the Energy Gap," *Physical Review Letters*, vol. 51, no. 20, pp. 1888–1891, Nov. 14, 1983. DOI: 10.1103/PhysRevLett.51.1888.

[79] A. Savin, C. J. Umrigar, and X. Gonze, "Relationship of Kohn–Sham eigenvalues to excitation energies," *Chemical Physics Letters*, vol. 288, no. 2, pp. 391–395, May 22, 1998, ISSN: 0009-2614. DOI: 10.1016/S0009-2614(98)00316-9.

[80] J. P. Perdew et al., "Understanding band gaps of solids in generalized Kohn–Sham theory," *Proceedings of the National Academy of Sciences*, vol. 114, no. 11, pp. 2801–2806, Mar. 14, 2017. DOI: 10.1073/pnas.1621352114.

[81] G. Eckold, "Phonons," in *International Tables for Crystallography Volume D: Physical Properties of Crystals*, A. Authier, Ed., Dordrecht: Springer Netherlands, 2003, pp. 266–293, ISBN: 978-1-4020-5409-9. DOI: 10.1107/97809553602060000638.

[82] H. Hellmann, *Einführung in die Quantenchemie*. Ann Arbor, Mich: J.W. Edwards, 1944, 350 pp.

[83] R. P. Feynman, "Forces in Molecules," *Physical Review*, vol. 56, no. 4, pp. 340–343, Aug. 15, 1939. DOI: 10.1103/PhysRev.56.340.

[84] I. Pallikara, P. Kayastha, J. M. Skelton, and L. D. Whalley, "The physical significance of imaginary phonon modes in crystals," *Electronic Structure*, vol. 4, no. 3, p. 033 002, Jul. 2022, ISSN: 2516-1075. DOI: 10.1088/2516-1075/ac78b3.

[85] A. Togo, K. Shinohara, and I. Tanaka, "Spglib: A software library for crystal symmetry search," *Science and Technology of Advanced Materials: Methods*, vol. 4, no. 1, p. 2 384 822, Dec. 31, 2024, ISSN: null. DOI: 10.1080/27660400.2024.2384822.

[86] X. Gonze and C. Lee, "Dynamical Matrices, Born Effective Charges, Dielectric Permittivity Tensors, and Interatomic Force Constants from Density-Functional Perturbation Theory," *Physical Review B*, vol. 55, no. 16, pp. 10 355–10 368, Apr. 15, 1997. DOI: 10.1103/PhysRevB.55.10355.

[87] N. A. Spaldin, "A Beginner's Guide to the Modern Theory of Polarization," *Journal of Solid State Chemistry*, Polar Inorganic Materials: Design Strategies and Functional Properties, vol. 195, pp. 2–10, Nov. 1, 2012, ISSN: 0022-4596. DOI: 10.1016/j.jssc.2012.05.010.

[88] H. Mehrer, *Diffusion in Solids* (Springer Series in Solid-State Sciences), M. Cardona, P. Fulde, K. Von Klitzing, H.-J. Queisser, R. Merlin, and H. Störmer, red. Berlin, Heidelberg: Springer, 2007, vol. 155, ISBN: 978-3-540-71486-6 978-3-540-71488-0. DOI: 10.1007/978-3-540-71488-0.

[89] B. Prince, "Embedded non-volatile memories," in *Proceedings of the 20th Annual Conference on Integrated Circuits and Systems Design*, ser. SBCCI '07, New York, NY, USA: Association for Computing Machinery, Sep. 3, 2007, p. 9, ISBN: 978-1-59593-816-9. DOI: 10.1145/1284480.1284490.

[90] C. Wilhelmer, D. Waldhoer, L. Cvitkovich, D. Milardovich, M. Waltl, and T. Grasser, "Over-and Undercoordinated Atoms as a Source of Electron and Hole Traps in Amorphous Silicon Nitride (a-Si3N4)," *Nanomaterials*, vol. 13, no. 16, p. 2286, 16 Jan. 2023, ISSN: 2079-4991. DOI: 10.3390/nano13162286.

[91] S. B. Zhang and J. E. Northrup, "Chemical potential dependence of defect formation energies in GaAs: Application to Ga self-diffusion," *Physical Review Letters*, vol. 67, no. 17, pp. 2339–2342, Oct. 21, 1991. DOI: 10.1103/PhysRevLett.67.2339.

[92] C. Freysoldt, J. Neugebauer, and C. G. Van de Walle, "Fully Ab Initio Finite-Size Corrections for Charged-Defect Supercell Calculations," *Physical Review Letters*, vol. 102, no. 1, p. 016 402, Jan. 5, 2009. DOI: 10.1103/PhysRevLett.102.016402.

[93] A. Alkauskas, Q. Yan, and C. G. Van de Walle, "First-principles theory of nonradiative carrier capture via multiphonon emission," *Physical Review B*, vol. 90, no. 7, p. 075 202, Aug. 18, 2014. DOI: 10.1103/PhysRevB.90.075202.

[94] M. H. Naik and M. Jain, "CoFFEE: Corrections For Formation Energy and Eigenvalues for charged defect simulations," *Computer Physics Communications*, vol. 226, pp. 114–126, May 1, 2018, ISSN: 0010-4655. DOI: 10.1016/j.cpc.2018.01.011.

[95] H. Eyring, "The Activated Complex in Chemical Reactions," *The Journal of Chemical Physics*, vol. 3, no. 2, pp. 107–115, Feb. 1, 1935, ISSN: 0021-9606. DOI: 10.1063/1.1749604.

[96] M. G. Evans and M. Polanyi, "Some applications of the transition state method to the calculation of reaction velocities, especially in solution," *Transactions of the Faraday Society*, vol. 31, no. 0, pp. 875–894, Jan. 1, 1935, ISSN: 0014-7672. DOI: 10.1039/TF9353100875.

[97] A. Cahlík et al., "Significance Of Nuclear Quantum Effects In Hydrogen Bonded Molecular Chains," *ACS Nano*, vol. 15, no. 6, pp. 10 357–10 365, Jun. 22, 2021, ISSN: 1936-0851. DOI: 10.1021/acsnano.1c02572.

[98] A. Nitzan, *Chemical Reactions In Condensed Phases: Relaxation, Transfer and Reactions in Condensed Molecular Systems*, A. Nitzan, Ed. Oxford University Press, Apr. 6, 2006, ISBN: 978-0-19-852979-8. DOI: 10.1093/oso/9780198529798.003.0021.

[99] K.-N. Tu and A. M. Gusak, "Linear and Nonlinear Diffusion," in *Kinetics in Nanoscale Materials*, John Wiley & Sons, Ltd, 2014, pp. 37–66, ISBN: 978-1-118-74314-0. DOI: 10.1002/9781118743140.ch2.

[100] E. P. Gusev and Electrochemical Society, Eds., *Advanced Gate Stack, Source/Drain, and Channel Engineering for Si-Based CMOS 2: New Materials, Processes and Equipment.* (ECS Transactions Dielectric and Semiconductor Materials, Devices, and Processing). Pennington, Pa: Electrochemical Soc, 2006.

[101] H. Jónsson, G. Mills, and K. W. Jacobsen, "Nudged elastic band method for finding minimum energy paths of transitions," in *Classical and Quantum Dynamics in Condensed Phase Simulations*, World Scientific, Jun. 1998, pp. 385–404, ISBN: 978-981-02-3498-0. DOI: 10.1142/9789812839664_0016.

[102] G. Henkelman, B. P. Uberuaga, and H. Jónsson, "A climbing image nudged elastic band method for finding saddle points and minimum energy paths," *The Journal of Chemical Physics*, vol. 113, no. 22, pp. 9901–9904, Dec. 8, 2000, ISSN: 0021-9606. DOI: 10.1063/1.1329672.

[103] G. Henkelman and H. Jónsson, "A dimer method for finding saddle points on high dimensional potential surfaces using only first derivatives," *The Journal of Chemical Physics*, vol. 111, no. 15, pp. 7010–7022, Oct. 15, 1999, ISSN: 0021-9606. DOI: 10.1063/1.480097.

[104] R. Elber and M. Karplus, "A method for determining reaction paths in large molecules: Application to myoglobin," *Chemical Physics Letters*, vol. 139, no. 5, pp. 375–380, Jan. 1, 1987, ISSN: 0009-2614. DOI: 10.1016/0009-2614(87)80576-6.

[105] X. Zhu, K. C. Thompson, and T. J. Martínez, "Geodesic interpolation for reaction pathways," *The Journal of Chemical Physics*, vol. 150, no. 16, p. 164 103, Apr. 22, 2019, ISSN: 0021-9606. DOI: 10.1063/1.5090303.

[106] P. Xiao, Q. Wu, and G. Henkelman, "Basin constrained k-dimer method for saddle point finding," *The Journal of Chemical Physics*, vol. 141, no. 16, p. 164 111, Oct. 27, 2014, ISSN: 0021-9606. DOI: 10.1063/1.4898664.

[107] J. Heyd and G. E. Scuseria, "Assessment and validation of a screened Coulomb hybrid density functional," *The Journal of Chemical Physics*, vol. 120, no. 16, pp. 7274–7280, Apr. 22, 2004, ISSN: 0021-9606. DOI: 10.1063/1.1668634.

[108] H. J. Monkhorst and J. D. Pack, "Special points for Brillouin-zone integrations," *Physical Review B*, vol. 13, no. 12, pp. 5188–5192, Jun. 15, 1976. DOI: 10.1103/PhysRevB.13.5188.

[109] A. Bussy and J. Hutter, "Efficient periodic resolution-of-the-identity Hartree–Fock exchange method with k-point sampling and Gaussian basis sets," *The Journal of Chemical Physics*, vol. 160, no. 6, p. 064 116, Feb. 14, 2024, ISSN: 0021-9606. DOI: 10.1063/5.0189659.

[110] M. Guidon, F. Schiffmann, J. Hutter, and J. VandeVondele, "Ab initio molecular dynamics using hybrid density functionals," *The Journal of Chemical Physics*, vol. 128, no. 21, p. 214 104, Jun. 4, 2008, ISSN: 0021-9606. DOI: 10.1063/1.2931945.

[111] A. Jain et al., "Commentary: The Materials Project: A materials genome approach to accelerating materials innovation," *APL Materials*, vol. 1, no. 1, p. 011 002, Jul. 18, 2013, ISSN: 2166-532X. DOI: 10.1063/1.4812323.

[112] I. Petousis et al., "High-throughput screening of inorganic compounds for the discovery of novel dielectric and optical materials," *Scientific Data*, vol. 4, no. 1, p. 160 134, Jan. 31, 2017, ISSN: 2052-4463. DOI: 10.1038/sdata.2016.134.

[113] D. C. Liu and J. Nocedal, "On the limited memory BFGS method for large scale optimization," *Mathematical Programming*, vol. 45, no. 1, pp. 503–528, Aug. 1, 1989, ISSN: 1436-4646. DOI: 10.1007/BF01589116.

[114] R. Fletcher, *Practical Methods of Optimization*. John Wiley & Sons, Ltd, 2000, ISBN: 9781118723203. DOI: 10.1002/9781118723203.fmatter.

[115] Z. Hashin and S. Shtrikman, "Conductivity of Polycrystals," *Physical Review*, vol. 130, no. 1, pp. 129–133, Apr. 1, 1963. DOI: 10.1103/PhysRev.130.129.

[116] G. W. Rubloff, "Far-Ultraviolet Reflectance Spectra and the Electronic Structure of Ionic Crystals," *Physical Review B*, vol. 5, no. 2, pp. 662–684, Jan. 15, 1972, ISSN: 0556-2805. DOI: 10.1103/PhysRevB.5.662.

[117] K. Suzuki, M. Cadatal-Raduban, M. Kase, and S. Ono, "Band gap engineering of $Ca_xSr_{1-x}F_2$ and its application as filterless vacuum ultraviolet photodetectors with controllable spectral responses," *Optical Materials*, vol. 88, pp. 576–579, Feb. 1, 2019, ISSN: 0925-3467. DOI: 10.1016/j.optmat.2018.12.023.

[118] R. P. Lowndes, "Dielectric Response of the Alkaline Earth Fluorides," *Journal of Physics C: Solid State Physics*, vol. 2, no. 9, p. 1595, Sep. 1969, ISSN: 0022-3719. DOI: 10.1088/0022-3719/2/9/309.

[119] J. G. Hartnett, A. C. Fowler, M. E. Tobar, and J. Krupka, "The microwave characterization of single crystal lithium and calcium fluoride at cryogenic temperatures," *IEEE transactions on ultrasonics, ferroelectrics, and frequency control*, vol. 51, no. 4, pp. 380–386, Apr. 2004, ISSN: 0885-3010. DOI: 10.1109/tuffc.2004.1295423. PMID: 15139539.

[120] R. Geyer, J. Baker-Jarvis, and J. Krupka, "Dielectric characterization of single-crystal lif, CaF_2, MgF_2, BaF_2, and SrF_2 at microwave frequencies," in *The 17th Annual Meeting of the IEEE Lasers and Electro-Optics Society, 2004. LEOS 2004.*, Oct. 2004, pp. 493–497. DOI: 10.1109/CEIDP.2004.1364295.

[121] M. Wintersgill, J. Fontanella, C. Andeen, and D. Schuele, "The temperature variation of the dielectric constant of "pure" CaF_2, SrF_2, BaF_2, and MgO," *Journal of Applied Physics*, vol. 50, no. 12, pp. 8259–8261, Dec. 1, 1979, ISSN: 0021-8979. DOI: 10.1063/1.325932.

[122] C. Feng et al., "A newly discovered BiF_3 photocatalyst with a high positive valence band," *Journal of Molecular Catalysis A: Chemical*, vol. 401, pp. 35–40, May 15, 2015, ISSN: 1381-1169. DOI: 10.1016/j.molcata.2015.02.022.

[123] T. J. Moravec, R. A. Skogman, and E. B. G, "Optical properties of bismuth trifluoride thin films," *Applied Optics*, vol. 18, no. 1, pp. 105–110, Jan. 1, 1979, ISSN: 2155-3165. DOI: 10.1364/AO.18.000105.

[124] S. K. Ghosh, V. K. Perla, and K. Mallick, "Enhancement of dielectric and electric-field-induced polarization of bismuth fluoride nanoparticles within the layered structure of carbon nitride," *Scientific Reports*, vol. 10, no. 1, p. 14 835, Sep. 9, 2020, ISSN: 2045-2322. DOI: 10.1038/s41598-020-71953-4.

[125] M. Cadatal-Raduban et al., "Investigation of cross luminescence in lanthanum fluoride as a potential fast-response scintillator," *Japanese Journal of Applied Physics*, vol. 59, no. 5, p. 052 005, May 2020, ISSN: 1347-4065. DOI: 10.35848/1347-4065/ab887b.

[126] H.-D. Wiemhöfer, S. Harke, and U. Vohrer, "Electronic properties and gas interaction of LaF_3 and ZrO_2," *Solid State Ionics*, vol. 40–41, pp. 433–439, Aug. 1, 1990, ISSN: 0167-2738. DOI: 10.1016/0167-2738(90)90373-Y.

[127] J. C. Krupa and M. Queffelec, "UV and VUV optical excitations in wide band gap materials doped with rare earth ions: 4f–5d transitions," *Journal of Alloys and Compounds*, vol. 250, no. 1, pp. 287–292, Mar. 20, 1997, ISSN: 0925-8388. DOI: 10.1016/S0925-8388(96)02725-9.

[128] R. Solomon, A. Sher, and M. W. Muller, "Polarization in LaF_3," *Journal of Applied Physics*, vol. 37, no. 9, pp. 3427–3432, Aug. 1, 1966, ISSN: 0021-8979. DOI: 10.1063/1.1708875.

[129] T. Mahalingam, M. Radhakrishnan, and C. Balasubramanian, "Dielectric of properties of lanthanum fluoride thin films," *Thin Solid Films*, vol. 59, no. 2, pp. 221–229, May 1, 1979, ISSN: 0040-6090. DOI: 10.1016/0040-6090(79)90295-5.

[130] M. A. F. Destro and A. J. Damião, "Lead Fluoride (PbF2)," in *Handbook of Optical Constants of Solids*, E. D. Palik, Ed., Burlington: Academic Press, Jan. 1, 1997, pp. 761–776, ISBN: 978-0-12-544415-6. DOI: 10.1016/B978-012544415-6.50131-X.

[131] K. F. Young and H. P. R. Frederikse, "Compilation of the Static Dielectric Constant of Inorganic Solids," *Journal of Physical and Chemical Reference Data*, vol. 2, no. 2, pp. 313–410, Apr. 1, 1973, ISSN: 0047-2689. DOI: 10.1063/1.3253121.

[132] F. Marabelli, P. Wachter, and G. Kaindl, "Optical spectroscopy of the covalent insulator CeF_4," *Physical Review B*, vol. 46, no. 16, pp. 10 012–10 016, Oct. 15, 1992. DOI: 10.1103/PhysRevB.46.10012.

[133] E. Talik, P. Zajdel, A. Guzik, D. Skrzypek, L. Lipińska, and M. Michalska, "Electronic and crystal structure, EPR and magnetic investigations of YF_3:1%re (RE=Pr, Ho, Er and Tm) and LaF_3:1%Pr nanocrystals," *Journal of Alloys and Compounds*, vol. 616, pp. 556–568, Dec. 15, 2014, ISSN: 0925-8388. DOI: 10.1016/j.jallcom.2014.07.074.

[134] V. Trnovcova, P. Fedorov, B. Sobolev, K. Seiranyan, S. Oganesyan, and M. Val'kovskii, "Conductivity of orthorhombic beta-YF_3 single crystals," *Crystallography Reports*, vol. 41, no. 4, p. 694–699, Jul. 1996. DOI: 10.1134/1.170470.

[135] D. K. Schroder, "Negative bias temperature instability: What do we understand?" *Microelectronics Reliability*, Modelling the Negative Bias Temperature Instability, vol. 47, no. 6, pp. 841–852, Jun. 1, 2007, ISSN: 0026-2714. DOI: 10.1016/j.microrel.2006.10.006.

[136] K. S. Ralls et al., "Discrete Resistance Switching in Submicrometer Silicon Inversion Layers: Individual Interface Traps and Low-Frequency (1/f?) Noise," *Physical Review Letters*, vol. 52, no. 3, pp. 228–231, Jan. 16, 1984. DOI: 10.1103/PhysRevLett.52.228.

[137] R. Ghosh et al., "Theoretical insights into the impact of border and interface traps on hysteresis in monolayer MoS_2 fets," *Microelectronic Engineering*, vol. 299, p. 112 333, 2025. DOI: 10.1016/j.mee.2025.112333.

[138] F. Schanovsky, O. Baumgartner, V. Sverdlov, and T. Grasser, "A multi scale modeling approach to non-radiative multi phonon transitions at oxide defects in MOS structures," *Journal of Computational Electronics*, vol. 11, no. 3, pp. 218–224, Sep. 1, 2012, ISSN: 1572-8137. DOI: 10.1007/s10825-012-0403-1.

[139] A. I. Chou, K. Lai, K. Kumar, P. Chowdhury, and J. C. Lee, "Modeling of stress-induced leakage current in ultrathin oxides with the trap-assisted tunneling mechanism," *Applied Physics Letters*, vol. 70, no. 25, pp. 3407–3409, Jun. 23, 1997, ISSN: 0003-6951. DOI: 10.1063/1.119186.

[140] J. D. Sundberg, D. L. Druffel, L. M. McRae, M. G. Lanetti, J. T. Pawlik, and S. C. Warren, "High-throughput discovery of fluoride-ion conductors via a decoupled, dynamic, and iterative (DDI) framework," *npj Computational Materials*, vol. 8, no. 1, pp. 1–9, May 6, 2022, ISSN: 2057-3960. DOI: 10.1038/s41524-022-00786-8.

[141] D. Waldhoer et al., "Comphy v3.0-A compact-physics framework for modeling charge trapping related reliability phenomena in MOS devices," *Microelectronics Reliability*, vol. 146, pp. 1–15, Jul. 2023, ISSN: 0026-2714. DOI: 10.1016/j.microrel.2023.115004.

[142] R. W. Ure, "Ionic Conductivity of Calcium Fluoride Crystals," *The Journal of Chemical Physics*, vol. 26, no. 6, pp. 1363–1373, Jun. 1, 1957, ISSN: 0021-9606, 1089-7690. DOI: 10.1063/1.1743547.

[143] N. I. Sorokin and D. N. Karimov, "Ionic Conductivity and Thermal Stability of BiF_3 crystals," *Kristallografiâ*, vol. 68, no. 2, pp. 285–289, 2 Mar. 1, 2023, ISSN: 0023-4761. DOI: 10.31857/S0023476123020182.

[144] F. Fujara, D. Kruk, O. Lips, A. F. Privalov, V. Sinitsyn, and H. Stork, "Fluorine dynamics in LaF_3-type fast ionic conductors - Combined results of NMR and conductivity techniques," *Solid State Ionics*, vol. 179, no. 40, pp. 2350–2357, Dec. 31, 2008, ISSN: 0167-2738. DOI: 10.1016/j.ssi.2008.10.003.

[145] V. V. Sinitsyn, O. Lips, A. F. Privalov, F. Fujara, and I. V. Murin, "Transport properties of LaF_3 fast ionic conductor studied by field gradient NMR and impedance spectroscopy," *Journal of Physics and Chemistry of Solids*, vol. 64, no. 7, pp. 1201–1205, Jul. 1, 2003, ISSN: 0022-3697. DOI: 10.1016/S0022-3697(03)00050-7.

[146] A. Roos, F. C. M. van de Pol, R. Keim, and J. Schoonman, "Ionic conductivity in tysonite-type solid solutions $La_{1-x}Ba_xF_{3-x}$," *Solid State Ionics*, vol. 13, no. 3, pp. 191–203, Jun. 1, 1984, ISSN: 0167-2738. DOI: 10.1016/0167-2738(84)90030-4.

[147] ECHA. “C&L Inventory BiF_3,” Accessed: Mar. 19, 2025. [Online]. Available: https://echa.europa.eu/information-on-chemicals/cl-inventory-database/-/discli/details/49409.